

MULTICHANNEL SENSE AND AVOID RADAR FOR SMALL UAVS

By

Lei Shi

Copyright 2016

Submitted to the graduate degree program in Electrical Engineering and Computer Science and the Graduate Faculty of the University of Kansas in partial fulfillment of the requirements for the degree of Doctor of Philosophy.

Chairperson: Christopher Allen

Glenn Prescott

James Stiles

Heechul Yun

Lisa Friis

Date Defended: May 24, 2016

The Dissertation Committee for Lei Shi
certifies that this is the approved version of the following dissertation:

MULTICHANNEL SENSE AND AVOID RADAR FOR SMALL UAVS

Chairperson: Christopher Allen

Date approved: May 24, 2016

Abstract

This dissertation investigates the feasibility of creating a multichannel sense and avoid radar system for small fixed-wing UAVs (also known as sUAS or drones). The target sUAS is a 40% Yak-54 remote controlled aircraft with a typical payload of 10 lbs. Small UAS's such as these are increasing in popularity for both personal, commercial, and government use including precision agriculture, infrastructure monitoring, and assisting first response. However, due to their lack of situation awareness, the FAA has placed strict regulations on their operation limiting their use on both the civil and government sides across the U.S. This miniature radar system is intended to provide these sUAS with target detection, tracking, and 3-D location and velocity information on potential non-cooperative hazards, primarily focusing on general aviation (GA) aircraft. The resulting FMCW miniature radar system has a size weight and power (SWaP) that is suitable for installing onboard the 40% Yak-54 UAS with the exception of replacing a TX power amplifier and has demonstrated, through measuring moving cars, that it is capable of target detection using a 2-D FFT processing algorithm and a constant false alarm rate (CFAR) detector. Tracking of the target was performed using the range-Doppler relationship of targets in the resulting radar image. The target's angular information in the form of target echo angle of arrival (AoA, needed for location estimation) was estimated using interferometry. While the angular estimations were in the right direction, their uncertainties resulting in significant fluctuations in estimated target XYZ position and XYZ velocities. It was observed that in the near term, averaging the AoA (which changes relatively slowly for steady flight) is a way to reduce this uncertainty. In the future, the radar system needs to be upgraded so that it can provide the ideal 10-Hz update rate which will also provide sufficient data for more complex target AoA detection algorithms.

Acknowledgments

I want to thank my parents who are first generation immigrants to the United States for showing me how to make courageous decisions in life. I want to thank my brother for being my brother; a statement that makes me more proud than anything I've accomplished. I want to thank my adviser Dr. Christopher Allen whose outstanding character is truly the foundation of this dissertation. The work presented here could not have been accomplished without a team of supporting individuals and not only am I grateful for all of their help but I feel that I have become a better person through working with them. Thank you to everyone that made this dissertation possible.

Table of Contents

Chapter 1: Introduction	1
1.1 Background – Small Unmanned Aircraft Systems (sUAS)	1
1.2 Radar systems.....	3
1.3 Collision avoidance technologies.....	5
1.4 Target platform and specifications	8
Chapter 2: Radar theory and simulations.....	10
2.1 Receiver power	10
2.2 Radar range and Doppler processing	11
2.3 Angle of arrival processing.....	15
2.4 Simulations	16
Chapter 3: Brassboard proof-of-concept radar	22
3.1 Brassboard radar hardware	22
3.1.1 Analog-to-digital converter.....	23
3.1.2 Waveform generator	24
3.1.3 FPGA	28
3.1.4 RF assembly.....	29
3.1.5 Antennas	32
3.2 Radar processing in hardware.....	34
3.3 Loopback testing.....	37
3.3.1 Data Interpretation	39
3.3.3 Anomalies and saturation.....	41
3.4 Flight testing	44

Chapter 4: Miniature radar	52
4.1 Miniature radar hardware.....	53
4.1.1 Miniature RF board.....	54
4.1.2 Miniature digital board	60
4.1.3 Antennas	64
4.2 Laboratory testing.....	65
4.2.1 Rev1 miniature radar system.....	65
4.2.2 Diagnostics procedure.....	69
4.2.3 Rev2 miniature radar system.....	75
4.2.4 Comparison to simulation	78
4.3 Roof top testing.....	79
4.3.1 Calibration target	79
4.3.2 Moving car measurements	85
Chapter 5: Performance analysis	88
5.1 Radar size, weight, and power	88
5.2 Target detection in range and Doppler	91
5.3 Angle of arrival estimation	94
5.3.1 Calibration beacon measurements	95
5.3.2 AoA simulations for miniature radar system.....	99
5.3.3 Phase difference to AoA conversion and fitting	102
5.3.4 Car measurement AoA.....	108
5.4 Target tracking and 6-DOF estimation	109
5.4.1 Target tracking.....	110

5.4.2 Six degrees of freedom (6-DOF) estimation.....	112
Chapter 6: Conclusion and continuing work	120
6.1 Conclusion	120
6.2 Continuing work	121
References	124
Appendix.....	127
A.1 Rev2 Miniature Radar RF Chain.....	127
A.2 Detailed 2-D FFT simulation	127
A.3 Ideal AoA simulation with skewed RX array	134

List of Figures

Figure 1: Concept of miniature collision-avoidance radar system onboard a sUAS	1
Figure 2: Damaged wing of a Piper Apache GA aircraft after colliding with a UAS	3
Figure 3: Miniature ADS-B system for transponder based collision avoidance	5
Figure 4: MIT's Drone collision avoidance camera technology	6
Figure 5: Ground base station UAS collision avoidance architecture and cover	7
Figure 6: Image of 40% Yak-54 UAV inside KU's anechoic chamber	8
Figure 7: KU's Cessna-172 used to flight test the radar system.....	9
Figure 8: FMCW operations and 2-D FFT processing.	12
Figure 9: Simulated 2-D FFT processed data showing leakage signal and target echoes.	14
Figure 10: RX antenna array spacing and geometry.....	15
Figure 11: Angle-of-arrival ambiguity cone using receiver antennas A and B.	16
Figure 12: Detailed 2-D FFT simulations.....	17
Figure 13: Expected ground backscatter signal strength.	19
Figure 14: Simulation of intruders surrounding the collision-avoidance radar system.	20
Figure 15: Maximum AoA change between radar and intruders vs range	21
Figure 16: Expected AoA estimation error in dB given detected target SNR	21
Figure 17: Brassboard radar system block diagram.....	23
Figure 18: Custom Analog Device's AD8283 multi-channel ADC board.....	24
Figure 19: Analog Device's ADF4158 FMCW waveform synthesizer evaluation board.....	25
Figure 20: VCO snubber circuit tuning.	26
Figure 21: Spectrum of the WFG chirp signal after tuning.	26
Figure 22: Timing between FMCW chirp waveforms and MUXOUT strobe.....	27

Figure 23: Ztex LX150 FPGA evaluation board with accessories	28
Figure 24: FPGA and user computer communication block diagram	29
Figure 25: Prototype TriQuint 856928 SAW bandpass filter board.	30
Figure 26: Brassboard radar assembly	30
Figure 27: Transmit chain block diagram.....	31
Figure 28: Receiver chain block diagram	32
Figure 29: Pasternack PE51057 transmit antenna	33
Figure 30: Azimuth RX antenna array.....	34
Figure 31: Elevation RX antenna array.	34
Figure 32: Block diagram of the 2-D FFT processing.....	35
Figure 33: Block diagram of radar system and loopback test setup	37
Figure 34: Brassboard radar loopback test result after 2-D FFT processing.	38
Figure 35: Chipscope plot of the 12-bit ADC output read by the FPGA.	42
Figure 36: Example of leakage MSB clipped 2-D FFT radar image.....	43
Figure 37: The same setup and processing as figure 36 but without the leakage signal.	43
Figure 38: Brassboard radar system installation onboard the Cessna 172.....	45
Figure 39: Brassboard radar test flight setup against tall tower near Linwood, KS.	45
Figure 40: Sample of brassboard radar flight test results.	46
Figure 41: Enlarged view of brassboard radar 2-D FFT processed flight test image.	48
Figure 42: Measured range to target from consecutive radar updates	49
Figure 43: Measured radial velocity from the same consecutive updates.	49
Figure 44: Measured ranges to tower vs. predicted ranges to tower based on previous doppler .	50
Figure 45: Range, Doppler and calculated AoA from brassboard radar flight test.	51

Figure 46: Miniature radar system block diagram.	53
Figure 47: AE recommended chassis for the miniature radar system.	54
Figure 48: Miniature radar RF board to TX and RX antenna connection diagram.	55
Figure 49: Miniature radar surface mount RF components evaluation board.	56
Figure 50: SAW filter performance on the custom evaluation board vs datasheet.	56
Figure 51: Miniature radar RF board.	58
Figure 52: Miniature radar TX chain block diagram	59
Figure 53: Miniature radar RX chain block diagram.....	59
Figure 54: Miniature radar IF stage amplifier and HPF.	61
Figure 55: Miniature radar digital board.....	62
Figure 56: Tuning results of the WFG voltage ramp on the new miniature radar.....	63
Figure 57: FPGA evaluation board without heat sink or breakout board.	63
Figure 58: Sample S11 of the COTS RX antenna array.	64
Figure 59: Rev1 miniature radar loopback testing results	66
Figure 60: Rev1 miniature radar flight test results from the Cessna 172.	68
Figure 61: Rev1 miniature radar roof top testing against moving cars.....	69
Figure 62: Noise floor analysis using different power supplies and waveform generators.....	70
Figure 63: Subarea of 2-D FFT radar image used to calculate the average noise floor.	71
Figure 64: Block diagram of radar digital test using arbitrary waveform generator	72
Figure 65: 2-D FFT radar image produced using the AWFG to imitate a loopback test.	73
Figure 66: ADC sampled data with and without MSB error for a sinusoidal input	73
Figure 67: 2-D FFT radar image of both RX channels with ADC MSB error fixed.....	75
Figure 68: Rev2 miniature radar loopback result showing 35 dB SNR	76

Figure 69: Calibration beacon target block diagram.....	80
Figure 70: Calibration beacon target setup on the roof of KU’s engineering build.	81
Figure 71: Calibration beacon target test setup block diagram.....	82
Figure 72: Starting orientation of the RX antenna array to the calibration beacon target	84
Figure 73: Sample 2-D FFT processed radar data from roof top calibration beacon testing.....	84
Figure 74: Scene as seen by the RX antenna array.	86
Figure 75: Estimation of range in the car measurement scene.	87
Figure 76: Sample of measured car data captured by the rev2 miniature radar system.	87
Figure 77: Rev2 miniature radar external amplifiers.....	89
Figure 78: CFAR detection example for the radar’s range-Doppler image.....	92
Figure 79: Sample CFAR processed car measurement images	93
Figure 80: Scatter plot CFAR detected cars over a 12-sec recording interval.....	94
Figure 81: Azimuth calibration target phase difference measurement from antenna pairing 1....	96
Figure 82: Azimuth calibration target phase difference measurement from antenna pairing 2....	97
Figure 83: Elevation calibration target phase difference measurement from antenna pairing 3 ..	98
Figure 84: Estimated antenna spacing of the RX antenna array.	99
Figure 85: Phase, phase difference, and angle of arrival simulations.....	101
Figure 86: AoA simulation for scewed RX array	101
Figure 87: Two samples of unwrapped, calibration beacon, phase difference data	103
Figure 88: Calibration beacon AoA fitted to ideal AoA simulation.....	104
Figure 89: Angular coverage area of each azimuth antenna pair.....	105
Figure 90: Unwrapped phase difference data for the entire $\pm 60^\circ$ elevation angular cut	107
Figure 91: Unwrapped phase differences for only $\pm 20^\circ$ elevation angular cuts.....	107

Figure 92: Range-Doppler and Azimuth AoA plots of the measured car.....	109
Figure 93: Tracking of detected target in range-Doppler with confidence levels	111
Figure 94: Estimation of the azimuth AoA of the approaching car	113
Figure 95: Interpolated ideal car location vs measured car locatoin in azimuth	114
Figure 96: Interpolated azimuth location RMSE histogram	114
Figure 97: X-axis velocity from interpolated measured car data.....	115
Figure 98: Y-axis velocity from interpolated measured car data.....	116
Figure 99: Estimation of the elevation parameters of the car measurement scene.	117
Figure 100: Interpolated ideal car location vs measured car location in elevation.....	118
Figure 101: Interpolated elevation location RMSE histogram.	118
Figure 102: Z-axis velocity from interpolated measured car data.	119
Figure 103: Tegra K1 system of systems integration diagram	122

List of Tables

Table 1: Proposed radar operating parameters.....	4
Table 2: Summary of airborne SAA technology capabilities	8
Table 3: 40% Yak-54 UAV specifications	9
Table 4: Radar waveform and data capture specifications	12
Table 5: Brassboard radar parameters.....	22
Table 6: Radar loopback parameters for figure 33	39
Table 7: Rev1 and Rev2 miniature radar parameters.....	52
Table 8: FPGA antenna selection control to RX antenna array mapping.....	55
Table 9: Rev1 miniature radar loopback parameters (figure 59).....	67
Table 10: Rev2 miniature radar loopback parameters (figure 68).....	76
Table 11: Rev2 miniature radar phase differences from loopback test setup	78
Table 12: Rev2 miniature radar system weights.....	90
Table 13: Calibration beacon data biases and adjustments for optimized AoA fitting	104
Table 14: Measured car range, Doppler, and AoA	109
Table 15: Rev2 miniature radar noise figure calculation chart.....	127

Chapter 1: Introduction

1.1 Background – Small Unmanned Aircraft Systems (sUAS)

The objective of this dissertation is to create a proof-of-concept miniaturized collision-avoidance radar system capable of being mounted onboard a small unmanned aircraft system (sUAS) and provide the aircraft with robust, airborne, sense-and-avoid capability against both cooperative and non-cooperative hazards (figure1). This capability is important because UAS's can offer significant advantages over existing manned-aircraft in many commercial, industrial and government applications. In the future, sUAS may also enable many new and valuable services that would not otherwise exist. However, their lack of situation awareness poses unacceptable societal hazards such as airborne collisions with mobile and fixed objects. There currently exists miniature, transponder-based, collision-avoidance systems for cooperative targets, however there will always exist in any airspace, non-cooperative hazards such as cellphone towers and other aircraft which must be detected using additional sensors. The miniature collision-avoidance radar developed through this dissertation is designed specifically to provide sUAS with airborne, non-cooperative target detection and location capability while

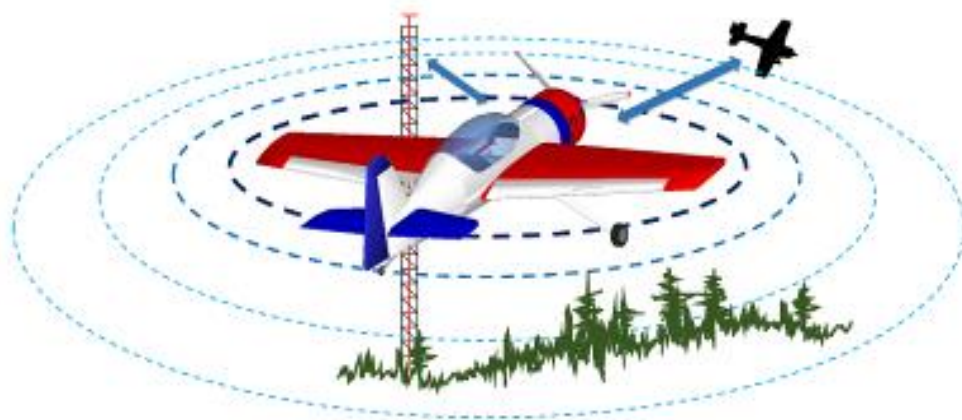


Figure 1: Concept of miniature collision-avoidance radar system flying onboard a sUAS detecting non-cooperative hazards (cellphone tower and non-responsive aircraft)

simultaneously providing redundant information on cooperative targets to further enhance their safety.

Fixed wing UAS that fall under the sUAS category weigh less than 55 lbs and have a typical payload of approximately 10 lbs or less. Given their lack of sense-and-avoid capability combined with the complexity of the U.S. national airspace system (NAS) which is the most complex in the world, the FAA has set strict regulations on UAS operating within the NAS requiring line of sight operations, flight below 400 ft above ground level (AGL), and in areas away from the general public. Once the issue of safety has been resolved and sUAS are unleashed into the NAS, the FAA predicts that these platforms will play a significant role in (but not limited to) the following commercial sectors:

- Precision agriculture
- First response
- Communications
- Infrastructure surveillance
- Package delivery
- Public safety

Agencies such as NASA, NSF, and the DOD would also like to use the sUAS for scientific or military applications in dangerous/hostile environments to carry out missions that would otherwise involve risking human life.

According to a study performed by the Association for Unmanned Vehicle Systems International (AUVSI), the ten year economic impact of UAS in the NAS would reach over \$60 billion for the U.S. These experts believe that the state of Kansas would rank amongst the top 10 states to benefit the most from this economic impact. Once again though, due to the lack of situation awareness, these economic benefits cannot be realized. Furthermore, this causes the



Figure 2: Damaged wing of a Piper Apache GA aircraft after colliding with a UAS at 2,500-ft AGL at Lewis University, Illinois in Aug, 2015 [ref 1].

U.S. to fall further behind other countries such as China which have significantly reduced regulations.

Even though these U.S. regulations are in place for safety purposes it does not mean that people will obey them. Individuals neglecting these rules have consistently made news headlines for dangerous incidences such as a collision with a manned aircraft at 2,500 ft (figure 2). Therefore, it has become urgent from both a safety and economic stand point to create sensor technology that can overcome this situation awareness barrier for sUAS; especially for non-cooperative hazards.

1.2 Radar systems

The collision-avoidance radar system offers a significant benefit over other forms of collision avoidance sensors (see section 1.3) due to its superior detection range, and all-weather, day/night capability to provide range and Doppler information of the surrounding hazards. While few radar systems may be capable of sensing non-cooperative objects for UAS collision-

avoidance, the technical barriers of size, weight and power consumption (SWaP), as well as cost, makes them unsuitable for deployment onboard commercial grade sUAS. The collision-avoidance radar system not only overcomes these issues but is capable of detection objects out to 800 m in a 360° azimuth and $\pm 15^\circ$ elevation field-of-view (exceeding that of a human pilot onboard a GA aircraft). Furthermore, the radar performs all of this without any moving parts or scanning. While a sensor suite may ultimately be required to achieve a cumulative level of situation awareness to overcome all of the FAA's concerns, a radar system such as the one developed here, will certainly be the primary sensor given its many advantages and capabilities. The radar operating requirements provided by KU's UAS experts are summarized in Table 1.

Development of the radar system was performed in two phases. Phase I was the development of a brassboard proof-of-concept radar using evaluation and connectorized components wherever possible. The radar was used to demonstrate/evaluate the radar principles and performance characteristics. Phase II involved the miniaturization of the brassboard radar system using custom electronics to demonstrate the capability of reducing SWaP to a form factor that could be flown onboard a sUAS.

Table 1: Proposed radar operating parameters

Parameter	Value
Size	6.5" x 4" x 3" (not including antennas)
Weight	< 5 lbs (including antennas and chassis)*
Power	< 20 W
Max detection range	300 m to 800 m (for 1 m ² RCS**)
Max target velocity (relative)	280 mph
Azimuth coverage	360°
Elevation coverage	$\pm 15^\circ$
Update rate	8 Hz – 10 Hz
Range resolution	10 m
Doppler resolution	10 Hz (1.4 mph)
Angular accuracy	Varies with SNR

* Assuming power drawn from the sUAS therefore not including battery weight

**RCS = radar cross section

1.3 Collision avoidance technologies

Current (2016) market solutions for sUAS airborne collision-avoidance of non-cooperative hazards are severely limited. General aviation (GA) aircraft uses the Traffic Alert and Collision System (TCAS) and Automatic Dependent Surveillance-Broadcast (ADS-B) transponder system to communicate with one another and to ground base stations. Research and development on these transponders have miniaturized them to the point where they can be installed onboard a sUAS and groups at NASA have demonstrated their functionality. While these systems work extremely well they require all aircraft and potential hazards (e.g. any tall structures) to be equipped with a transponder in order to perform cooperative collision-avoidance. As mentioned before, there will always exist in any airspace non-cooperative targets which will be undetectable by a transponder based systems and will require non-cooperative target detection capability. The benefit of the proposed radar system is that it is capable of detecting non-cooperative targets while providing redundant information (enhanced safety) for cooperative one.

Due to the low barrier of entry, there are several universities and companies investigating the use of onboard cameras for collision avoidance. While cameras designed for sUAS are

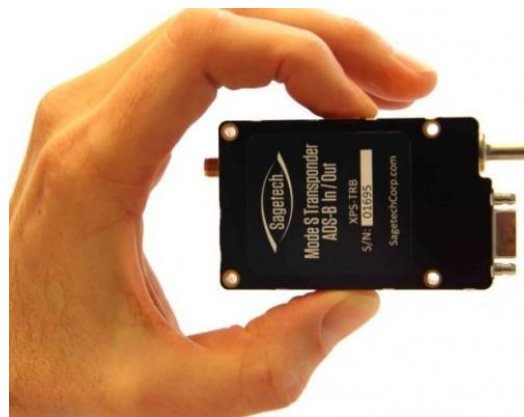


Figure 3: Miniature ADS-B system for transponder based collision avoidance with cooperative targets [ref 2].

readily available their detection capabilities are limited given the SWaP constraints of sUAS. Either mechanical scanning and/or multiple cameras are necessary to provide the same coverage as the collision-avoidance radar system (360° azimuth and $\pm 15^\circ$ elevation). The resolution of the camera(s) along with the sophistication of the image processing algorithm will limit the size and range of targets that can be spotted. Furthermore, these systems are significantly affected by weather conditions when operating outdoors. Other optical sensors such as lidar are also susceptible to weather conditions and have limited field-of-view. In contrast, the radar systems uses isotropic radiators which doesn't require any moving parts and is inherently capable of operating day/night and in all weather conditions.

A network of ground based systems providing continuous monitoring of the NAS for sUAS traffic has been proposed and studied. These stations are mostly in the form of radar and will relay messages to both the GA aircraft as well as air traffic control presumable through ADS-B. While this is feasible it cannot guarantee the same level of consistent coverage as a miniature airborne radar system directly mounted onboard the sUAS that is providing



Figure 4: MIT's Drone collision avoidance camera technology uses two cameras and two separate GPU processors to constant detect targets located specifically at 10m in front of the aircraft to provide real time collision avoidance capability [ref 3].

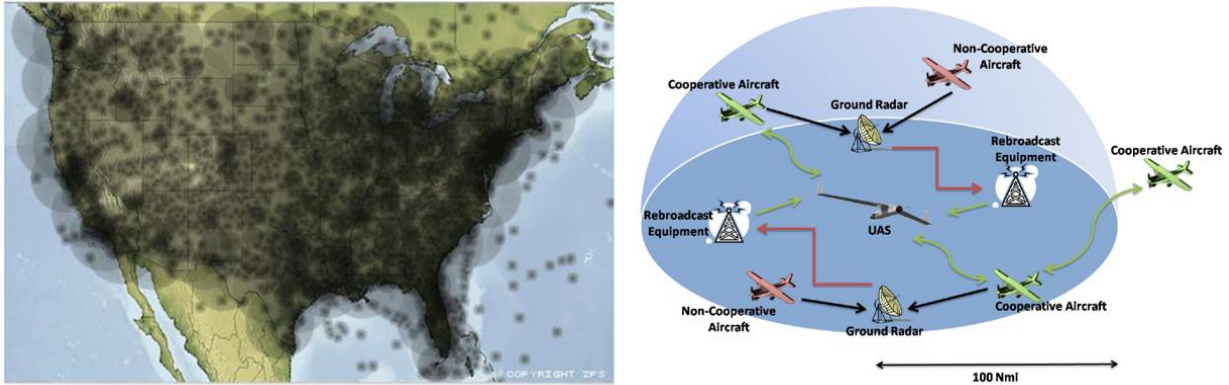


Figure 5: Ground base station UAS collision avoidance architecture and cover estimation [ref 4].

information directly correlated to the current UAS flight condition. The use of ground based systems will likely require additional human operators, congest the current flight control network, and is dependent on the reliability of relay stations to forward critical information from node to node.

In the field of radars, the University of Denver in 2014 announced the development of a miniature radar sensor targeted at quadcopters. The radar is a phased-array system costing over \$7,000 that can detect obstacles up to 100 meters in range. This detection range is not enough to allow time for collision avoidance with GA aircraft such as a Cessna 172 which has a cruising speed of 52 m/s (120 mph). Similar to the camera systems, this radar requires scanning or multiple systems to be installed on a single sUAS to provide the total coverage of the surroundings. Table 2 is a summary of all of the mentioned sensor types taking parameters from their sUAS implementation when possible.

Table 2: Summary of airborne SAA technology capabilities

	Dissertation Radar	Other Radar*	Camera	Lidar**	ADS-B
Day/night operation	Yes	Yes	NO	NO	Yes
All weather operation	Yes	Yes	NO	NO	Yes
Non-cooperative target	Yes	Yes	Yes	Yes	NO
Maximum detection range	800 m	100 m	< 800 m	75 m	> 800 m
Doppler detection capability	280 mph	N/A	N/A	Dependent	Report based
Azimuth coverage (no scanning)	360°	< 180°	120°	100°	Report based
Elevation coverage (no scanning)	±15°	unknown	±15°	unknown	Report based
Range resolution	10 m	unknown	Dependent	< 10 m	Report based
Doppler (velocity) resolution	1.4 mph	N/A	N/A	Dependent	Report based

* Other Radar from research at the University of Denver [ref 5]

** Lidar from YellowScan lidar developed for small UAS [ref 6]

1.4 Target platform and specifications

The proposed miniature radar system is designed to be flown onboard a radio controlled, commercial off-the-shelf (COTS) hobby-grade UAS that is primarily used for training and research. The 40% Yak-54 UAV (figure 5) or a similar sUAS is targeted as the final platform. Table 3 summarizes the expected sUAS operating characteristics.



Figure 6: Image of 40% Yak-54 UAV inside KU's anechoic chamber

Table 3: 40% Yak-54 UAV specifications

Parameter	Value
Wingspan	3.1 m
Length	3.1 m
Empty Weight	18.1 kg
Payload	4 kg
Cruise speed (max)	36 m/s

Initial flight testing of the radar system will be performed on a manned Cessna-172 (figure 7) which will be flown against stationary targets such as a tall radio tower. The typical cruising speed of a Cessna-172 is 120 mph (54/ms). Due to the antenna mounting limitations which will be further discussed in section 3.2, the radar will be forward looking during these manned flight tests.



Figure 7: KU's Cessna-172 with experimental classification used to flight test the radar system against a stationary structure.

Chapter 2: Radar theory and simulations

2.1 Receiver power

The collision avoidance radar is a multichannel, frequency-modulated continuous wave (FMCW) radar. FMCW radar constantly transmits swept-frequency signals known as chirps, while simultaneously receiving target echoes. This permits a large time-bandwidth product to achieve higher signal to noise ratio (SNR) with lower transmit power requirements. These radars differs from pulsed systems which turns off their receiver during the transmit portion of the pulse repetition interval (PRI) and vice versa. This act of swapping between transmit and receive mode results in a blind zone around the pulsed system that is equal to half the transmit duration times the speed of light. Given the transmit signal characteristics shown in table 4, the immediate blind zone would be at least 30,000 m; which would clearly be insufficient from a collision avoidance stand point.

The FMCW radar however faces its own set of challenges primarily in the form of the direct path leakage signal between the TX and RX. The leakage signal is many orders of magnitude greater than the echoes from a distant target which must be separated from the leakage in order to properly perform target detection. Assuming that the TX and RX antennas are relatively co-located when compared to a distant target at a range, R , the radar's received power from target echoes is given by the radar range equation [1] below.

$$P_{RX} = \frac{P_{TX} G^2 \lambda^2 \sigma L}{(4\pi)^3 R^4} \quad [1]$$

Here P_{RX} is the received echo power, P_{TX} is the transmitted power, G is the gain of the TX and RX antennas (note: assumed to be identical), λ is the wavelength of the radar signal, σ is

the radar cross section (RCS) of the target, and L accounts for any additional losses ($L < 1$). The received power of the leakage signal can be calculated through Friis' equation [2] below.

$$P_{Leakage} = \frac{P_{TX} G^2 \lambda^2 L}{(4\pi)^2 R_{ant}^2} \quad [2]$$

Here $P_{Leakage}$ is the power of the leakage signal, P_{TX} is the transmitted power, G is the gain of the TX and RX antennas (again assumed to be identical), λ is the signal wavelength, L is any addition losses, and R_{ant} is the distance between the TX and RX antennas. Notice that the range, R_{ant} , is on the order of 1 – 2 meters since both the TX and RX antennas are installed onboard the same sUAS while the range to the target, R from equation [1], is on the order of 300 to 800 meters according to radar target detection range (table 1). Furthermore, the power of the leakage signal only experiences a R_{ant}^2 and $(4\pi)^2$ loss term in the denominator of equation [2] vs the power of the target echo, P_{RX} which experiences R^4 and $(4\pi)^3$ loss terms. Once again, separating the leakage signal from the weaker target signals is critical in properly detecting collision hazards. This is performed using a 2-D Fast Fourier Transform (FFT) process that is explained in the following section.

2.2 Radar range and Doppler processing

This section walks through the data capturing, formatting and 2-D FFT processing of the collision avoidance radar system. Table 1 lists all of the radar waveform and sampling specifications and figure 8 illustrates the theory behind generating the beat frequency, sampling, and data gathering in preparation for the 2-D FFT processing.

Table 4: Radar waveform and data capture specifications

Parameter	Value
Signal type	Up Chirp
Transmit frequency (bandwidth)	1.445 GHz – 1.450 GHz (15 MHz)
Transmit duration (PRI)	200 μ s (4 kHz)
Sampling frequency	4 MSa/s
Fast time samples	800
Slow time samples	500

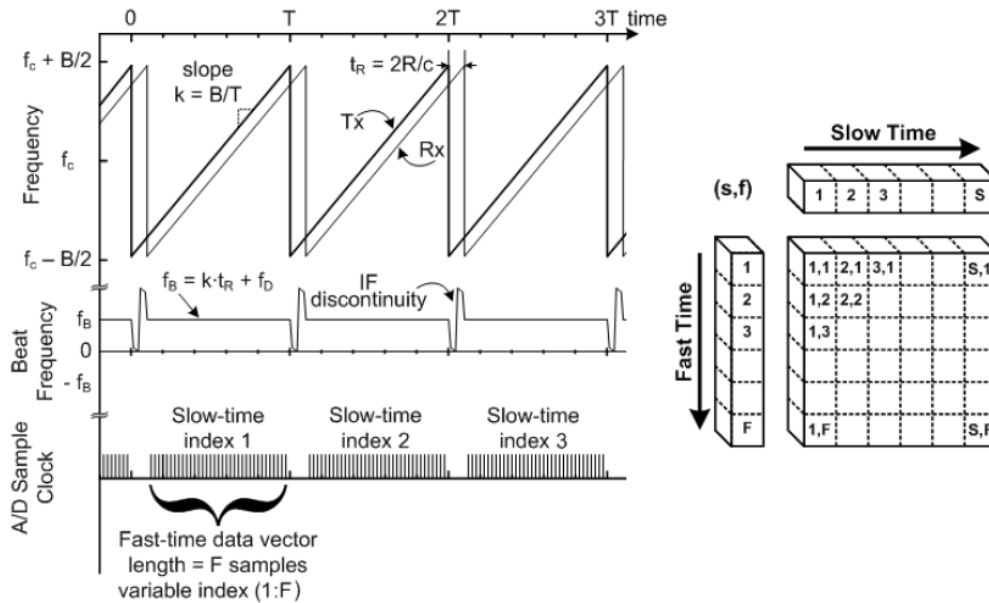


Figure 8: FMCW operations and 2-D FFT processing.

(Left) Transmit and receive chirp signals mixing to create a beat frequency that is then sampled using a synchronous A/D. Samples from each chirp is used to fill a slow time indexed column in a data matrix. Once the matrix is completely filled FFTs are performed across both the rows and columns of the matrix to complete the 2-D FFT radar processing.

The radar receive process begins by performing IF down conversion using an analog mixer to beat the RX echoes against the transmitted chirp, TX (figure 8). Since the received echo, RX, is delayed in time due to the round trip propagation to the target and the chirp signal is a linear frequency sweep, the resulting beat frequency, f_B is a constant sinusoid whose frequency is directly related to the range to the target by:

$$f_B = \frac{2RB}{c\tau} \quad [3]$$

Where R is the range to the target, B is the bandwidth of the chirp signal, c is the speed of light, and τ is the waveform duration. This means that the range to the target can be directly calculated from f_B .

Given that the chirp signal has a duration of 200 μs , 15-MHz bandwidth, and the maximum detection range is 800 m, the expected maximum f_B is 400 kHz. This process of generating f_B using analog components is also critical for reducing the analog-to-digital converter (ADC) sampling requirements. Since a maximum beat frequency of 400 kHz is expected, the ADC sample rate only needs to be greater than 800 kHz to satisfy the Nyquist criteria. In practice, the radar samples the beat frequency at 4 MSa/s resulting in 800 samples per 200- μs transmit.

The 800 samples for a single transmit are stored as a column of fast-time data in the data matrix shown in the right of figure 8. The 800 samples from the subsequent transmit is stored in that adjacent fast-time data column. This process repeats until 500 total transmits and therefore, 500 columns of fast-time data has been gathered, filling up the entire data matrix. A Hanning window is then applied across both the column and row (slow-time) dimensions followed by FFTs across both dimensions as well. The Hanning window is important because it reduces the sidelobes from the leakage signal which would otherwise mask the target's weak echo. This results in the 2-D FFT processed radar data shown in figure 9 where the fast time columns now represent range and the slow time rows now represent Doppler or radial velocity.

The 2-D FFT is a coherent process which yields a range-Doppler mapping of received energy. Theoretically, the 800 x 500 points of coherent integrations should provide 56 dB of SNR improvement. However, in practice a 1-MHz anti-aliasing filter is implemented in the ADC prior to sampling the fast time signals and noise at 4 MSa/s. This 2x over sampling (note:

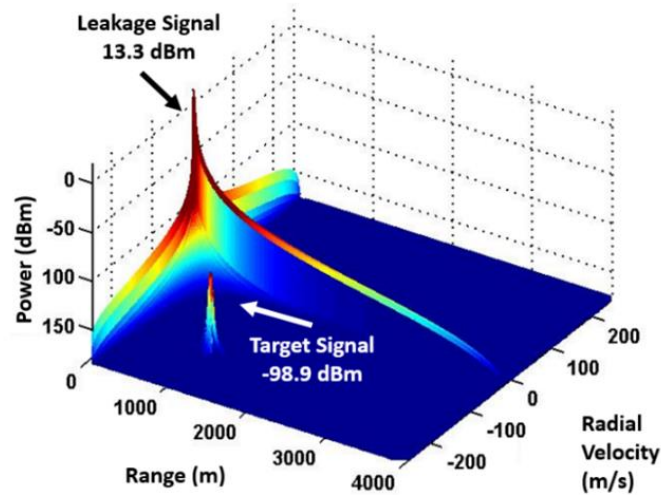


Figure 9: Simulated 2-D FFT processed data showing leakage signal and target echoes.

2 MSa/s Nyquist sampling requirement) means that the noise samples are not truly independent which reduces the SNR improvement from the 2-D FFT process by 3 dB resulting in 53 dB SNR enhancement.

One of the critical outcomes of the 2-D FFT process is the offset in range and Doppler of the target echoes from the leakage signal and its sidelobes. Since the transmitter and receiver are within close proximity of each other and have no relative motion to one another, the leakage energy is mapped to zero range and zero Doppler pixel. Due to the strength of this signal, the side-lobes (even after Hanning windowing) extends out across the zero range and zero Doppler axes and is still strong enough to challenge the pulse compressed target echoes. However, since the targets are not located at zero range and have motion relative to the RX antenna array (i.e. non-zero Doppler), their pulse compressed energy is offset in both range and Doppler from the leakage signal and its sidelobes. This separation of the target echoes from the known behavior of the leakage is what allows the radar to detect targets using this FMCW radar architecture. Figure 9 is a simulation result which illustrates this concept of separating the target from the leakage using 2-D FFT processing.

2.3 Angle of arrival processing

The TX antenna for the radar system is a single isotropic radiator to transmit the radar signal in all directions. The RX antenna array comprises of four isotropic antennas, three of which are in an equilateral triangle formation in the azimuth plane and the last antenna is stacked on top or below one of the azimuth antennas. Ideally, all antennas are spaced half-wavelength apart from each other as shown in figure 10.

Using this RX array setup, interferometry can be performed using the detected target's phase difference between RX antennas. Given the known spacing between antennas, the phase difference can be used to calculate the angle-of-arrival (AoA) of the target echo using equation [3] and referencing figure 11.

$$\theta_{AB} = \cos^{-1} \left(\frac{\lambda \delta_{AB}}{2\pi d} \right) \text{ [rad]} \quad [3]$$

From equation 3, the incoming signal's AoA is measured as, θ_{AB} , off of the baseline between antennas A and B (figure 11). This is obtained by using the measured target phase

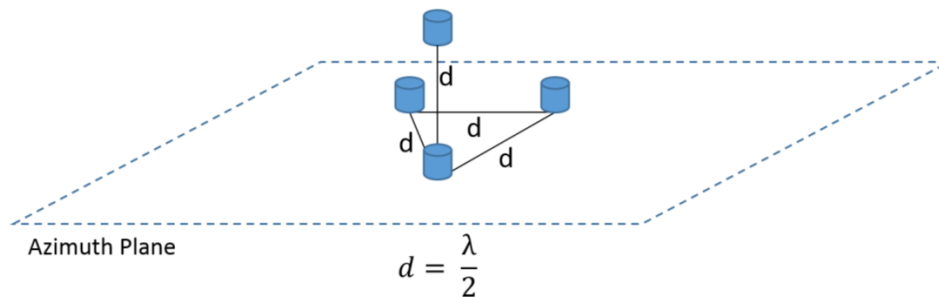


Figure 10: RX antenna array spacing and geometry.

Three RX antennas in an equilateral triangle in the azimuth plane and one RX antenna vertically offset in the elevation plane directly above one of the azimuth antennas. All antennas are spaced half-wavelength apart.

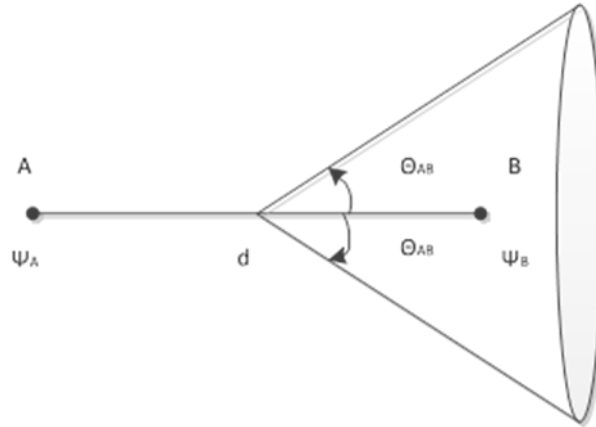


Figure 11: Angle-of-arrival, θ_{AB} , ambiguity cone given phase difference δ_{AB} between receive antenna A and B.

between the two RX antennas, δ_{AB} , the separation between the two antennas, d , and the wavelength, λ , and inserting them into equation [3]. Using two RX antennas, there is an ambiguity about the baseline which locates the target on a circle whose diameter is related to the range to the target. With the three RX antennas in the azimuth plane, this ambiguity can be resolved to a single Azimuth AoA. Only two vertically stacked antennas are needed to unambiguously determine the elevation AoA since it is only a matter of whether the target is above or below the horizontal plane of the aircraft. Combining the unambiguous azimuth and elevation AoA of the target with the range to the target should theoretically allow the radar to identify the location of the target in 3-D space relative to the radar RX antenna array.

2.4 Simulations

Detailed 2-D FFT process

Simulations played a critical role in verifying the proposed radar theory and validating the hardware performance. The first simulation was performed by Dr. Chris Allen which created the range-Doppler map from ideal 2-D FFT processing in a noiseless environment is shown in

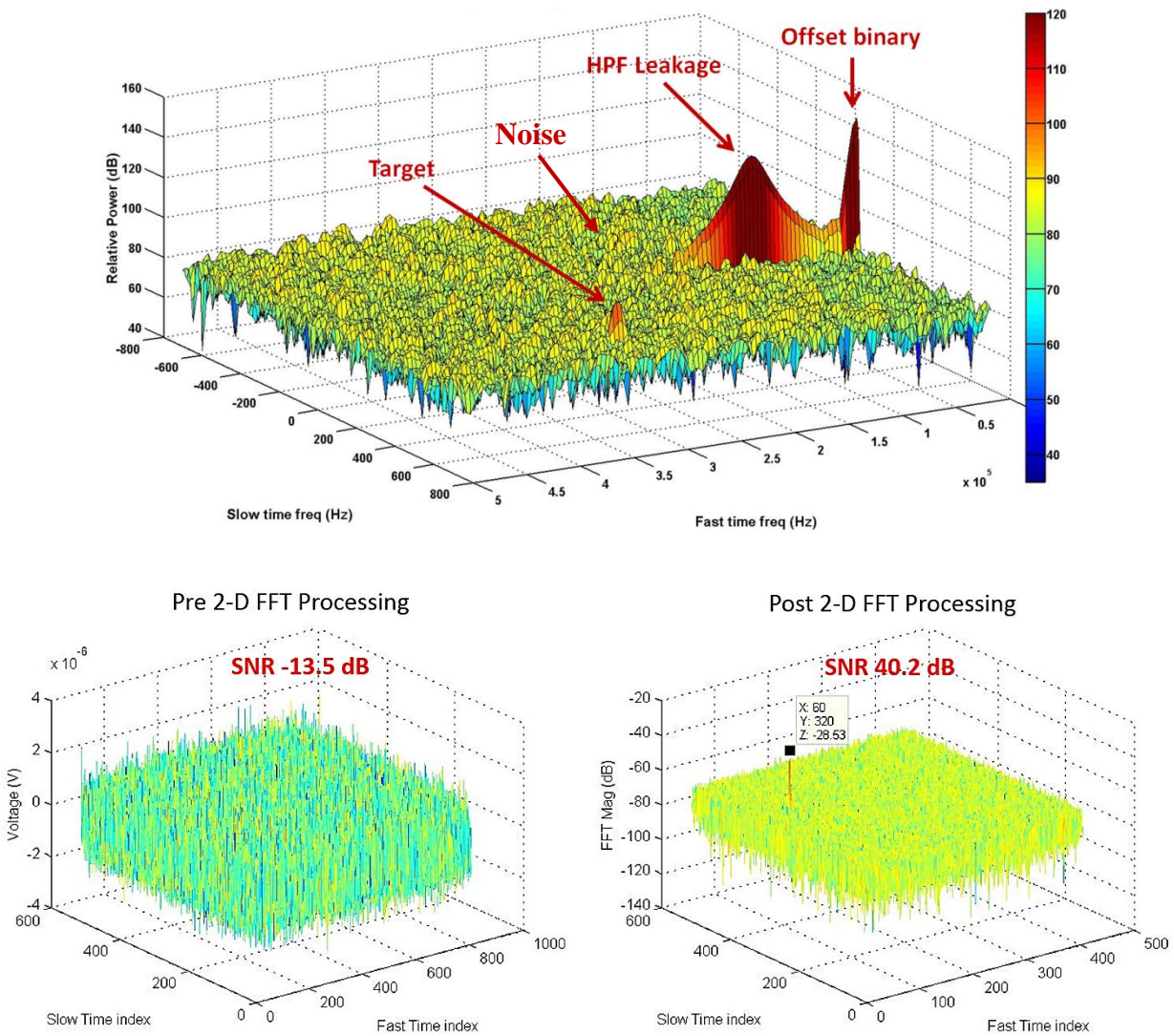


Figure 12: Detailed 2-D FFT simulations

(Top) Simulation of the brassboard radar system with signal, noise, leakage, and quantizing effects. (Bottom) Simulation of pure 2-D FFT processing gain showing 53.7 dB SNR improvement. Note that the theoretical gain is 56 dB but since the simulated signal is a real sinusoid, the peak power is reduced by 3 dB since there is a real and imaginary component to the FFT result.

figure 9 where the separation of the weak target echoes from the leakage can be clearly seen. As the radar development progressed, the complexity of the simulation was expanded to incorporate the effects of noise, leakage and various quantization effects. Figure 12 shows the results of an advanced version of the radar 2-D FFT simulation. Figure 12, top, is a simulation that shows the incorporation of leakage, Hanning windowing (via a lookup table), ADC (in offset binary mode),

and quantization effects resulted in a 1.58-dB degradation of the SNR when compared to just signal and noise (without quantization effects). Figure 12 bottom, is a detail simulation that demonstrated the 2-D FFT SNR gain. The simulated input signal power was -124 dBm while the input noise power was -110.5 dBm; calculated from $P_{\text{noise}} = kT_0BF$ where k is Boltzmann's constant, T_0 is absolute RX temperature of 290 K, B is the receiver IF bandwidth (1-MHz) and F is the noise figure of 3.5 dB [7]. The results showed 53.7 dB SNR improvement after 2-D FFT processing. Note that the IF signal used in the simulation is a real valued sine wave, the FFT of which has a positive and negative frequency component. Shown in figure 12 bottom is only the positive portion thus the peak is 3 dB lower; this means that the 2-D FFT processing actually produced 56.7 dB SNR improvement which matches the theoretical 56.1 dB.

Ground clutter

Simulations were also used to determine the effects of ground echoes on the radar operations. Since the radar is in constant motion, echoes from the ground will have both a range and Doppler component offsetting it from the leakage signal. Figure 13 shows the simulated ground echo strength in range and Doppler. Note that specific to this simulation, the aircraft is assumed to be flying 150-m AGL with a radar that transmits 1 dBm of power using a dipole antenna for both TX and RX. The ground's backscatter coefficient, σ^0 , is estimated to be $10\cos(\theta)$, where θ is the incidence angle. From this simulation it was concluded that the echoes from the ground would significantly affect the ability to detect targets that also occupies the same range-Doppler bin. This is especially true for the AoA estimations process where the phase content is easily corrupted by the ground echoes. Therefore, the radar system, though designed

to detect targets out to a maximum of 800 m, is only capable of reliably detecting targets out to the same distance as its height AGL.

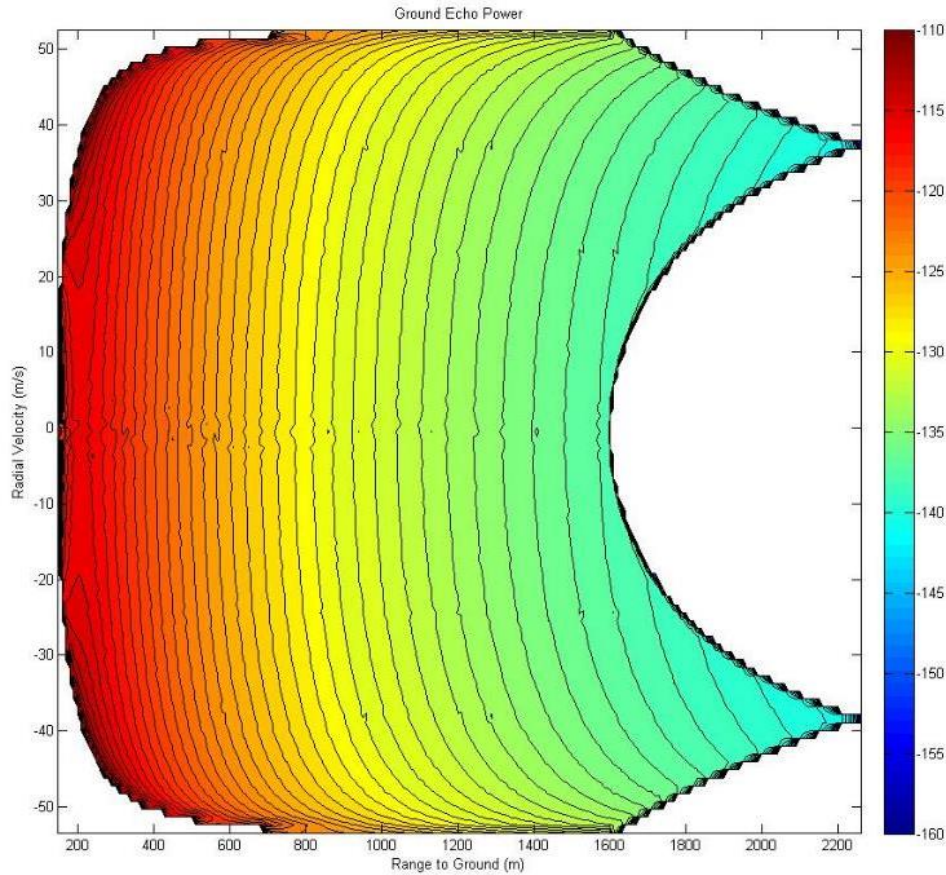


Figure 13: Expected ground backscatter signal strength.

Assuming a radar height of 150-m AGL and a 1 dBm transmit power. This signal strength rivals that of a target echo and will significantly affect the AoA detection capability by corrupting the target's phase information.

Physical geometries

The last simulation is to analyze geometrically what are the limits to target angular change between radar updates (recall the radar's target update rate is 10 Hz). This simulation result became even more critical after realizing the hardware limitations of the proof-of-concept radar system both in terms of reducing the number of RX channels and slowing the update rate. The

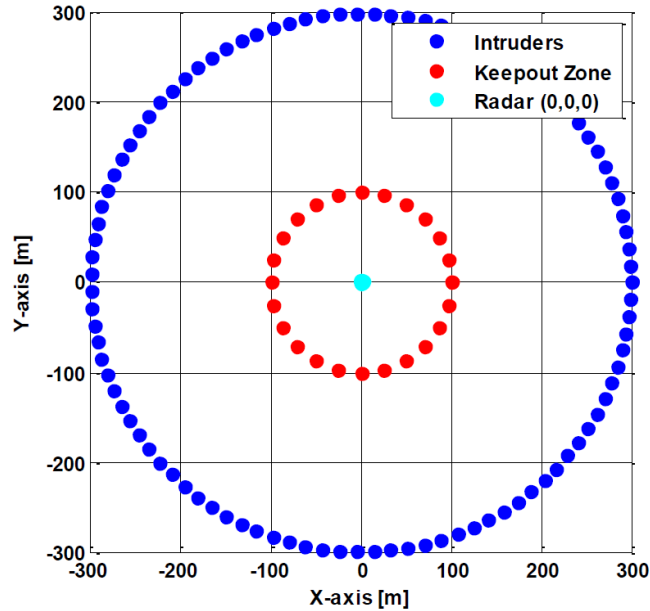


Figure 14: Simulation of intruder located at 300 m surrounding the collision-avoidance radar system. The relative speed of the intruders to the radar is 90 m/s (200 mph) with all intruders moving in the positive X direction [ref 7].

initial simulations were performed by Mikhail (Mike) Zakharov in his Master's thesis from The University of Kansas [ref 7]. Zakharov's simulation involved a ring of intruders located 300-m away from the radar system moving toward the negative x -axis direction at a velocity of 56 m/s. The radar was simulated to move in the positive x-axis direction at 36 m/s (figure 13). The two major pieces of information from this simulations is: 1. the maximum AoA rate of change is approximately $0.6^\circ/100$ ms (i.e. 0.6° per radar update at a 10 Hz) and 2. the AoA estimation error is a heavily dependent on the target SNR which will affect the ability to perform 6-degrees of freedom (6-DOF) target motion calculations. Figure 14 illustrates the simulation setup, figure 15 is a graph of the maximum expected AoA change assuming a 10 Hz update rate, and figure 16 shows the SNR dependency of the AoA estimation error.

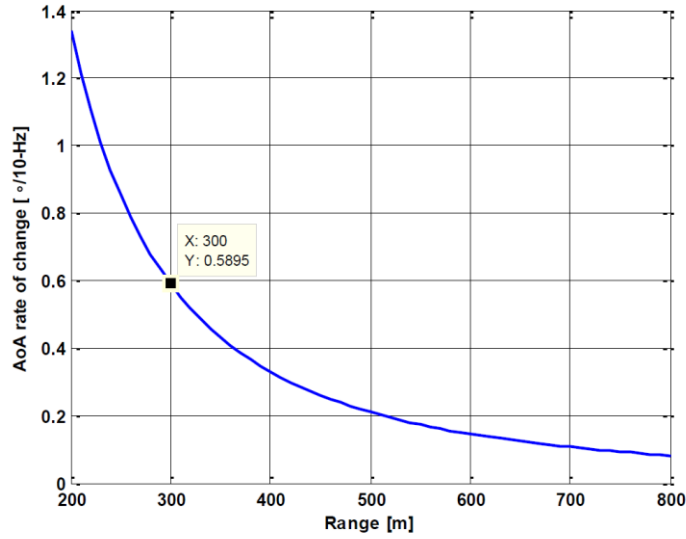


Figure 15: Maximum AoA change between radar and intruding target at various ranges assuming a radar update rate of 10 Hz [ref 7].

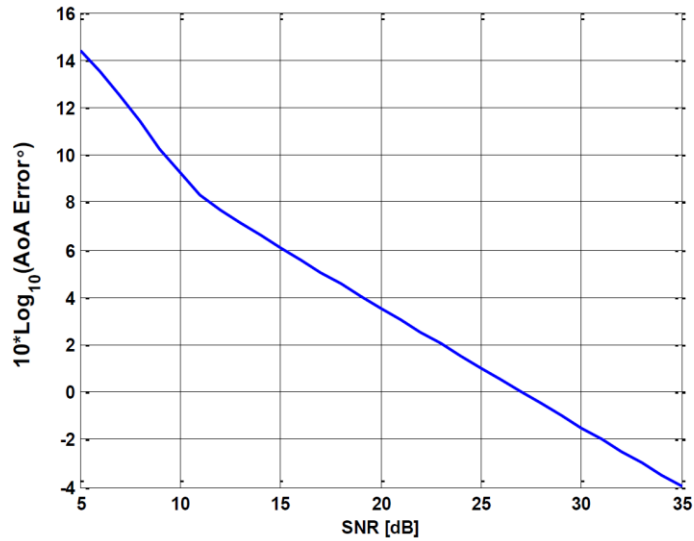


Figure 16: Expected AoA estimation error in dB given detected target SNR. This will affect target 6-DOF estimations [ref 7].

Chapter 3: Brassboard proof-of-concept radar

The brassboard proof-of-concept radar was designed and developed using NASA LEARN I funding from 2012 – 2013. This radar was a large prototype created primarily from evaluation components whenever possible. In its final form the radar had the following parameters listed in table 5. Note that there are large discrepancies between the brassboard radar's parameters versus the initial design specifications in table 1, primarily transmit duration, update rate, and number of receiver channels. This section will describe the hardware and software development as well as the limitations which resulted in descopeing the radar performance.

3.1 Brassboard radar hardware

The hardware development of the brassboard radar was broken down into five primary subcomponents. These are the ADC, the waveform generator (WFG), the field programmable gate array (FPGA), the RF assembly, and the TX/RX antennas. Figure 17 shows a block diagram of these components on the brassboard radar system that will be discussed in this section.

Table 5: Brassboard radar parameters

Parameter	Value
Radar type	FMCW
Center frequency	1.445 GHz
Bandwidth	15.7 MHz
Transmit duration	254 μ s (210 μ s chirp & 44 μ s delay)
Fast-time data capture duration	200 μ s
Slow-time samples	512
Update rate	2 Hz
Transmit power	0.32 W (25 dBm)
Sampling frequency	4 MSPS / channel
Range resolution	9.55 m
Doppler resolution	9.77 Hz (1.01 m/s)
Transmit antenna	Monopole (COTS)
Azimuth receive antenna	3 element monopole array
Elevation receive antenna	2 element dipole array
Active receiver channels	2 per update

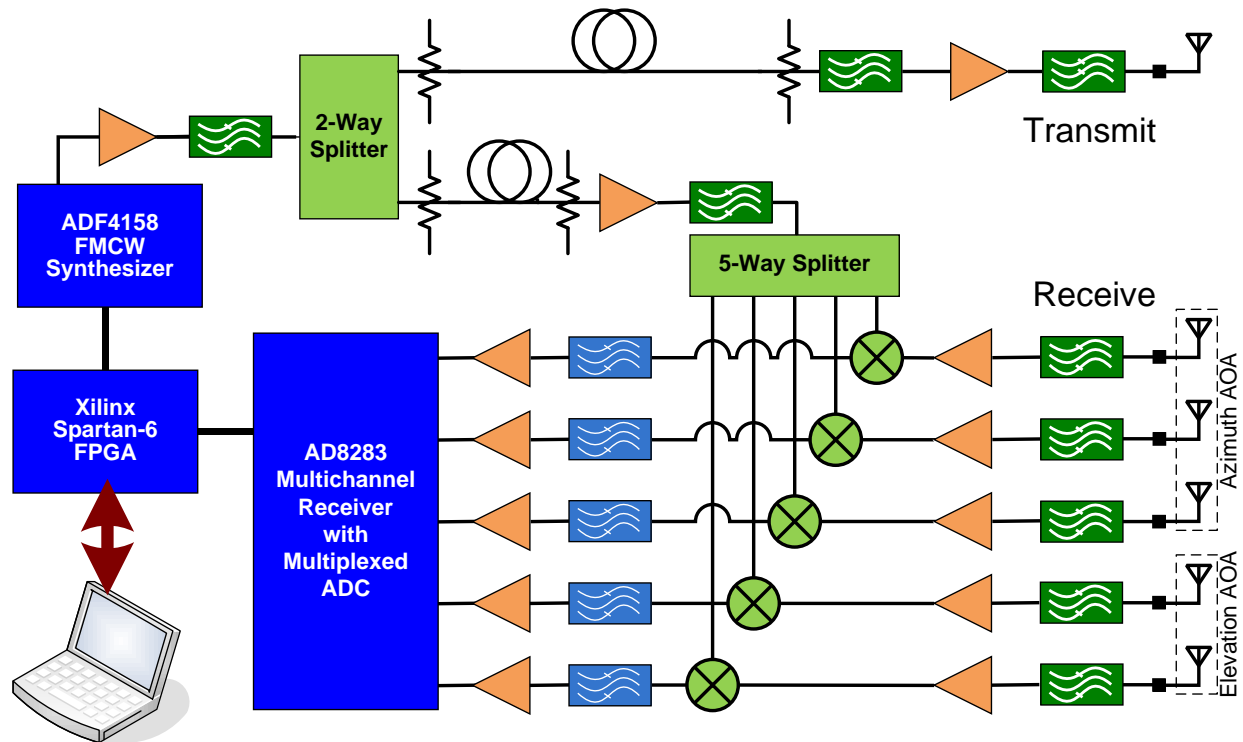


Figure 17: Brassboard radar system block diagram

3.1.1 Analog-to-digital converter

The ADC chosen for this radar is Analog Device's AD8283 6-channel analog-to-digital converter. This chip contains a 12-bit, parallel output ADC with 6-multiplexed input channels each with its own low-noise amplifier (LNA), programmable gain amplifier (PGA), and 3rd order elliptical antialiasing filter (AAF). Five of the six ADC channels are utilized at a sampling rate of 4 MSa/s. Given this sample rate the AAF is automatically set by the integrated circuit (IC) internal logic to 1 MHz and, after experimenting with the completed system, the internal PGA was set to 34 dB. The ADC settings is programmed by the FPGA through a SPI bus and it also takes in a 20-MHz clock (5 channels x 4 MSa/s) from the FPGA to remain synchronous to the rest of the radar's digital system. This is critical for coherent pulse compression during the 2-D

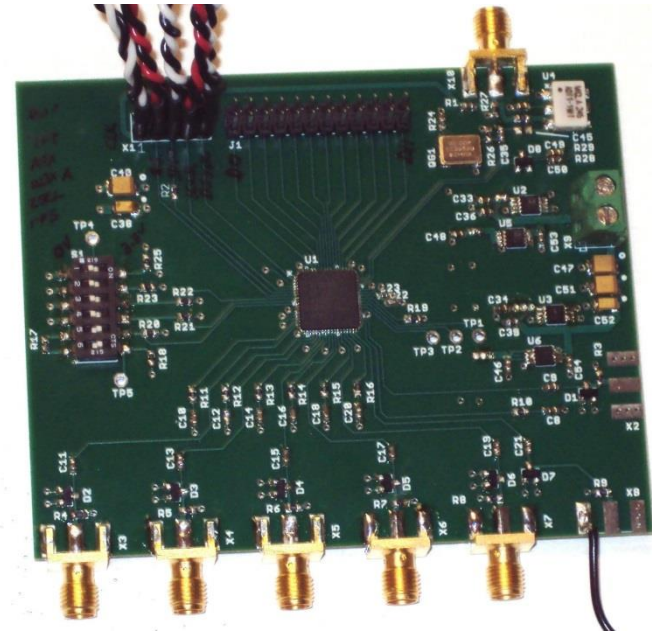


Figure 18: Custom Analog Device AD8283 multi-channel ADC board
The ADC produces a 12-bit parallel output and has built in LNA, PGA, and AAF per channel.

FFT process. An evaluation board for this ADC did not exist at the time of the project and a custom ADC board was created and tested for the brassboard radar (figure 18).

3.1.2 Waveform generator

Analog Device's ADF4158 FMCW waveform synthesizer is used as the brassboard radar's WFG. This is an IC designed for the automotive collision-avoidance market and comes with an evaluation board that operates at 5.8 GHz (figure 19). The evaluation board comes with Analog Device's software that allows the user to control the characteristics of the generated signal through a USB connection. In order to make the evaluation board function at 1.445 GHz, the 5.8-GHz VCO was replaced with Z-Communications' V602ME40-LF, an equivalent VCO that worked from 1.4 GHz to 1.624 GHz.



Figure 19: Analog Device ADF4158 FMCW waveform synthesizer evaluation board. Modifications were made to the VCO and snubber filter to produce a 15-MHz chirp centered at 1.445 GHz.

The evaluation board was also originally designed for long transmit durations on the order of milliseconds. When reprogrammed to a PRI of 200 μ s, the voltage ramp sent to the VCO contained a significant amount of transients resulting in a non-linear chirp signal. A large amount of time was spent tuning the snubber circuit on the voltage ramp output to reduce the transient duration. In the end the transients were tamed using a combination of modified RC values in the snubber circuit along with a programmed extra delays between consecutive chirp signals. Figure 20 shows the before (top) and after (bottom) images of the VCO voltage ramp. Note that there is still a section of nonlinearity in the waveform between each voltage ramp which was measured to be roughly 50- μ s long. Furthermore, the actual radar chirp signal was extended to 210 μ s in duration and 15.7-MHz bandwidth to ensure that a window existed for a

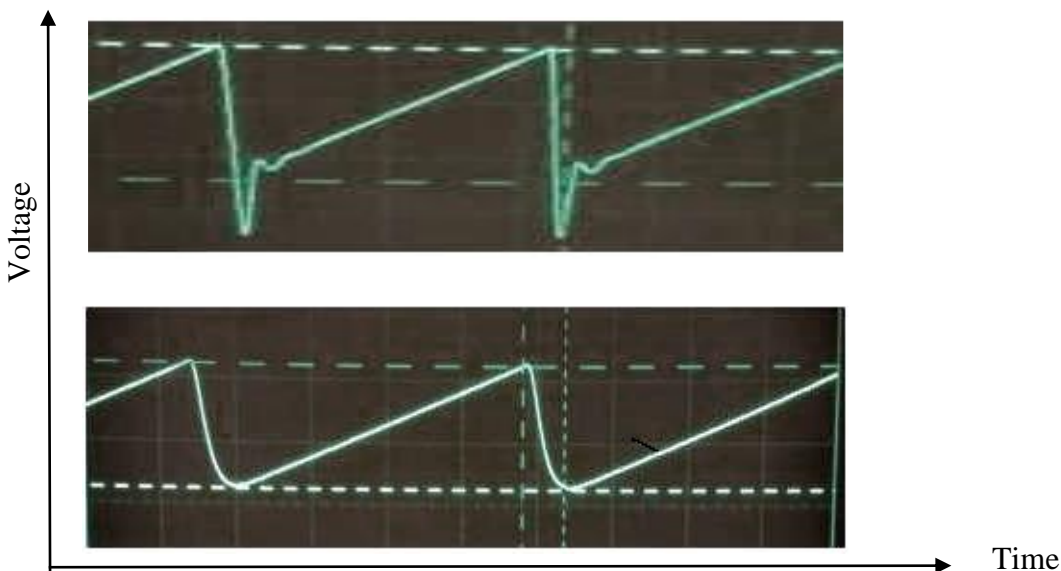


Figure 20: VCO snubber circuit tuning.

(Top) VCO voltage ramp with unmodified snubber circuit showing large transients. (Bottom) Voltage ramp after modification to snubber circuit and introduction of delay between transmits showing reduced transients and faster ramp recovery time.

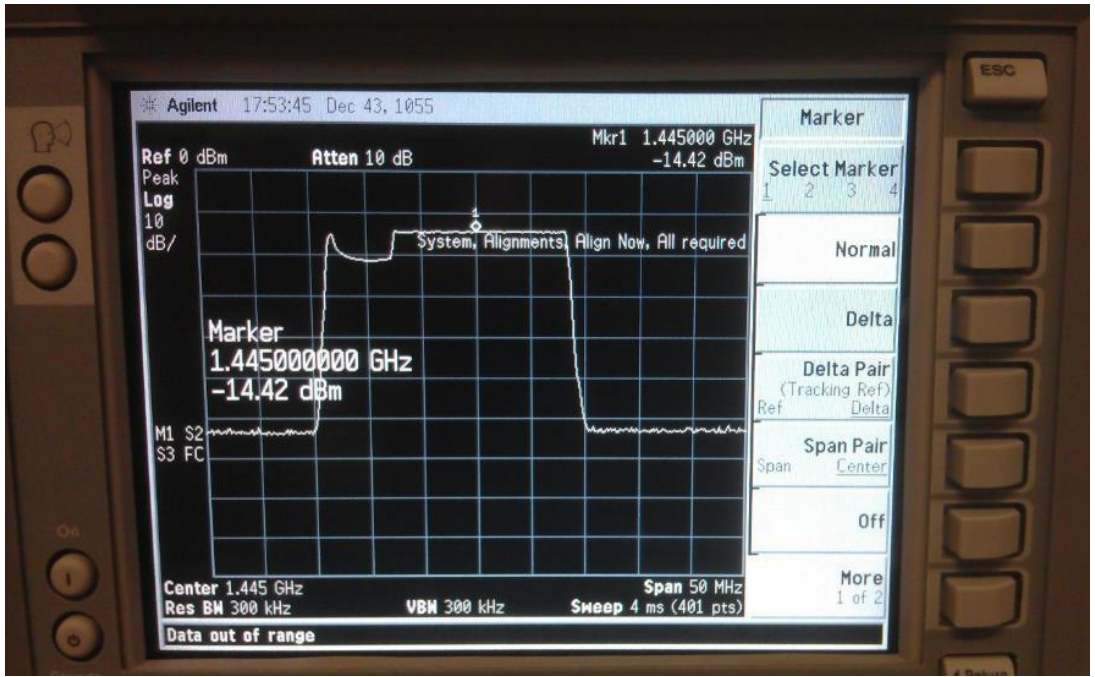


Figure 21: Spectrum of the WFG chirp signal after tuning.

The spectrum shown is captured using the spectrum analyzer max hold function. The additional spurious signal in the lower frequency range is attributed to the non-linearity in the voltage ramp reset. The 50 μ s of data thrown out at the start of each PRI is to discard this frequency section.

clean chirp signal of 200 μs to be sampled. Adding all of these extras times together, the final transmit signal had a PRI of 254 μs during which the first 50 μs and the last 4 μs of sampled data are thrown out leaving the middle 200 μs as samples from a single, clean, fast-time TX.

Figure 21 shows the spectrum of the generated chirp signal centered at 1.445 GHz using the spectrum analyzer's max hold function. Notice that the lower end of the chirp signal contains extra spurious signals which is likely due to the reset duration of the voltage ramp.

The FPGA was used to produce a 10-MHz clock signal to the WFG which in turn produced a "transmit strobe" signal back to the FPGA to indicate when a new chirp had begun. This strobe was called MUXOUT, because it was produced from the MUXOUT port of the ADF4158 IC. The timing relationship between the MUXOUT strobe and the generated signal is shown in figure 22. At the start of each MUXOUT strobe, the radar would wait 50 μs for all non-linearity to pass before starting its 200 μs of data capture from the ADC.

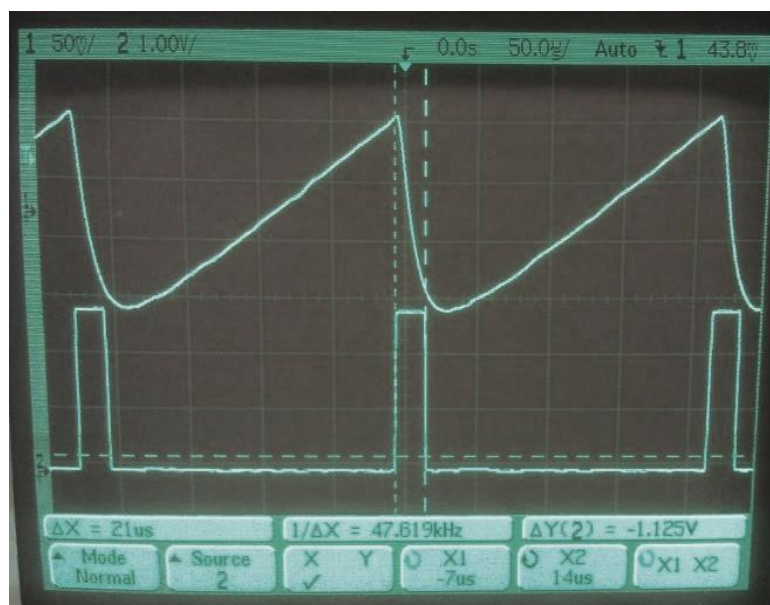


Figure 22: Timing relationship between the FMCW chirp waveforms and the MUXOUT strobe. After each rising edge of the MUXOUT strobe the FPGA would wait for 50 μs to allow all non-linearity to pass before accepting ADC data.

3.1.3 FPGA

The FPGA is the core of the radar digital system which controls all of the other digital hardware (ADC, WFG, and RF switches) as well as performs the necessary signal processing. For this brassboard radar, the Ztex LX150 evaluation board with a Xilinx Spartan-6 FPGA and built in 128-MB DDR2 SDRAM is used at the recommendation of Robert Young and the KU Instrument Design Laboratory. This board contains 99 GPIOs, a USB 2.0 interface, and an expansion microSD memory slot. Figure 23 shows an image of the Ztex LX150 evaluation board sitting on top of an IO breakout board which in turn sits on top of a custom power/IO board.

Due to RAM limitations, the brassboard radar's FPGA code is written in VHDL for a 2-channel receiver and uses a modular architecture that can be expanded to multiple channels in

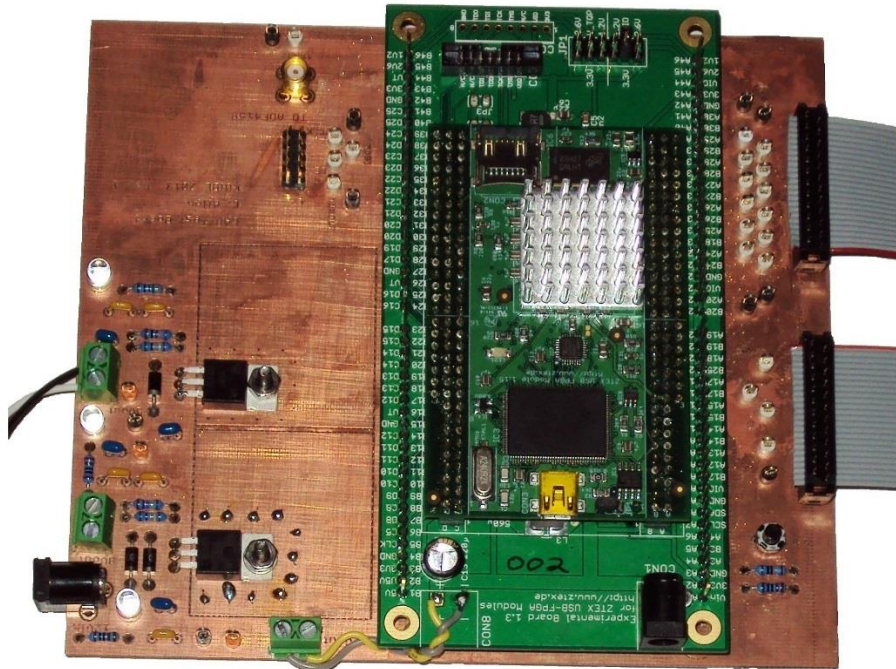


Figure 23: Ztex LX150 FPGA evaluation board with IO breakout board and custom power/IO board. The custom power/IO board also contains the necessary interface to the ADC and WFG.

the future. Surrounding the primary VHDL radar code is a Picoblaze microprocessor (also created within the FPGA) which handles communication between the radar's VHDL code and the USB interface to an external user computer. On the user computer side, Java code was written to interface with the FPGA allowing the user to program the FPGA through the USB connection and to read and record the FPGA's processed radar data to the computer's hard drive. The architecture of this setup using Java script, a Picoblaze microcontroller, and VHDL blocks was created by Robert Young of KU's Instrument Design Laboratory (IDL) and is shown as a block diagram in figure 24. Section 3.2 will explore the processing steps within the VHDL code and limitations in more detail.

3.1.4 RF assembly

The RF assembly can be further split into two branches, the transmit chain and the receive chains. For the brassboard radar, both RF chains are made entirely out of COTS components with the exception of the TriQuint 856928, RF surface acoustic wave (SAW) bandpass filters shown in figure 25.

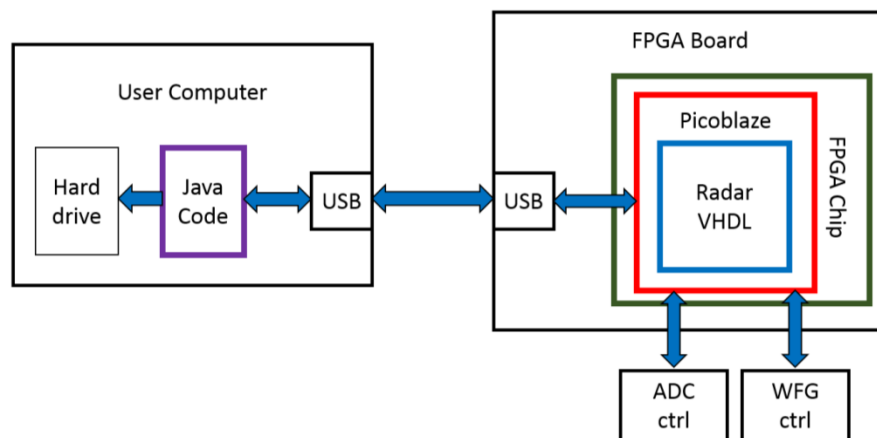


Figure 24: Block diagram of the communication architecture between the radar FPGA and the user computer. Note that all critical radar control and processing functions are contained within the “Radar VHDL” block.

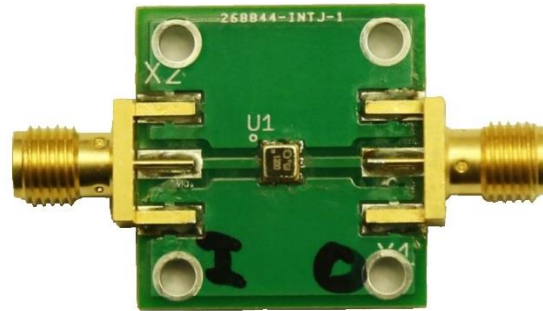


Figure 25: Prototype TriQuint 856928 SAW bandpass filter board. Center frequency of 1.445 GHz with a passband of 35 MHz and approximately 20 dB out of band attenuation.

The RF components for both TX and RX chains were assembled on an aluminum plate along with the digital devices (FPGA, ADC, and WFG). Figure 26 shows the final assembly of the brassboard radar system excluding the TX and RX antennas.

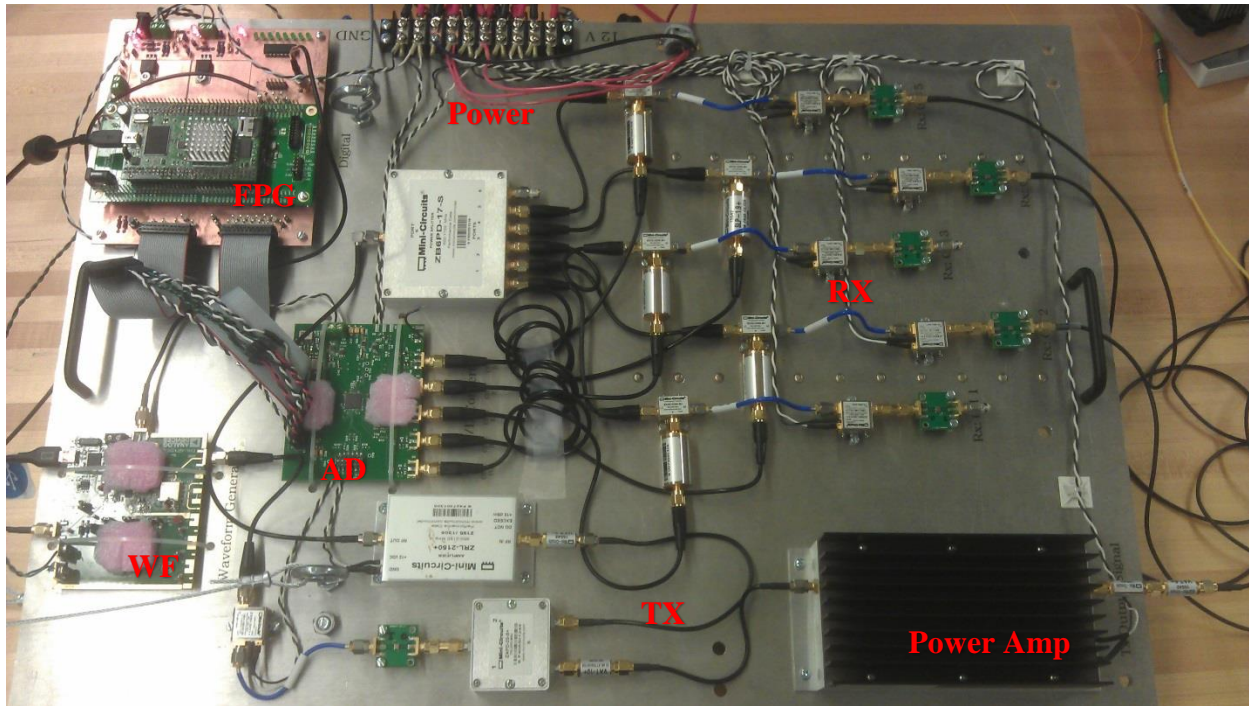


Figure 26: Brassboard radar assembly including all RF components, FPGA, ADC, and WFG.

Figure 27 is a detailed block diagram of the transmit chain showing individual component gain, attenuation, and expected signal strength along the path. The TX starts with the output from the WFG at -9 dBm and ends with a +25 dBm signal being sent to the TX antenna. Also included in the block diagram but not implemented is a variable length of TX cable that can be inserted to match the TX to RX antenna separation which would effectively guarantee that the leakage signal beat frequency is mixed down to DC. The limiting factor in the TX chain is the 1-dB compression point of the final power amplifier in the chain.

Figure 28 is a detailed block diagram of the receiver chain of the brassboard radar. Though five channels were built, only two channels were ever used due to limitations in the FPGA's internal block memory. The signal coming into the top of the block diagram is the portion of the transmit waveform that is split off of the TX chain and used for IF down conversion. The -12-dBm input into the RX chain (figure 28, right) is the expected leakage signal strength. This value was obtained from antenna coupling measurements taken onboard the Cessna 172 once the antenna mounting positions had been determined (section 3.4).

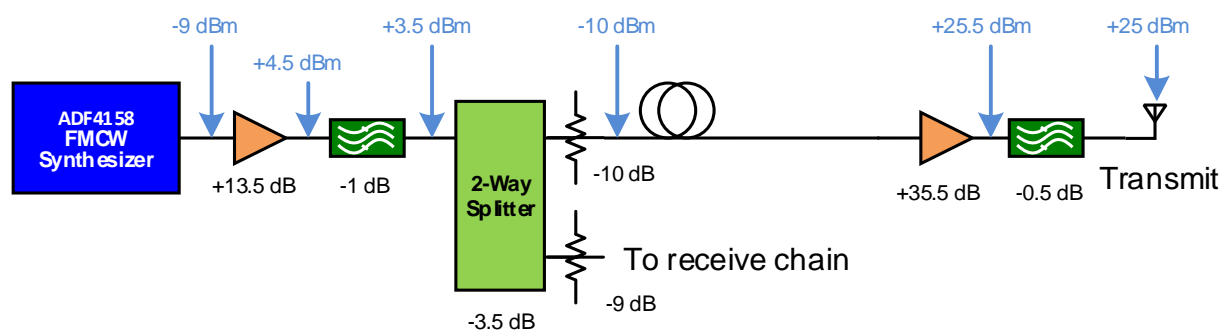


Figure 27: Transmit chain block diagram showing gain and attenuation (black) and signal strength (blue). Note that a portion of the transmit signal is split off and set to the receiver chains for analog IF down conversion.

172, see figure 29. The receive antennas were custom designed as two separate antenna arrays by two different graduate students. The azimuth RX antenna array was designed by Francisco Florencio using HFSS and comprises of three, quarter-wave monopoles in a tripod setup above a copper ground plane. The antennas were spaced apart by 10 cm and were fed by SMA connectors that extended out the bottom of the ground plane (figure 30). This antenna array was fabricated by the KU EECS shop [ref 8].

The elevation RX antenna array was designed by Nahal Niakan also using HFSS and comprised of two electrically small dipole antennas whose spacing between center points was 8.85 cm (note: half-wavelength is 10.38 cm). This design was a compromise in an attempt to make the vertical antenna array fit onboard the 40% Yak-54 UAS near the tail of the aircraft [ref 9]. The antenna was professional fabricated by Sierra Proto Express as a two layer board on FR-4 substrate (figure 31).

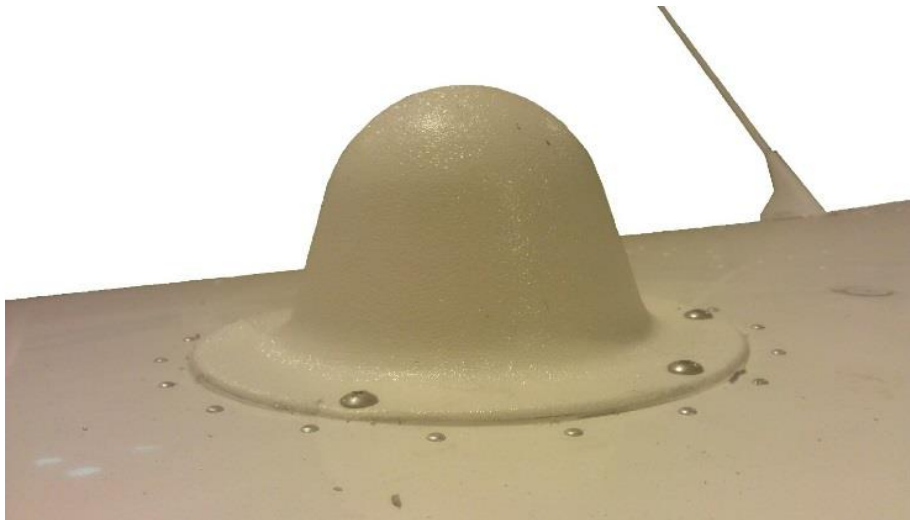


Figure 29: Pasternack PE51057 transmit antenna. Shown here mounted on the roof of the Cessna 172

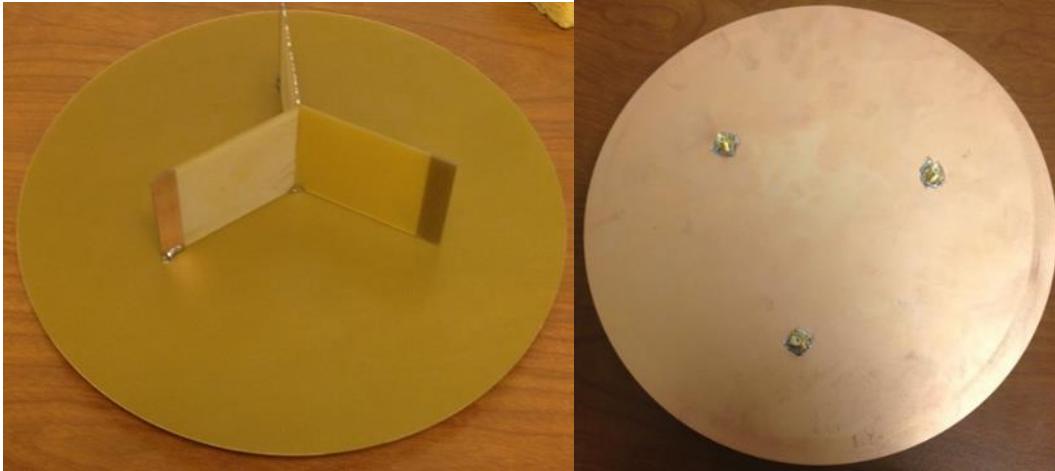


Figure 30: Azimuth RX antenna array.
 (left) Three, quarter-wave monopole antenna array. (right) SMA feed connectors and ground plane [ref 8].

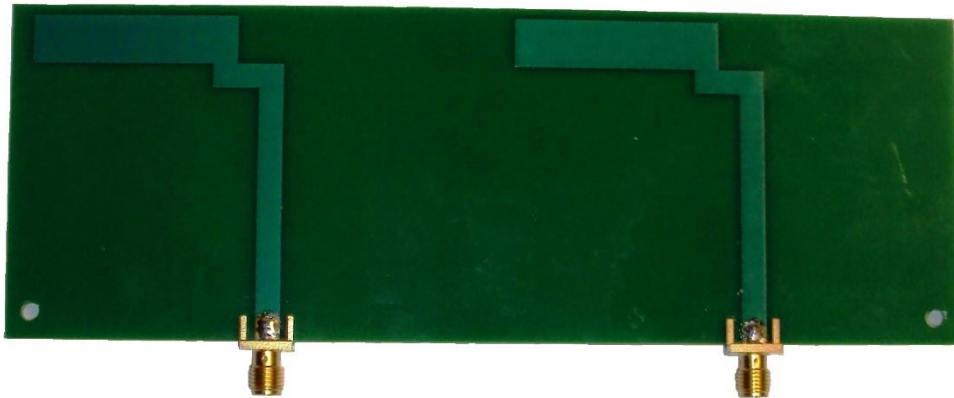


Figure 31: Elevation RX antenna array.
 Two electrically small dipole antennas separated by 8.85 cm [ref 9].

3.2 Radar processing in hardware

The following is a walkthrough of FPGA architecture and post processing necessary to generate a complete 2-D FFT image using the brassboard radar system and user computer.

Figure 32 illustrates this process as a block diagram.

During a single PRI of the FMCW radar, the ADC performs interleaved sampling of the five RX channels at 4 MSa/s per channel resulting in a data rate of 20 MSa/s (12-bit parallel output per sample). The data is read into the FPGA where it is multiplied by a Hanning window

stored in a lookup table. The multiplication of the 12-bit ADC data with the Hanning window scaler resulting in a 16-bit wide data output. This data point is then stored in one of five buffers within the FPGA based on which ADC channel the sample originated from. Once 800 samples per RX channel had been collected from a single radar PRI (takes 200 μ s) each buffer is zero padded to 1024 points and sent into parallel FFT engines created by Xilinx's ISE CORE Generator. The data from the buffers are fed into the FFT engines as the real values while the imaginary values are set to zero. The output of each FFT engine is a 1024-point complex data vector that is 54-bits wide, 27 bits per real value and 27 bits per imaginary value.

From a timing perspective, performing the Hanning windowing and parsing the data stream into buffers happens in real-time with only a 4 or 5 clock cycle latency (100-MHz clock). Performing the FFT of a 1024-point data set takes 34 μ s and the process is performed in parallel across all RX channels. This means that the fast-time dimension FFTs can be performed by the FPGA in real-time.

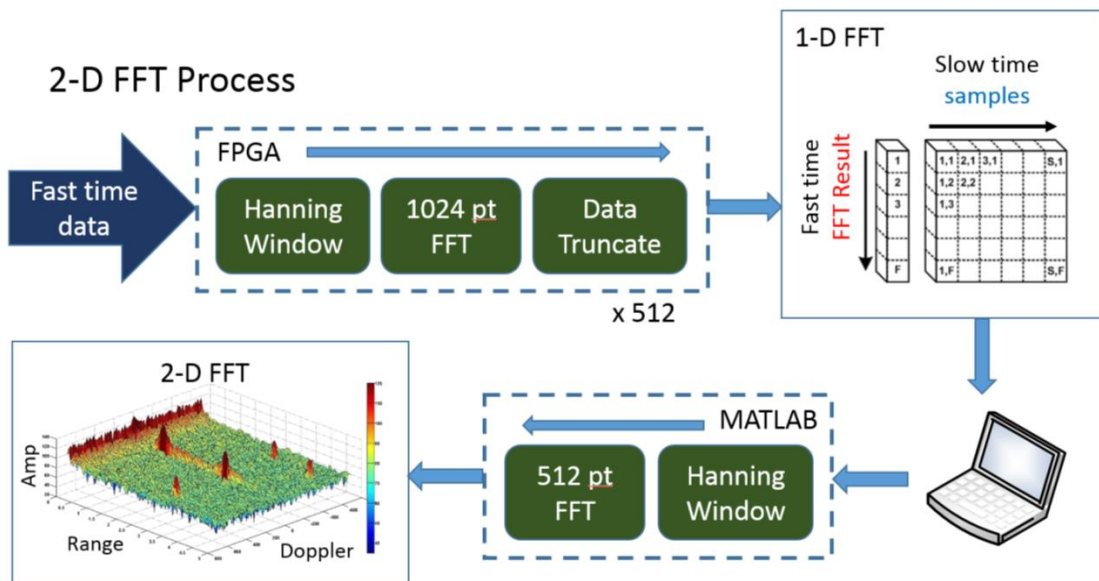


Figure 32: Block diagram of the 2-D FFT process. The FPGA generates the fast-time FFTs in real time and MATLAB is used to perform the slow-time FFTs in post processing.

From a data management perspective, out of the 1024-point complex FFT output per RX channel, only the first 128 complex points are kept which represents frequencies from 0 Hz – 500 kHz (i.e. target ranges from 0 m – 1 km). Out of the 54 bits per complex data point, the LSB 16 bits of both the real and imaginary components are stored while the rest are discarded. This entire process became known as the FFT truncation process which reduced each fast-time FFT data vector from 55,296 bits (1024 points, 54-bit wide) to 4096 bits (128 points, 32-bit wide), a 92.6% data reduction. A total of 512 truncated fast-time FFT data vectors needed to be gathered and placed side by side to fill a single data matrix before the second series of FFTs across the slow-time dimension can be performed (figure 32, top right). This means that a ping-pong architecture is required to avoid losing data from the next radar image while the current radar image completes the 2-D FFT processing. Multiplying this across five RX channels resulting in 2.6 MB of memory space required. However, due to a lack of documentation, the off-board RAM on the Ztec FPGA evaluation board could not be accessed and the internal block RAM of the FPGA was only capable of storing about 550 kB. Thus a decision was made to cut down the number of radar receive channels to only two and to only perform 1-D FFT processing on the FPGA removing the need for a ping-pong architecture. The slow time dimension FFT would be performed in post processing on the user computer. This process reduced the memory requirement down to 524 kB which uses up over 90% of the FPGA's onboard block RAM.

The data transfer speed from the FPGA to the user computer over USB was a second unexpected bottle neck which could only hit rates of approximately 1 MB/s. This effectively slowed down the 2-channel radar data record rate on the user computer to 1.7 Hz (each update takes 0.59 ms to write to PC). Once the data was written to hard drive, a MATLAB script was created which reads the 1-D FFT data, perform Hanning windowing across the slow-time

dimension and complete the FFTs resulting in a fully 2-D FFT processed radar image. This is why the brassboard radar parameters listed in table 5 falls short of the initial design parameters in table 1. Though these limitations are severe, it was enough to demonstrate the FPGA's data processing capabilities (Hanning windowing and FFTs) and, after post processing, resulted in a 2-D FFT radar image for demonstrating the proof-of-concept. Section 3.3 will discuss the 2-D FFT results in detail and the testing of this brassboard radar in a laboratory environment.

3.3 Loopback testing

Individually each component of the brassboard radar was tested using some combination of spectrum analyzers, network analyzers, logic analyzers, and/or a high-speed oscilloscope. Once the radar was assembled on the brassboard, a radar loopback test setup was created to characterize the radar performance in a laboratory environment. Figure 33 shows a block diagram of the radar system and how it attaches to the loopback test setup inside the dotted box.

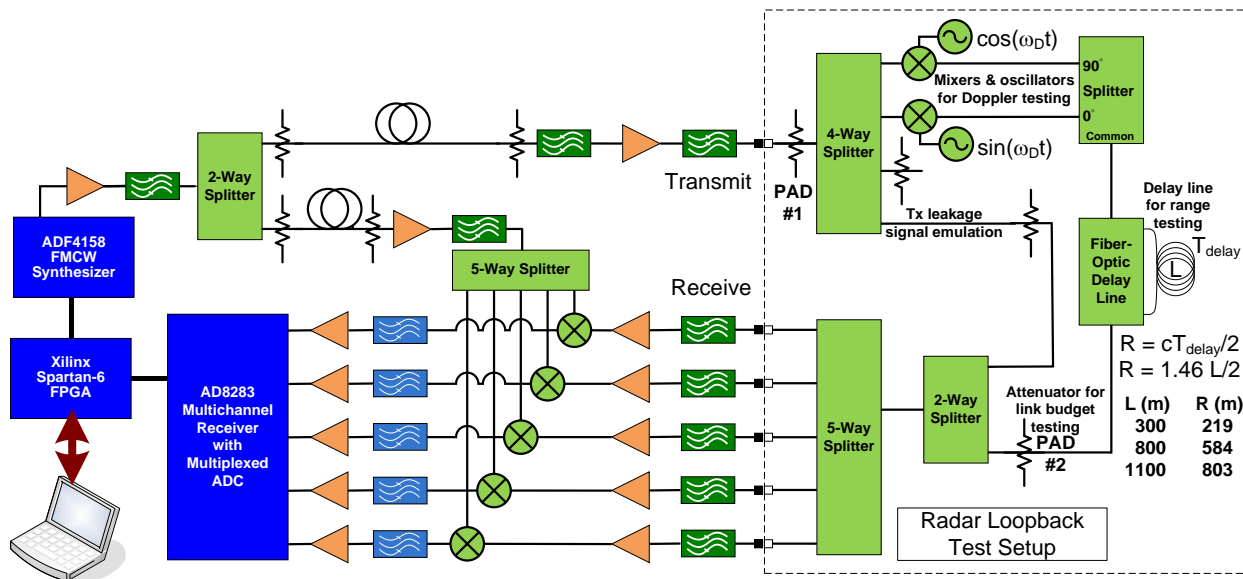


Figure 33: Block diagram of the radar system attached to the loopback test setup shown in the dotted box.

The loopback test setup's primary purpose is to mimic a distant point target by delaying the radar's transmit signal using a long fiber-optic spool and attenuating it to emulate the expected propagation loss. This loopback setup was also designed to apply a single-sideband Doppler shift to the transmitted signal. This is performed by using two synchronized function generators to produce an in-phase and quadrature version of the Doppler frequency which are used to modulate radar transmit signal. The modulated signals are then combined using a 90° splitter causing one of the sidebands to cancel. Note that the radar signal is used as the carrier in this modulation and will also show up in the 2-D FFT processed image.

Lastly, the loopback test setup incorporates the leakage signal by including a cable that bypasses the fiber-optic delay line and contains far less attenuation. This leakage signal is combined with the delayed, Doppler modulated, transmit signal and fed back into the receiver

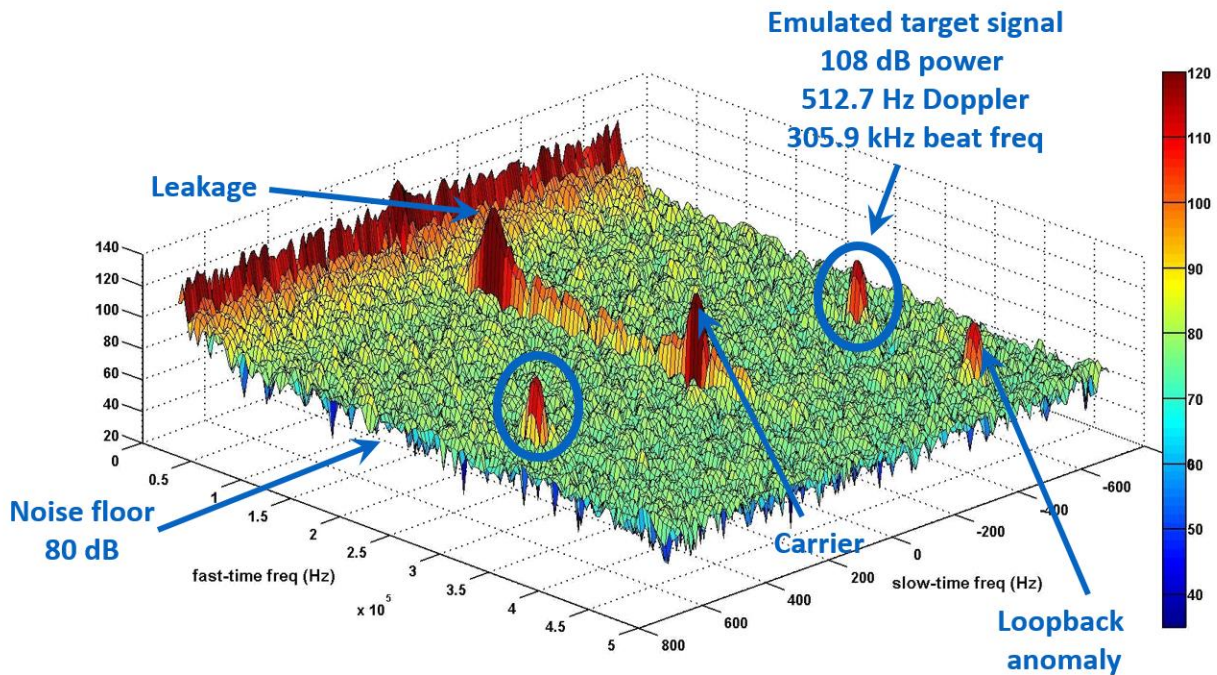


Figure 34: Brassboard radar loopback test result after 2-D FFT processing. A double sideband Doppler shift is used for this test hence there are two emulated targets circled.

Table 6: Radar loopback parameters for figure 33

Parameter	Value
Chirp bandwidth	15.7 MHz
Chirp duration	200 μ s
TX signal power	+25 dBm
RX signal power	-112 dBm
Leakage signal power	-12 dBm
Doppler modulation	500 Hz (double sideband)
Delay line length	800 m

channels. An 800-m long fiber-optic cable is used in the loopback test setup. The signal propagation speed inside the fiber is slower than propagation through free space making the effective length of the fiber-optic spool seem longer by 1.46 multiplier. Keep in mind though that the fiber-optic is providing round trip delay thus the emulated physical range to the target is 584 m (i.e. 800 m x 1.46 x 0.5). Figure 34 shows an image of a completed 2-D FFT processed radar image using double-sideband Doppler modulation and -12 dBm of leakage signal. Table 6 contains the key parameters used during this loopback test.

3.3.1 Data Interpretation

Notice that figure 34 contains two targets which are the results of using a double-sideband Doppler modulation. This modulation was created by using a single function generator and mixer instead of the in-phase and quadrature method (one of the inputs of the 90° combiner terminated). This modulation results in two targets that appear at \pm Doppler frequencies which are symmetric about the zero Doppler axis.

The emulated target echo signal strength going into the radar RX chain was assumed to be -112 dBm through calculating the total attenuation in the loopback setup. After the 2-D FFT processing this resulted in a pulse compressed target peak with a 28-dB SNR. Assuming that a minimum 10-dB SNR is required for target detection, then the minimum detectable input signal

strength is -130 dBm. Using the radar range equation [1], duplicated below, and assuming a 1 m² RCS, the maximum detection range, R, can be solved for.

$$P_{RX} = \frac{P_{TX} G^2 \lambda^2 \sigma L}{(4\pi)^3 R^4} \quad [1]$$

Assumptions:

$$P_{RX} = -130 \text{ dBm}$$

$$P_{TX} = 25 \text{ dBm}$$

$$G = 0 \text{ dBi}$$

$$\lambda = 20.7 \text{ cm}$$

$$\sigma = 1 \text{ m}^2$$

$$L = 0 \text{ dB}$$

$$\mathbf{R_{max} = 511 \text{ m}}$$

This means that with the given radar performance demonstrated in the loopback test and assuming no extra losses, the maximum detection range of the radar system is 511 m for a 1 m² RCS target.

The location of the targets in range (fast-time) can be verified as well given the loopback test setup emulated range of 584 m. The radar's bandwidth, B, is 15.7 MHz and the sampled transmit duration, τ , is 200 μ s. Therefore the expected target beat frequency, f_B , is 305.6 kHz and is given by equation 4 below.

$$f_B = \frac{2RB}{c\tau} \quad [4]$$

In the fast-time dimensions, the expected target beat frequency is 305.6 kHz which matches closely to the measured beat frequency of 305.9 kHz in figure 34. The Doppler frequency is set by the function generator used in the Doppler modulation which was set to 500 Hz. The function generator was running asynchronously to the radar system which measured Doppler shift to be 512 Hz. After multiple trials at various Doppler frequencies it can be

concluded that the 12-Hz difference between the radar measurement and the function generator is a bias that can be calibrated out.

3.3.3 Anomalies and saturation

The other notable signals in figure 34 are the carrier, and the anomaly. The carrier, is the original TX radar signal used in the Doppler modulating. This signal compresses to zero Doppler and a fast-time frequency equal to that of the targets since it too underwent the delay through fiber-optic cable. In the actual operation of the radar onboard the aircraft however, this signal will not exist.

An anomaly appears in the 2-D FFT processed image located at roughly 450 kHz fast-time frequency and -450 Hz Doppler frequency which could be mistaken as another target. The exact cause of this feature is unknown but is speculated to be a reflection of some sort or coupled interference. Throughout the various loopback tests performed on the brassboard radar there are cases where random signals such as the one shown in figure 34 appear. Furthermore, these anomalies have been observed to migrate slowly in Doppler from radar update to update but never in range. Since these anomalies do not follow a physical range-Doppler relationship (e.g. if the Doppler indicates an approaching then the range to the target should decrease on consecutive images) then they should be able to be filtered out without causing false alarms.

The loopback test setup was also used to investigate the effects of leakage saturation. Using Xilinx's Chipscope analyzer capability, the ADC output received by the FPGA can be monitored and plotted. Figure 35 shows the Chipscope plot of the ADC data when the input into the RX chain the expected maximum leakage signal (-12 dBm) along with the emulated target echo from the loopback test setup. This test allowed the RX chain to be calibrated such that

leakage signal. Should the clipping effects of figure 36 be seen however, a simple recompile of the FPGA code to use more significant bits should easily resolve the issue.

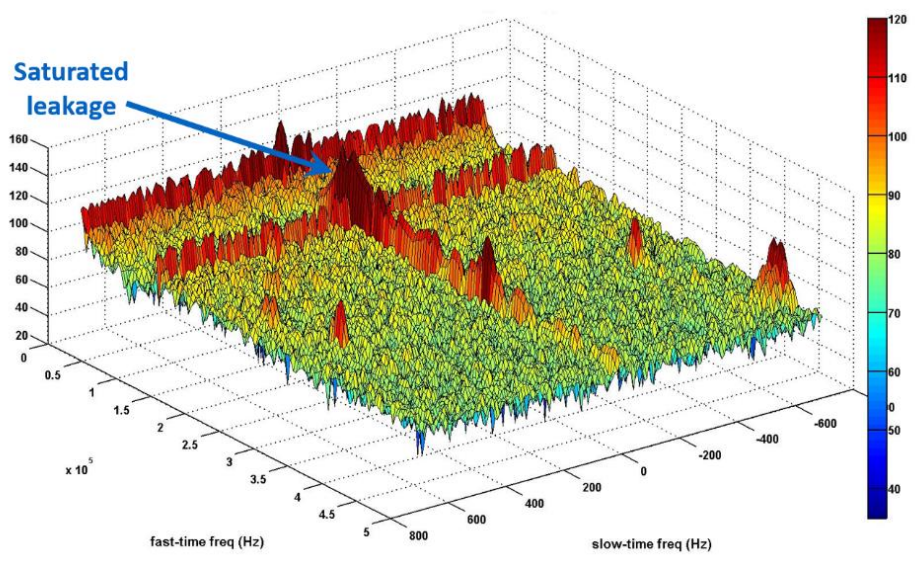


Figure 36: Example of a 2-D FFT processed radar image where the leakage signal is clipped by selecting the LSB 16-bit output from the FPGA's FFT processing.

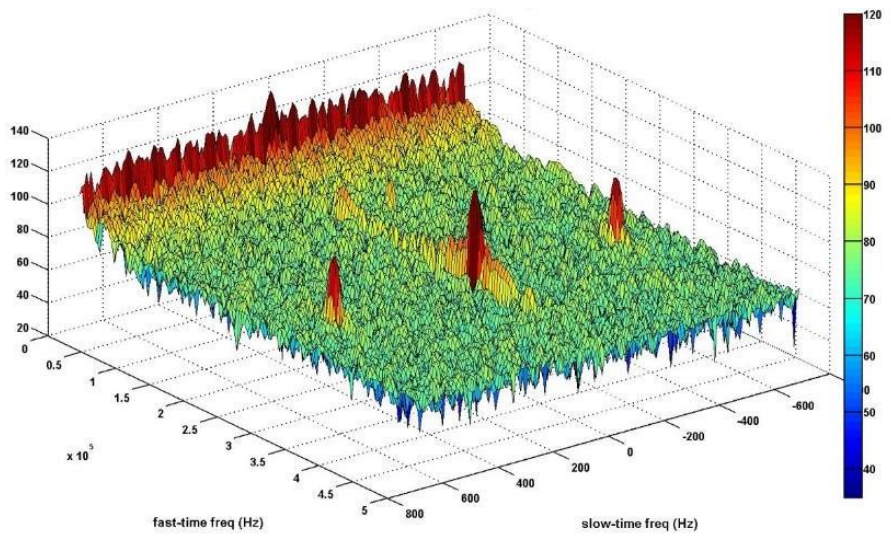


Figure 37: The same setup and processing as figure 36 but without the leakage signal. A comparison of the two figures shows that the saturated leakage signal will significantly affect the entire noise floor and thus SNR.

3.4 Flight testing

Flight testing of the brassboard radar system was conducted on February 22, 2014 onboard KU Aerospace Engineering (AE) department's Cessna 172 shown in figure 7. The brassboard radar was vertically mounted in the back of the cabin using metal cables bolted to the aircraft frame. Both the azimuth and elevation RX antenna arrays were mounted inside the cockpit behind the windshield using a wooden fixture. This installation setup was decided upon for the ease of flight certification. The TX antenna, since it already came in an aerodynamic form factor, was mounted to the roof of the aircraft without producing any flight worthiness concerns. The TX and RX antenna placement provided the conditions for the expected -37 dB of leakage signal coupling which was verified using a portable network analyzer to perform a S21 measurement. It should be noted that there was an unexpected amount of cable routing through the Cessna resulting in using 15-ft long SMA cables to connect the brassboard radar to the TX and RX antennas. This this cable length is estimated to have added an extra 9 dB of TX power loss and RX attenuation that was unplanned and untested using the loopback setup. Figure 38 is a set of images of what the final installation looked like about the Cessna.

The target that the radar was flown against is a 1045-ft tall tower located near Linwood, KS. During a test approach, the pilot would aim the Cessna's trajectory towards the tower at roughly 1-mile out and match the aircraft height AGL with the height of the tower. At this point the radar would be turned on and continuously capture 1-D FFT data from the two elevation antennas at a rate of 2 Hz. Note that no azimuth antenna were used during the test due to limitation described in section 3.2. The aircraft ground speed was maintained at approximately 93 knots during the entire approach and fly by. The flight test location and setup is illustrated in figure 39.



Figure 38: Brassboard radar system installation onboard the Cessna 172. (left) Brassboard radar system mounted vertically in the back of the Cessna 172 just behind the rear seat. (top right) RX azimuth and elevation antennas mounted inside the aircraft. (bottom right) TX antenna mounted to the roof.

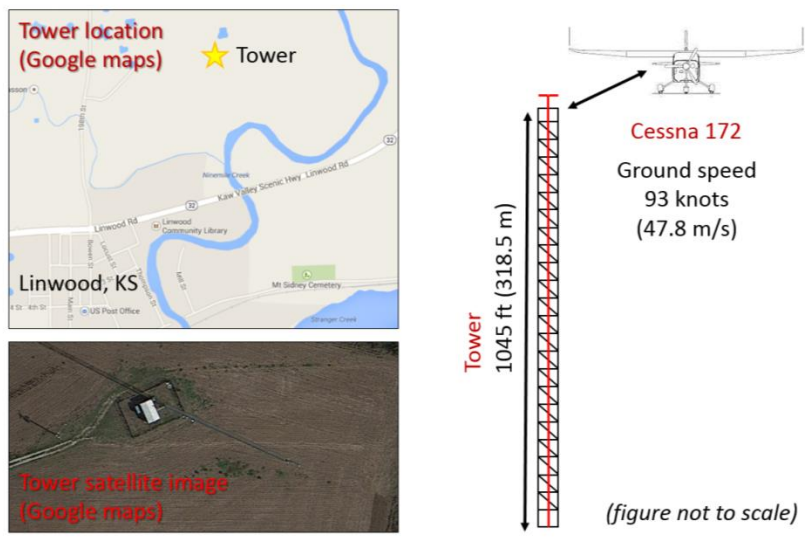


Figure 39: Brassboard radar test flight setup against tall tower near Linwood, KS.

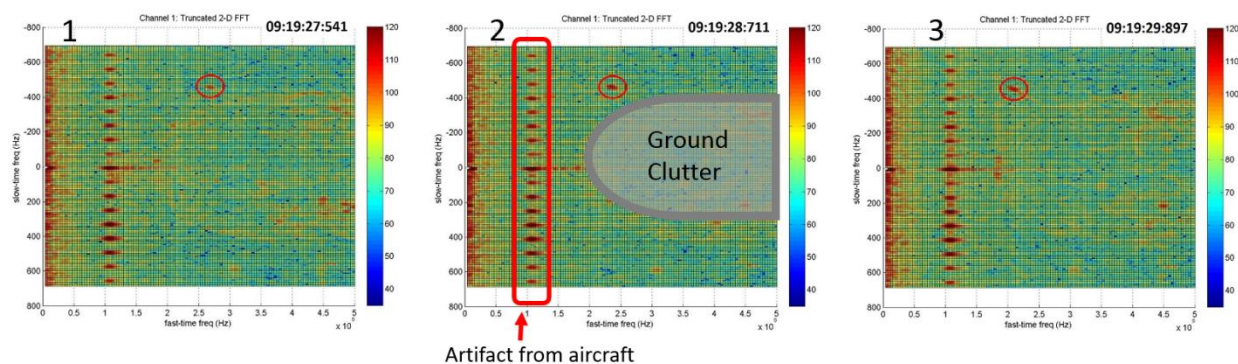


Figure 40: Sample of brassboard radar flight test results. Samples are selected at 1-second intervals showing successful target detection of tower (circled in red).

The brassboard radar flight test was successful in detecting the target tower. Figure 40 shows three sample images where the detected approaching tower is circled in red. The X-axis of the images are fast-time frequencies of 0 Hz to 500 kHz from left to right (i.e. ranges from 0 m to 1 km). The Y-axis of the images are slow-time (Doppler) frequencies of -700 Hz to +700 Hz from top to bottom (i.e. radial velocities of +72.7 m/s to -72.7 m/s or ± 141 knots). For all of the 2-D FFT processed images in this document, negative Doppler translates to positive radial velocities which indicates an approaching target while positive Doppler translates to negative radial velocities which indicates a retreating target (see equation 5). Therefore, the target tower in figure 40 can be seen as an approaching obstacle at a constant velocity and its range from image to image is steadily decreasing.

The middle image of figure 40 highlights two critical features beyond just the target tower. First is the ground clutter which spans both positive and negative Doppler and a range of approximately 400 m to 1 km (200 kHz to 500 kHz). This is expected from the simulations performed in section 2.4 of the ground echo returns. The closest point of the ground clutter at 400 m (1300 ft) is effectively the aircraft height AGL which is confirmed by the flight geometry where the pilot attempted to align the aircraft with the tip of the tower. Furthermore, the ground

clutter's Doppler values spans up to ± 400 Hz which equates to ± 80 knots ground speed. This is fairly close to the 93-knots ground speed recorded off of the flight instrumentation. The fact that the radar's measurement is less than the true value is expected since the distant ground echoes moving at faster speeds (closer to 93 knots) are likely masked by the noise due to the incident angle dependency of the backscatter coefficient. The second feature is the appearance of artifacts at the 100-kHz fast-time bins. This is not the same as the FFT truncation saturation shown in figure 36. The origin of these anomalies are unknown but are believed to be caused by the aircraft either through couple interference or reflections/multipath off of the aircraft propeller.

Figure 41 is an enhanced view of a single 2-D FFT processed radar image from the flight test against the tower. Using equation [4] the fast-time frequency of the target tower (i.e. f_B) can be converted to range, R , which locates the tower at a range of 473.9 m during this radar image. Using equation [6] below, the slow-time (Doppler) frequency, f_D , of the target can be converted to radial velocity, V_r , by:

$$f_D = \frac{-2V_r}{\lambda} \quad [6]$$

where λ is the wavelength of the chirp signal (0.2076 m). Given that the measured f_D is -465.8 Hz, the radial velocity of the tower is calculated to be 72.7 m/s or 94.1 knots. Since the aircraft is flying straight towards the tower during the flight tests, this radial velocity is effectively the

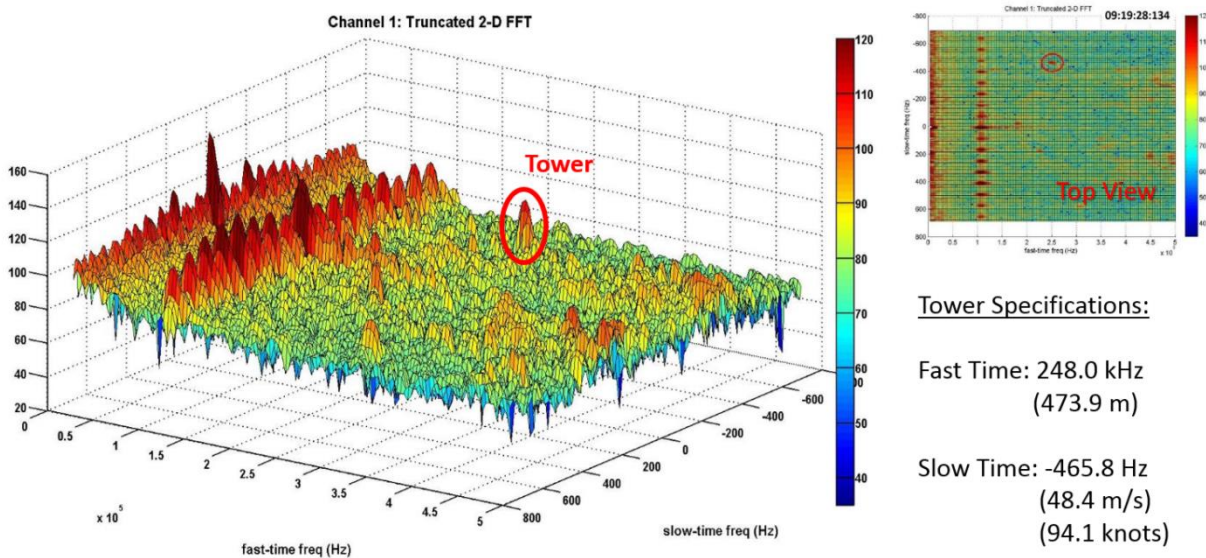


Figure 41: Enlarged view of brassboard radar 2-D FFT processed flight test image.

aircraft ground speed which was confirmed to be 93 knots by the Cessna's onboard instrumentation.

A total of 27 radar images containing the tower echo were captured during the flight test at roughly 2-Hz update rate. Using equations [4] and [6] across all of these images, the target tower's range and radial velocity as a function of time can be determined (figure 42 and 43).

Using the range and Doppler information from a single radar image, it is possible to predict the range to the target on the next radar update. A comparison of the prediction range against the actual measured range is shown in figure 40. This process of verifying the range-Doppler relationship and a potential method of removing anomalies such as the unknown peaks around the 100-kHz fast-time mark. Figure 44 shows that on average there is about an 11 m error between the measured and predicted range to the target. Note that this is approximately one range resolution bin which is 10 m.

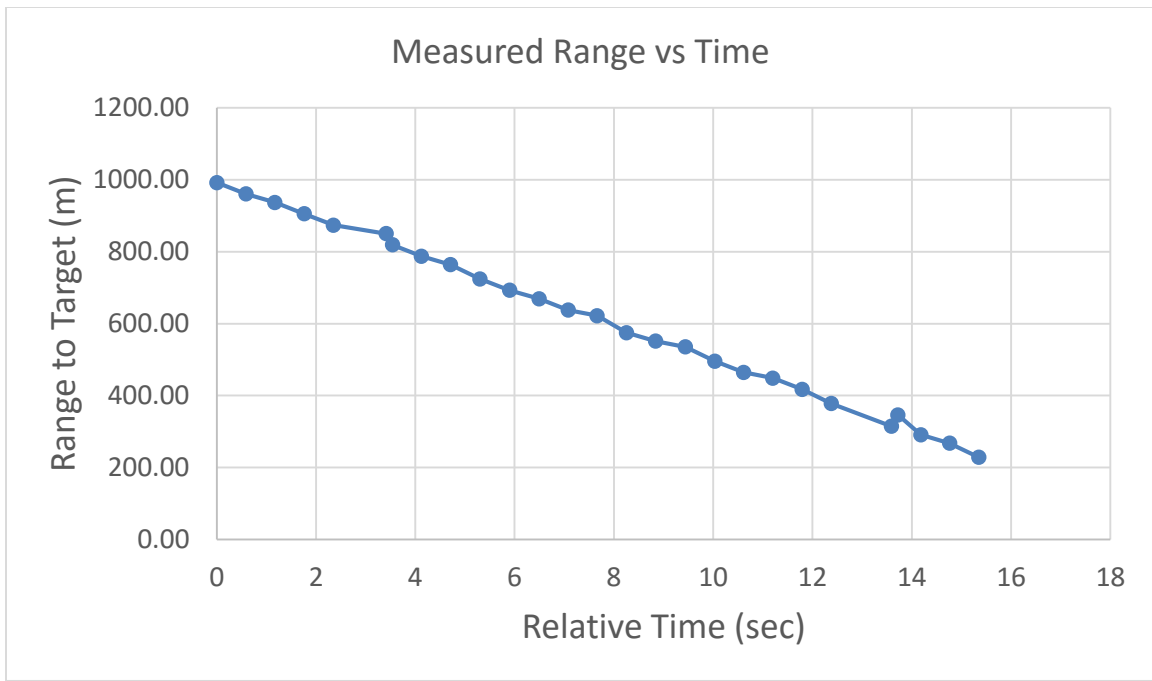


Figure 42: Measured range to target tower from consecutive radar updates during an approaching flight test.

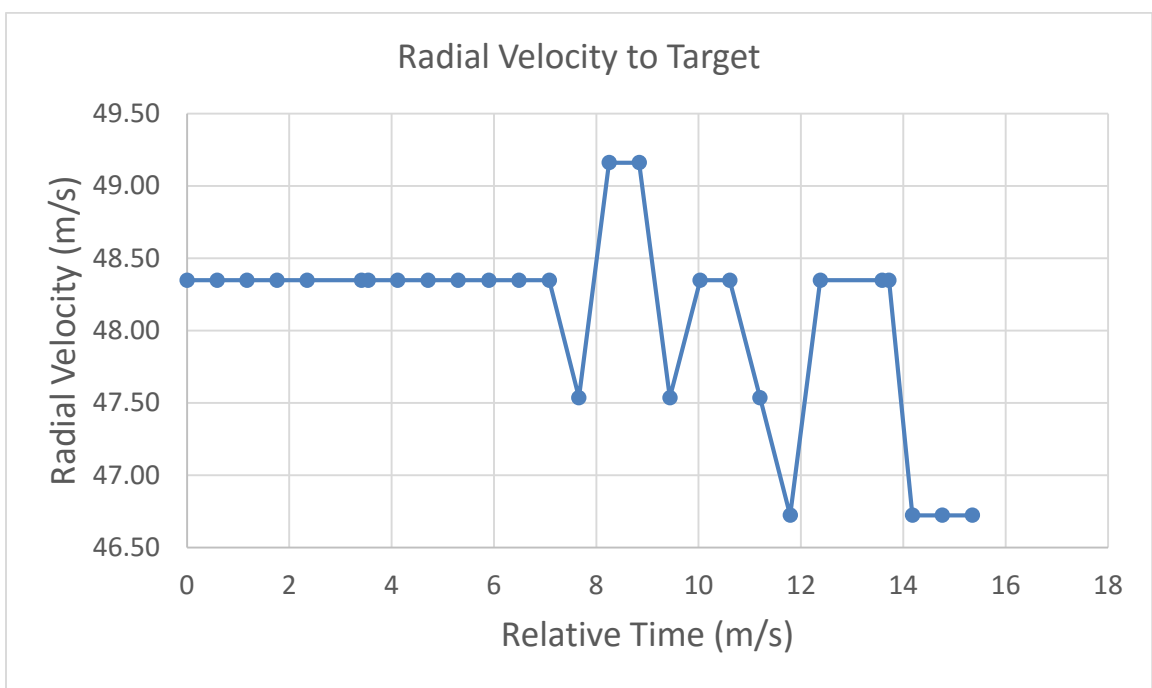


Figure 43: Measured radial velocity (i.e. aircraft ground speed) from the same consecutive updates in figure 42.

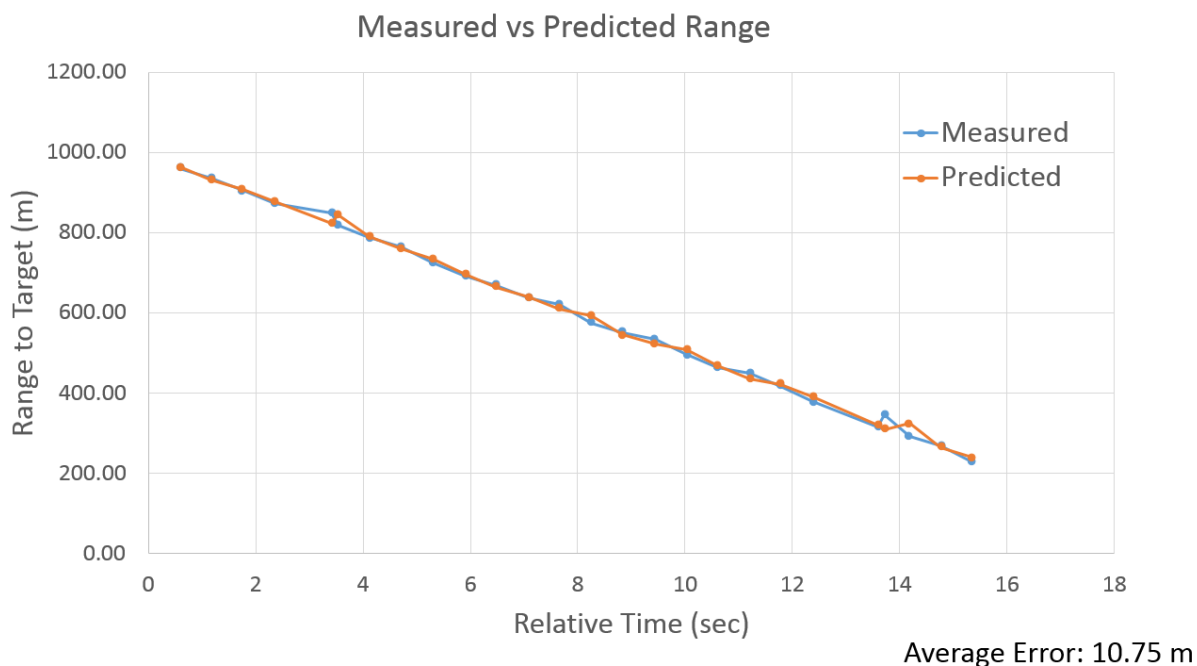


Figure 44: Measured ranges to target tower vs. predicted ranges to target tower based on previous measurements of range and radial velocity.

Looking back at figure 40, as the aircraft flew closer to the tower, the tower's echoes became stronger. At a range of approximately 250 m (125 kHz fast-time), right before the tower was about to enter the anomaly region, the individual scattering points on the tower became visible. Since the two elevation antennas of the RX array were used, the elevation angle of these scatterers were calculated. Figure 45 shows an enlarged image of the tower scatterers as well as the elevation AoA of these points. Note that since a calibration of the radar AoA was not performed and therefore biases in the data is likely to exist. An assumption was made that 0° elevation is aligned parallel to the ground and that the aircraft was flying straight and steady with the elevation antenna array's boresight aimed parallel to the ground. Given these assumptions it can be interpreted that these individual scatterers are located on roughly the same vertical axis (i.e. the tower) but at different elevations based on their range. This is a sample of the process

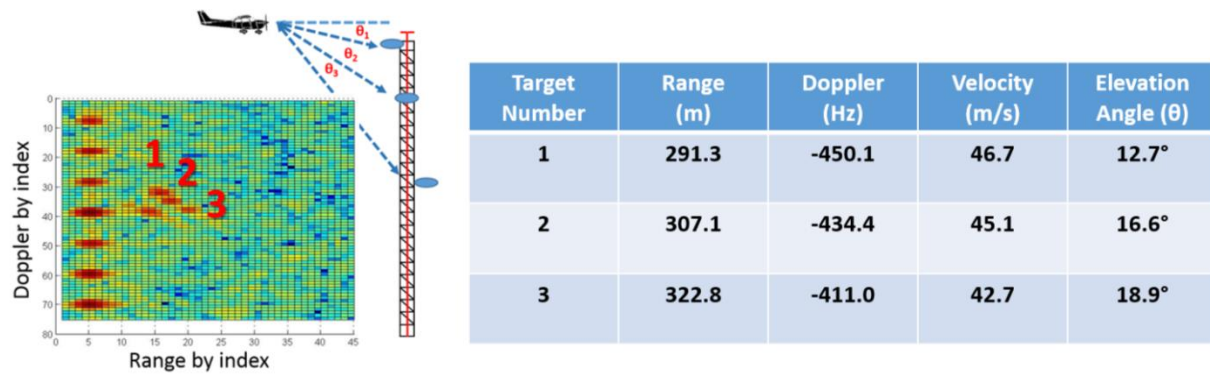


Figure 45: One instance of range, Doppler and calculated AoA obtained from brassboard radar flight test data.

that will be used to determine the target location through interferometry once more than 2 RX channels are available.

Chapter 4: Miniature radar

Work on the miniaturizing the brassboard radar system began in January 2014 to demonstrate the feasibility of creating a radar with small SWaP that could fit onboard the 40% Yak-54 UAS. The resulting miniature radar has the following parameters listed in table 7. The primary difference between the miniature and brassboard radar systems are the center frequency, the transmit power, and the ability to receive from 4 RX antenna elements as interleaved pairs vs the static 2 antenna receiver on the brassboard system. The center frequency migration to 2.365 GHz had a significant impact on all of the components used in the miniature radar as well as the radar detection range. This change was made in order to support the use of COTS antennas and to take advantage of the number of ICs that are available near the 2.4-GHz frequency range. The initial rev1 miniature radar system seemed to have produced acceptable laboratory test results but failing during flight testing. A series of diagnostic testing were then performed which uncovered some critical flaws in the system. A rev2 miniature radar system was finally created

Table 7: Rev1 and Rev2 miniature radar parameters

Parameter	Value
Radar type	FMCW
Center frequency	2.365 GHz
Bandwidth	15.7 MHz
Transmit duration	254 μ s (210 μ s chirp & 44 μ s delay)
Fast-time data capture duration	200 μ s
Slow-time samples	512
Update rate	2 Hz (1-D FFTs)
Transmit power	0.0724 W (18.6 dBm)
Sampling frequency	4 MSPS / channel
Range resolution	9.55 m
Doppler resolution	9.77 Hz (0.62 m/s)
Transmit antenna	Monopole (COTS)
Receive antenna	4 element array
Active receiver channels	4 channels interleaved as pairs

and laboratory tested with considerably better performance. The rev2 miniature radar was further tested on the roof of KU's engineering build against moving vehicles to demonstrate its capabilities.

4.1 Miniature radar hardware

The miniature radar hardware for both rev1 and rev2 can be broken down into three parts, the RF board, the digital board, and the antennas. Figure 46 shows a block diagram of the miniature radar components. A team of electrical engineering senior design (EECS 502) students volunteered to develop the RF board as a capstone project and was mentored through the process. Robert Young at IDL created the digital board, and both the TX and RX antennas were purchased as COTS components for the new center frequency. The design of both the RF

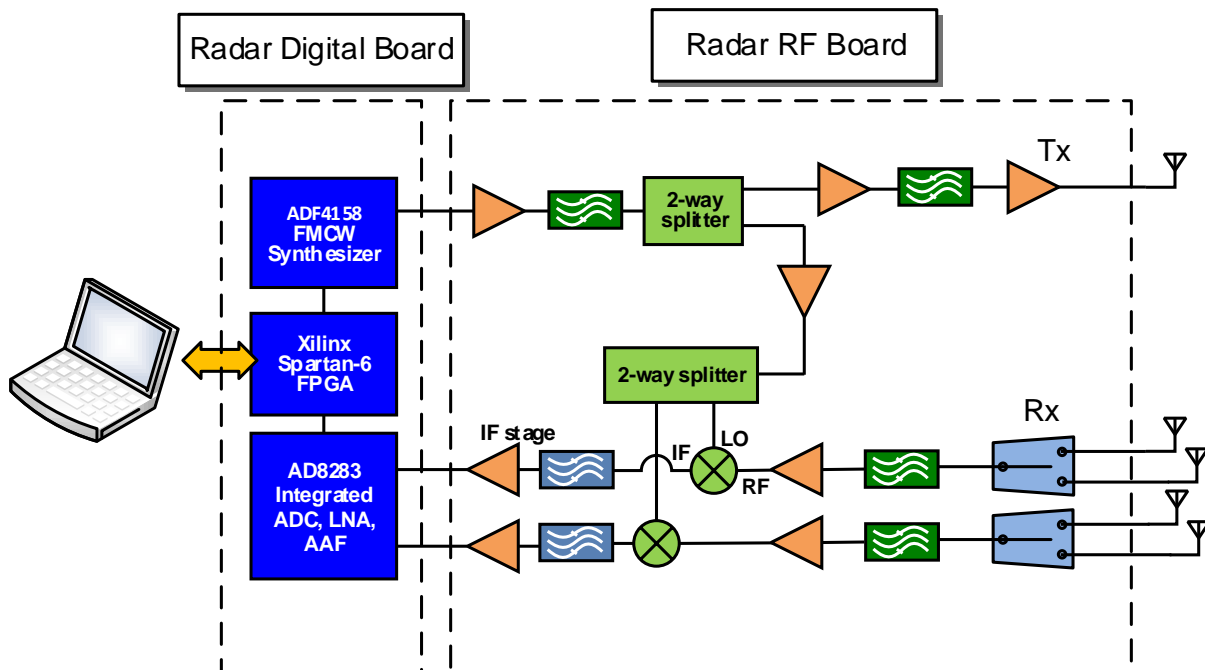


Figure 46: Miniature radar system block diagram.

The radar is miniaturized down to two PCBs with a FPGA daughter board. Note that the RX antenna array only uses 4 elements.

and digital boards needed to fit inside the recommended chassis specified by KU's AE department. The chassis is one that has previously flown onboard the 40% Yak-54 UAS and is shown in figure 47. It measures 6.63 in x 4.25 in x 2.31 in (L x W x H) and weighs 0.80 lbs. The following subsection describes each part in more detail.

4.1.1 Miniature RF board

The miniature radar's RF board is fairly consistent with the brassboard radar's RF assembly except for the addition of two RX switches. Since the same Ztex FPGA evaluation board is used for this radar system, the number of RX channels is still limited to just two inputs and therefore, in order to perform azimuth and elevation AoA measurements, the RX switches are used to toggle amongst antenna pairings to allow radar images from all azimuth and elevation antennas to eventually be collected for unambiguous AoA estimation. These switches are controlled by the FPGA and cycles through three sets of RX antenna pairings (two for azimuth, one for elevation). Toggling to the next antenna pair is performed at the completion of each 1-D FFT matrix data write to the user computer. Figure 48 shows the connection diagram between

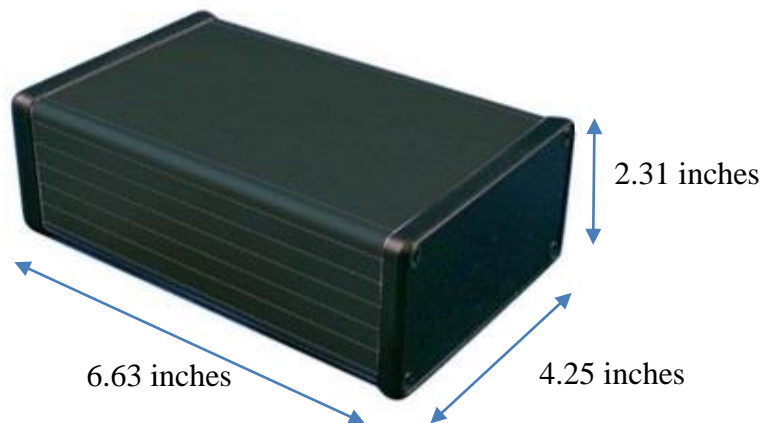


Figure 47: AE recommended chassis used to house the RF and digital PCBs of the miniature radar system.

the radar RF board and the TX and RX antennas and table 8 shows the antenna selection control produced by the FPGA and the associated RX antenna pair selected. Note that the new RX antenna array uses the same configuration as that depicted in figure 10 where one of the azimuth antenna elements (antenna B, top) is also used in the elevation array pair which reduces the necessary number of RX antennas to just four elements to provide unambiguous AoA estimations.

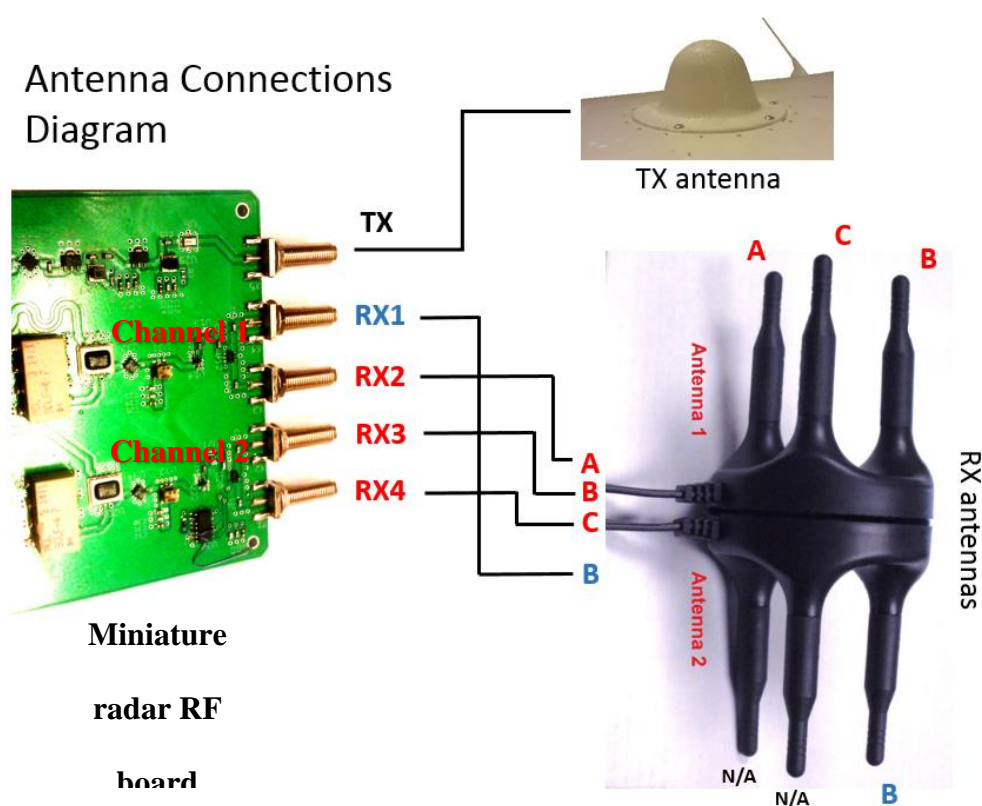


Figure 48: Miniature radar RF board to TX and RX antenna connection diagram. Data from the RX antenna array is collected in pairs. Table 8 shows the pairing selection.

Table 8: FPGA antenna selection control to RX antenna array mapping

Antenna Select (FPGA Ctrl)	RF Board Input	RX Antenna Array Pairing
0 (00)	RX2 & RX3	A & B
1 (01)	RX2 & RX4	A & C
2 (10)	RX1 & RX3	B & B

Before the miniature RF board was created, the individual surface mount components to be used in the TX and RX chains were tested using a custom evaluation board shown in figure 49. This board was created to test two potential amplifiers, a new SAW filter, a LPF, the RF switches, and a mixed substrate board stack up from a new vendor. One of the crucial findings from this evaluation board is that the grounding of the SAW filter in terms of number of vias, via size, and placement are critical to the SAW filter performance as seen in figure 50 which compares the measured evaluation board SAW filter against the typical performance taken from the datasheet. Extra care was taken in the miniature radar RF board layout around the SAW

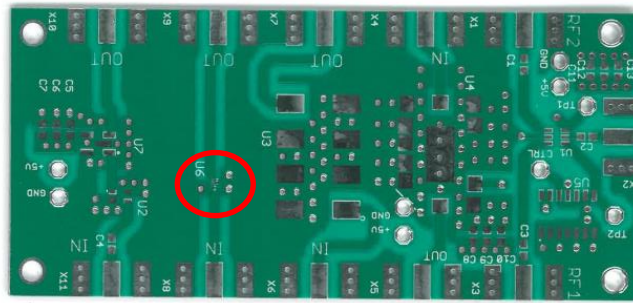


Figure 49: Miniature radar surface mount RF components evaluation board.

The components tested by this board are: amplifiers, SAW filter, LPF, and RF switch on a mixed substrate 4-layer PCB. All components performed as expected except for the SAW filter circled in red due to grounding mistakes.

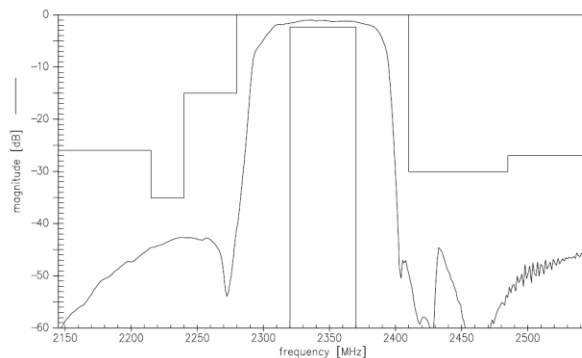
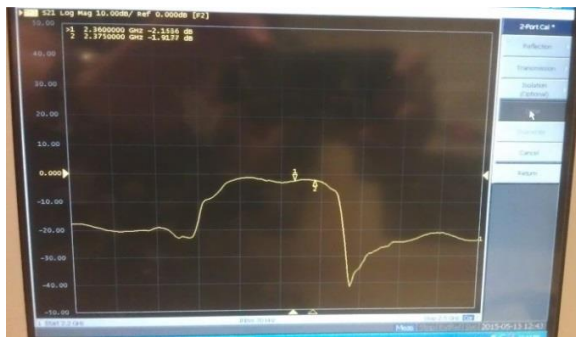


Figure 50: SAW filter performance on the custom evaluation board vs datasheet.

(left) SAW BPF response using improper grounding showing 20 dB rejection. (right) SAW BPF typical response per data sheet showing 40 dB rejection of out of band signals.

filters to match the datasheet recommendations. All of the other evaluated components functioned properly according to their typical performance.

The completed miniature radar RF board is a mixed substrate, 4-layer PCB manufactured by Custom Circuit Boards that measures 6.225 inches x 3.950 inches. The dielectric used between the 1st layer (RF signals) and 2nd layer (GND) is Rogers RO4350 while the other two substrate layers use FR-4 (note: the 3rd copper layer is power and 4th copper layer is low speed control signals). The RO4350 material has lower loss and better performance characteristics at 2.365 GHz compared to FR-4. Furthermore, a copy of the vendor's SAW filter evaluation board was eventually obtained and uses RO4350 dielectric.

Figure 51 shows an image of the populated miniature radar RF board. At the bottom of the board is the TX chain. The TX waveform enters the board through the SMB connector at the bottom right and is ultimately connected to the TX antenna through the SMA connector on the bottom left. In the middle of the TX chain, the signal is split and sent to the two mixers in the RX chain using matched length traces. The top 2/3 of the board are the two RX chains. Signals captured by the RX antenna array enter the RX chains through the top four SMA connectors on the left. Two of these inputs are selected using the RF switch and is ultimately converted into an IF beat frequency and sent to the digital board through the two SMB connectors on the right. These individual connectors and the TX and RX chains are shown with labels in figure 51.

SMB connectors are used between the digital and RF boards because they are snap on RF connectors. It is believed that this locking mechanism with its ability to provide a small amount of flexibility is better suited for the vibration environment onboard an aircraft. Since these connectors will be internal to the radar chassis, it would be inconvenient to have to resecure

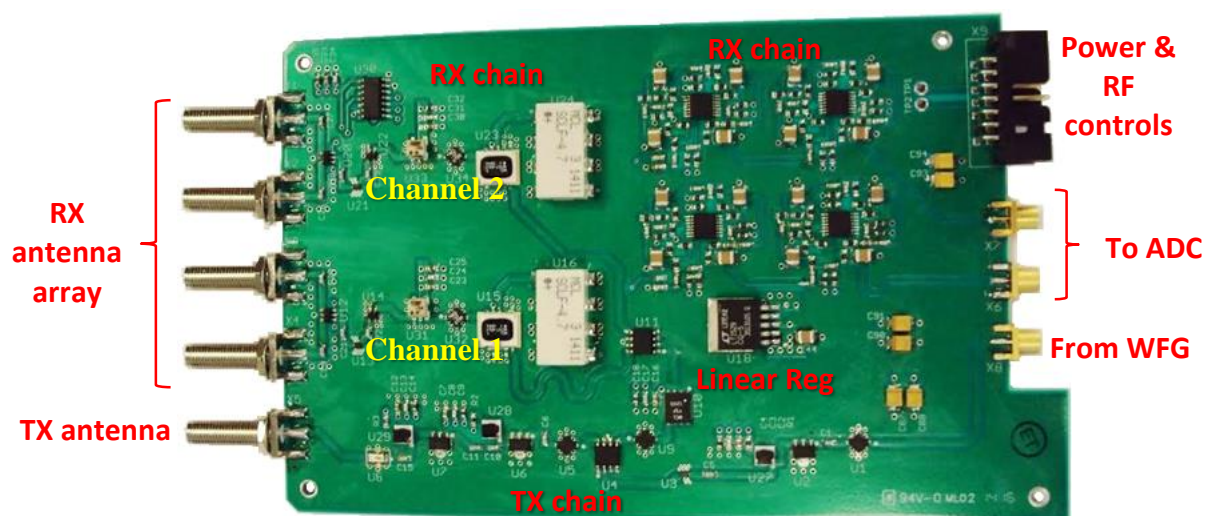


Figure 51: Miniature radar RF board.
The left hand side are SMA connectors to the TX and RX antennas. The right hand side are signals, power, and control lines to/from the digital board.

board designs where more than two RX channels will be used.

The black ribbon cable connector on the top right of figure 51 provides power and RF switch control signals to the RF board from the digital board. The components on the RF board that handles the 2.365-GHz signals (i.e. the TX chain and the first half of the RX chain prior to the mixer) are powered off of a 5V switching regulator (located on the digital board) provided through the ribbon cable. The IF portions of the RX chain, where the frequencies of interest range from 0 Hz to 500 kHz, are powered off of a 5V linear regulator labeled in figure 51, which steps the voltage down directly off of the 12V battery.

Figure 52 is a block diagram of the signal levels in the miniature radar RF board's TX chain and also includes the split signal sent to the RX chain mixers for IF down conversion. Note that even though the WFG is still the ADF4158, due to the migration to the new digital board the signal strength is now -12 dBm as opposed to the -9 dBm produced by the evaluation board. The primary bottle neck of the TX chain is the last amplifier in the chain (right before the

LPF and TX antenna) which has a P1dB of +22 dBm and an absolute maximum output of +24 dBm.

Figure 53 shows the block diagram of the miniature radar RX chain with labeled gains, attenuations, and expected leakage signal strengths at each point. Note however that the IF beat frequency of the leakage signal is heavily attenuated by the two cascaded Bessel, 8th order HPF

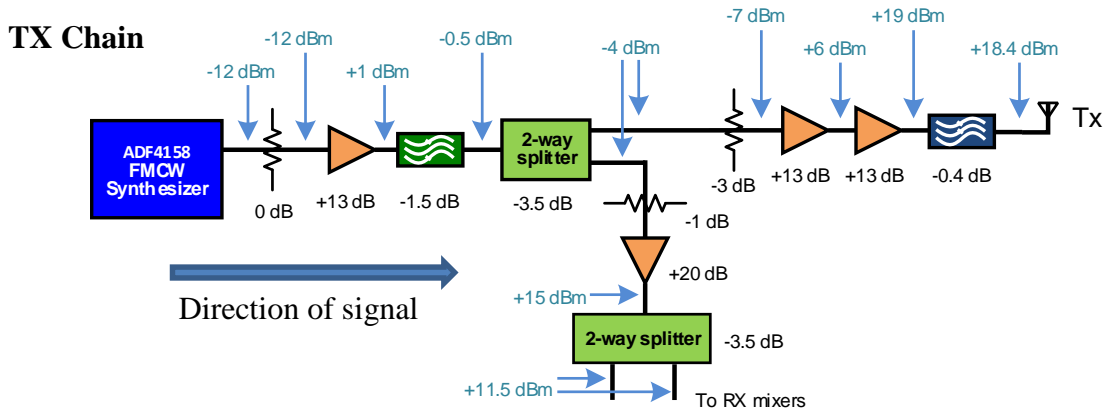


Figure 52: Miniature radar TX chain block diagram showing gain and attenuation (black) and signal strength (blue). Note the WFG built into the miniature radar’s digital board produces a -12 dBm output instead of the -9 dBm output from the WFG evaluation board used in the brassboard radar.

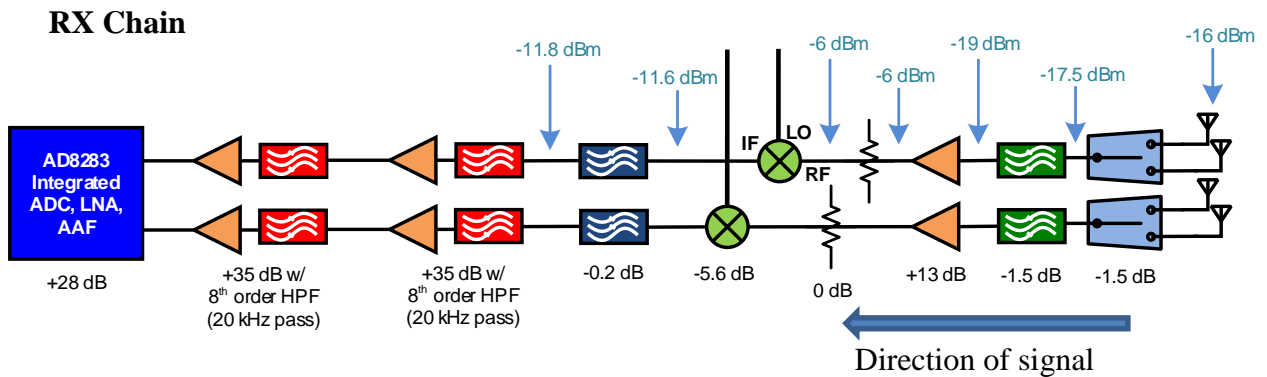


Figure 53: Miniature radar RX chain block diagram showing gain and attenuation (black) and signal strength (blue). The leakage signal is assumed to be -16 dBm. Due to the cascaded Bessel, 20-kHz, 8th order HPF, leakage signal strength could not be properly estimated beyond this point (Note: the leakage signal is near DC at the IF stage after the mixer).

and thus an estimation of the signal strength at this stage is not given since the exact leakage IF frequency is unknown. The Bessel HPF and amplifier are created from Texas Instruments' (TI) OPA322 operational amplifiers (op-amp) in a Sallen Key configuration. Figure 54 below shows one of the 8th order filters designed using TI's FilterPro software. Each op-amp IC contained four op-amps, which has a gain bandwidth product of 20 MHz and a slew rate of 10V/ μ s.

It was a concern that the 111 dB of total gain in the RX chain (13 dB in the RF stage, 70 dB in the IF stage, 28 dB onboard the ADC) would produce oscillations that could corrupt the radar results. However, since the RF, IF, and ADC amplifiers each used different voltage regulators, oscillations were not observed in the 2-D FFT processed radar images during laboratory testing.

4.1.2 Miniature digital board

The miniature radar's digital system combined the three previous digital evaluation boards into a single PCB along with all of the power regulators. The Ztex FPGA evaluation board (figure 57) was once again used instead of performing a custom FPGA layout to save time. The FPGA mates to the new miniature radar digital board through built in headers specifically designed to match the FPGA output without the need of the signal breakout board used in the brassboard radar. The schematic and layout of this board was performed by Robert Young at KU's IDL department. The board was populated and outputs were verified by Shi. Figure 55 shows the populated radar digital board without the FPGA evaluation board attached.

The same Analog Device's AD8283 6-channel ADC that was used on the brassboard radar is also used on the miniature digital board. Two of the ADC channels receive inputs from SMB connectors that connect to the two RX chains on the RF board. The other four ADC channels are setup as spare inputs located in the upper right corner of the board behind the ribbon

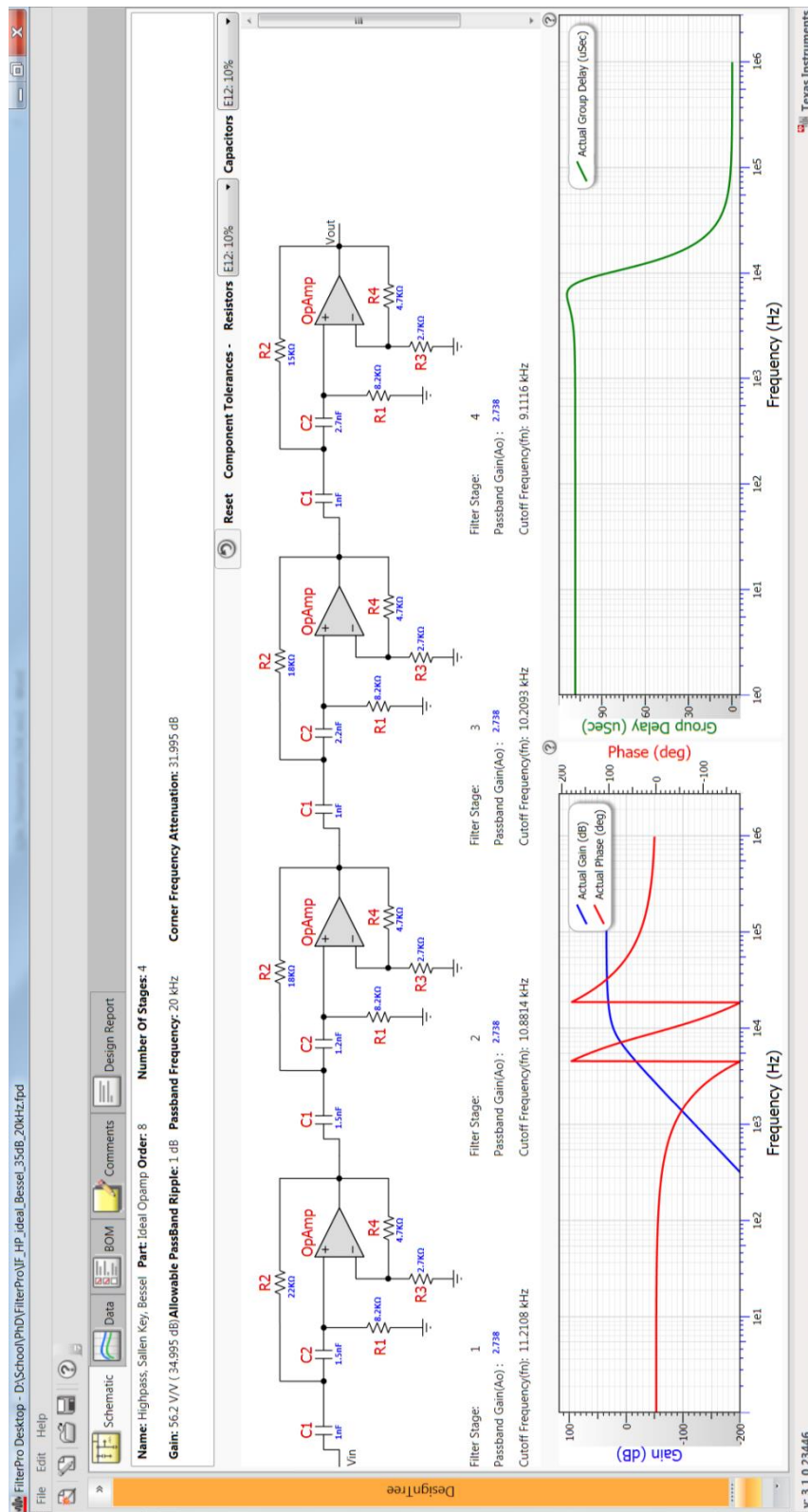


Figure 54: Miniature radar IF stage amplifier and HPF. The design is an 8th order Bessel HPF using a Sallen Key configuration. The HPF cutoff frequency is 20 kHz and the gain of the circuit is 35 dB.

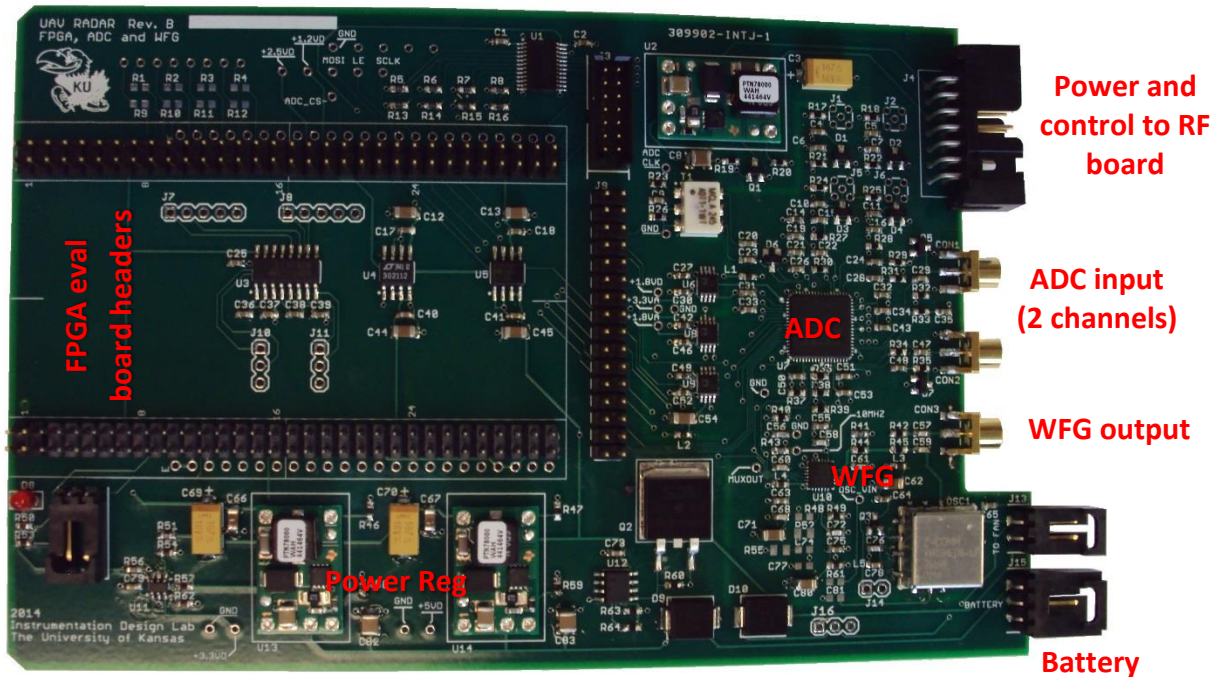


Figure 55: Miniature radar digital board combining the ADC, WFG, and power supplies onto a single PCB. The digital board also includes header banks which fits the miniature Ztex FPGA eval board shown in figure 57.

cable header.

The WFG is the same Analog Device's ADF4158 FMCW waveform synthesizer previously used in the brassboard radar. The output of the WFG is sent to the RF board via SMB connectors and shielded coaxial cable. This waveform generator's VCO is replaced with Z-Communications' V805ME08-LF IC which produces frequencies from 2.35 GHz to 2.93 GHz. The same VCO control programmed parameters were used in terms of a 210- μ s transmit duration, a hold time of 44 μ s between transmits, and a bandwidth of 15.7 MHz; but new tuning of the snubber filter circuit has to be done to smooth out the VCO voltage ramp. The before and after images of the voltage ramp is shown in figure 56 as well as the relative timing to the MUXOUT signal which synchronizes the FPGA with the PRF.

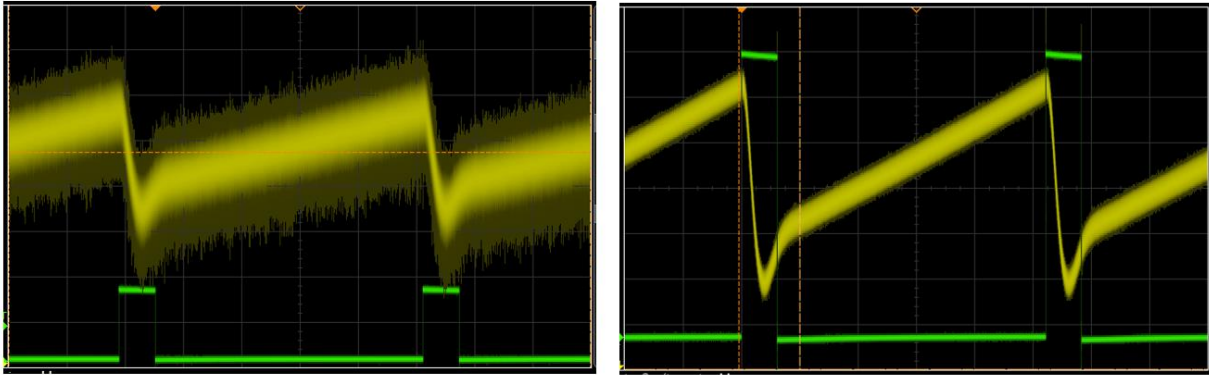
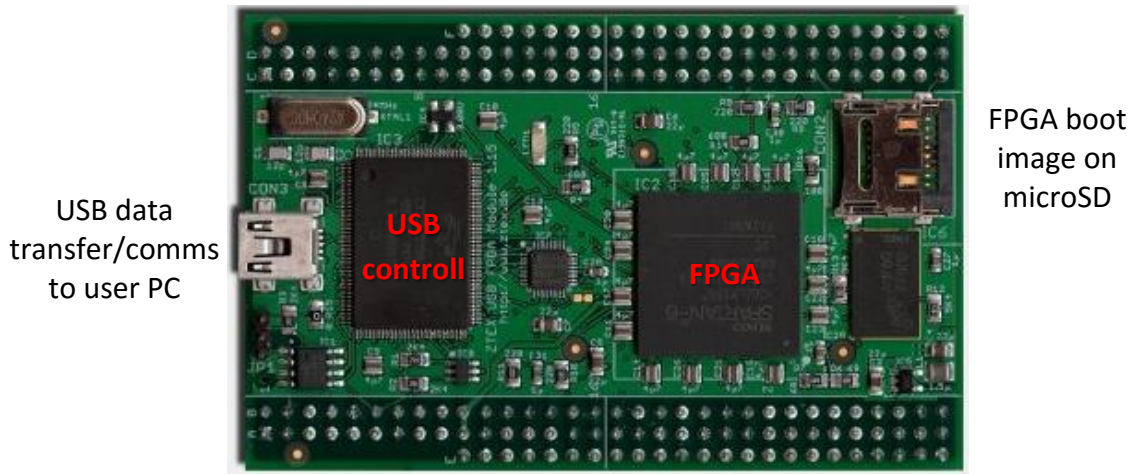


Figure 56: Tuning results of the WFG voltage ramp to the VCO on the new miniature radar digital board. (left) Noisy voltage ramp prior to tuning. (right) Quiet voltage ramp after snubber circuit tuning. Shown in green is the MUXOUT signal to trigger the FPGA.



USB data
transfer/comms
to user PC

FPGA boot
image on
microSD

Figure 57: FPGA evaluation board without heat sink or breakout board. This credit card sized eval board that mounts directly to the digital board shown in figure 55.

As mentioned before, the same Ztex Spartan-6 FPGA evaluation board was used again for the miniature radar system and mates directly to the new digital board. Testing was also performed with the FPGA heat sink removed and no thermal issues were found. An investigation into auto booting the FPGA from a microSD card was performed and demonstrated to be successful. However, given the constant revisions to the FPGA code, it was easier to manually reconfigure the FPGA during testing. The same FFT truncation and block RAM data

storage limitations described in the brassboard radar system still apply. Thus the miniature radar is still limited to producing two channels of 1-D FFT processed data at a 2-Hz update rate. The FPGA now produces a new set of control signals for the RF switches on the RF board allowing the two RX channels to select which RX antenna they are connected to. This capability allows enough data to ultimately be gathered for unambiguous AoA estimation. Figure 57 is an enlarged image of the FPGA evaluation board without the heat sink.

4.1.3 Antennas

The antennas used for the miniature radar system were completely purchased COTS products. The Pasternack PE51057 antenna installed on the roof of the Cessna 172 was verified as a viable TX antenna at the new 2.365 GHz range. For installation onboard the sUAS, the ANT-2.4-WRT-MON (monopole) by Antenna Factor is proposed as the TX antenna instead.

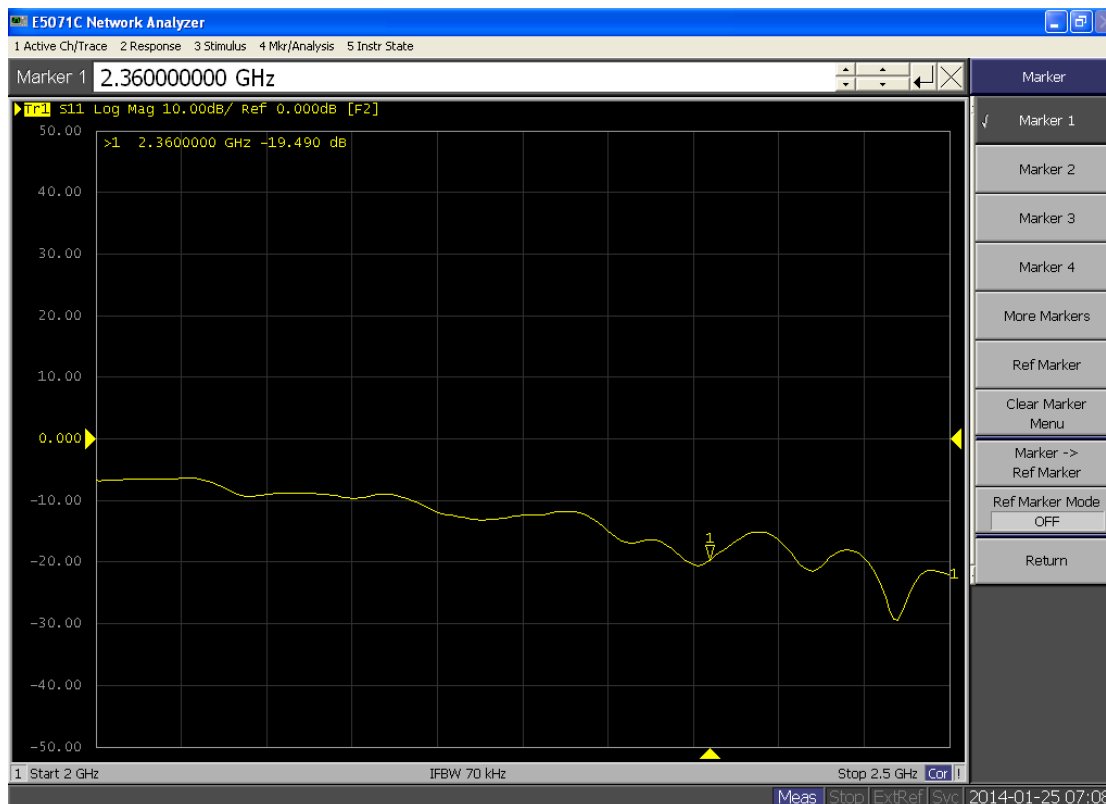


Figure 58: Sample S11 of the COTS RX antenna array. The antenna array output cables were modified with custom SMA connectors to fit the radar RX board.

The RX antenna array is Tyco Electronic's MIMO Triple Dipole, part number 1513837-1. This antenna is designed to operate between 2.4 – 2.4835 GHz with a gain of -2 dBi and a maximum transmit power of 10 W. The physical design of this COTS antenna array is suitable for interferometry in the azimuth plane having antenna to antenna separation just under a half wavelength and an equilateral triangle formation. Joining two of these antennas (base to base) yields a RX antenna array that also contains an elevation dimension. Figure 48 shows the completed RX antenna array made from two of these antenna elements.

4.2 Laboratory testing

Laboratory testing of the miniature radar system once again leveraged the loopback test setup shown in figure 33. An additional diagnostic test setup was also created using benchtop frequency synthesizers and arbitrary waveform generators to catch some critical errors. The initial miniature radar system prior to fixing these errors is known as the rev1 radar system which seemed to work during laboratory testing but failed flight testing. After finding and fixing the system errors, the rev2 miniature radar showed significant improvements over the brassboard system. Angle of arrival (AoA) phase measurements as well as a beacon target for calibration purposes was then developed to complete the laboratory testing for the rev2 miniature radar system.

4.2.1 Rev1 miniature radar system

The rev1 miniature radar system is the first working version of the reduced size, weight, and power (SWaP) radar based on the successfully flight tested brassboard system. This rev1 miniature radar utilized all of the components discussed in section 4.1 and was believed to be

working after some adjustments to various attenuator values in the TX and RX chain. Figure 59 shows an image of the rev1 miniature radar loopback test results and table 9 lists the key parameters of the test. Once again a double sideband Doppler modulation is performed for this test setup resulting in two targets at \pm Doppler. The same 800-m fiber-optic delay line was used for this test and the function generator creating the Doppler modulation was set to 500 Hz. This setup should yield the same expected 305.6-kHz beat frequency and 500-Hz Doppler frequencies calculated in section 3.3 using equation [4]. The measured target peaks have a beat frequency of 311 kHz and Doppler frequencies of \pm 504 Hz which is a reasonable match to the expected values.

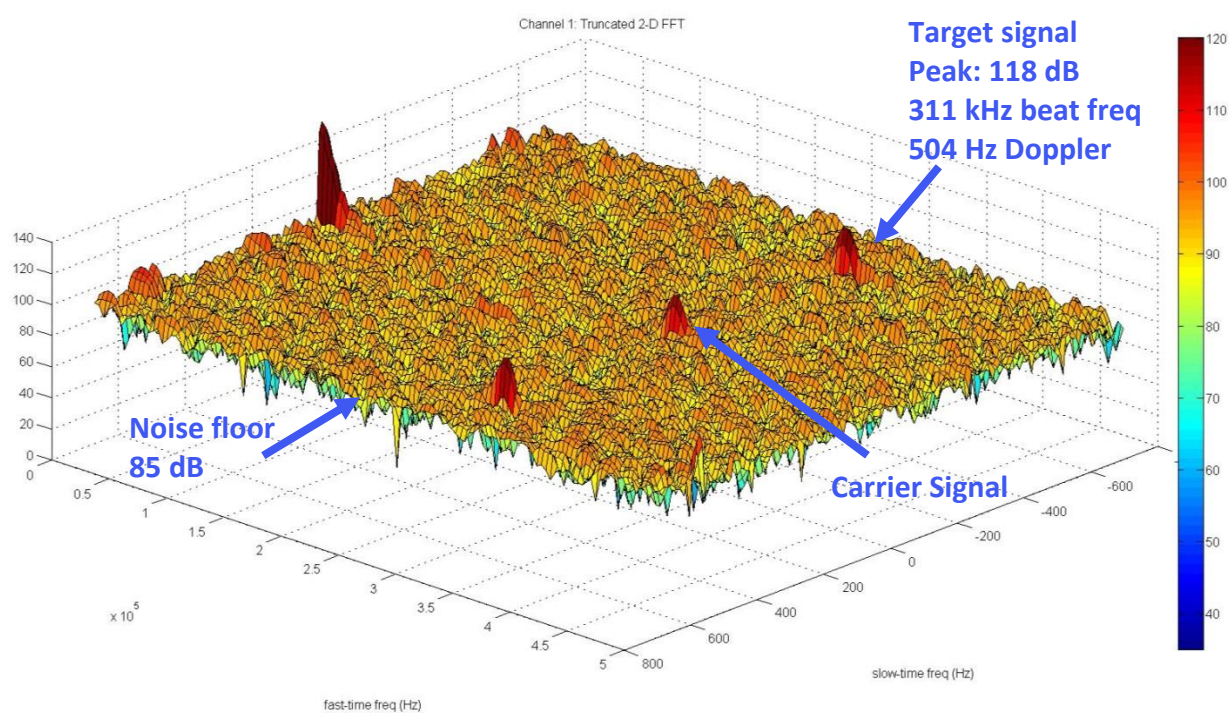


Figure 59: Rev1 miniature radar loopback testing showing double sideband modulated target and carrier signal. The value of the targets' beat frequencies and Doppler matches the expected values given the loopback test setup.

Table 9: Rev1 miniature radar loopback parameters (figure 59)

Parameter	Value
Chirp bandwidth	15.7 MHz
Chirp duration	200 μ s
TX signal power	+16 dBm
RX signal power	-121 dBm
Leakage signal power	-21 dBm
Doppler modulation	500 Hz (double sideband)
Delay line length	800 m
IF stage gain on RF board	48 dB (cascaded 24 dB Bessel HPF)

Since the same attenuation was used in both the brassboard and miniature radar loopback tests (recall that this was assumed to be 137 dB from section 3.3.2) and the TX power of the miniature radar is only 16 dBm, this implies that the RX signal power from the loopback test setup is -121 dBm. From figure 59, it can be seen that the SNR of two targets is 33 dB. Using the same logic as section 3.3 and assuming that a minimum of 10-dB SNR is required for target detection, then the minimum detectable signal is -144 dBm. Once again, using equation [1] and given the minimum detectable signal, the maximum detection range of a 1 m² RCS target can be calculated. (Note: equation [1] is duplicated below)

$$P_{RX} = \frac{P_{TX} G^2 \lambda^2 \sigma L}{(4\pi)^3 R^4} [1]$$

Assumptions:

$$P_{RX} = -144 \text{ dBm}$$

$$P_{TX} = 16 \text{ dBm}$$

$$G = 0 \text{ dBi}$$

$$\lambda = 12.68 \text{ cm}$$

$$\sigma = 1 \text{ m}^2$$

$$L = 0 \text{ dB}$$

$$\mathbf{R_{max} = 533 \text{ m}}$$

This means that with the given miniature radar performance demonstrated in the loopback test, and assuming no extra losses, the maximum detection range is 533 m for a 1 m² RCS target (only

a 22-m improvement on the brassboard system). This may seem counter intuitive since the miniature radar was able to produce 5-dB more SNR than the brassboard radar but the miniature radar's shorter wavelength, λ , offsets these benefits.

Upon further inspection, one of the concerns with the 2-D FFT processed image of figure 59 is the fact that both the noise floor and SNR have increased relative to the levels seen in figure 34 (note: the color scale is the same in both figures). It was incorrectly assumed that this is a result of the more significant IF stage amplification and that if necessary, adjusting the ADC's PGA would offset this phenomenon. A few attempts were made at flight testing this rev1 miniature radar system in November 2014 onboard the same Cessna 172 that was used for the brassboard radar tests against the same tower all of which resulted in failure (see figure 60). This prompted a full investigation into the performance of the rev1 miniature radar system using a new series of diagnostic tests that is briefly outline in section 4.2.2.

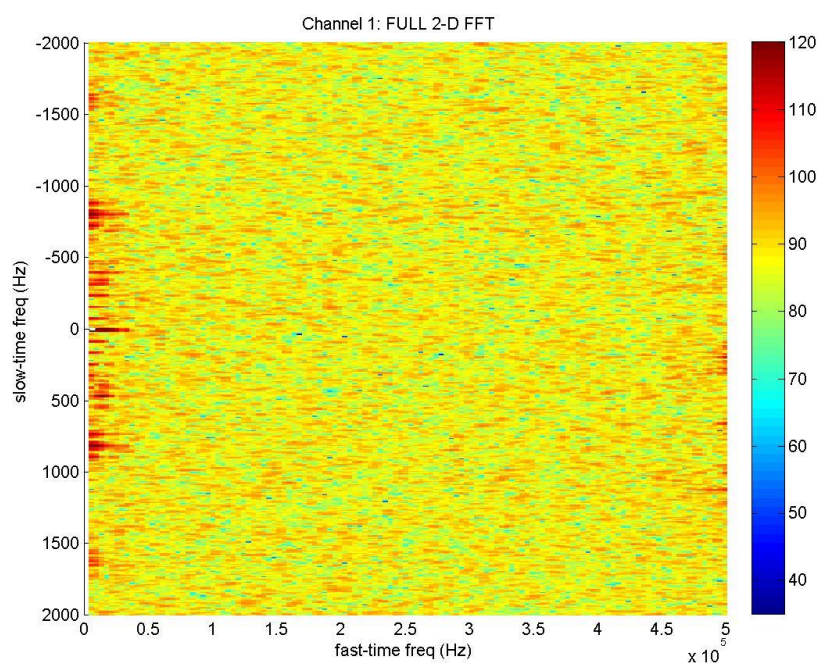


Figure 60: Top view of a full 2-D FFT processed image from the rev1 miniature radar captured from the Cessna 172. Note that the full Doppler dimension (± 2 kHz) are shown for diagnostic purposes.

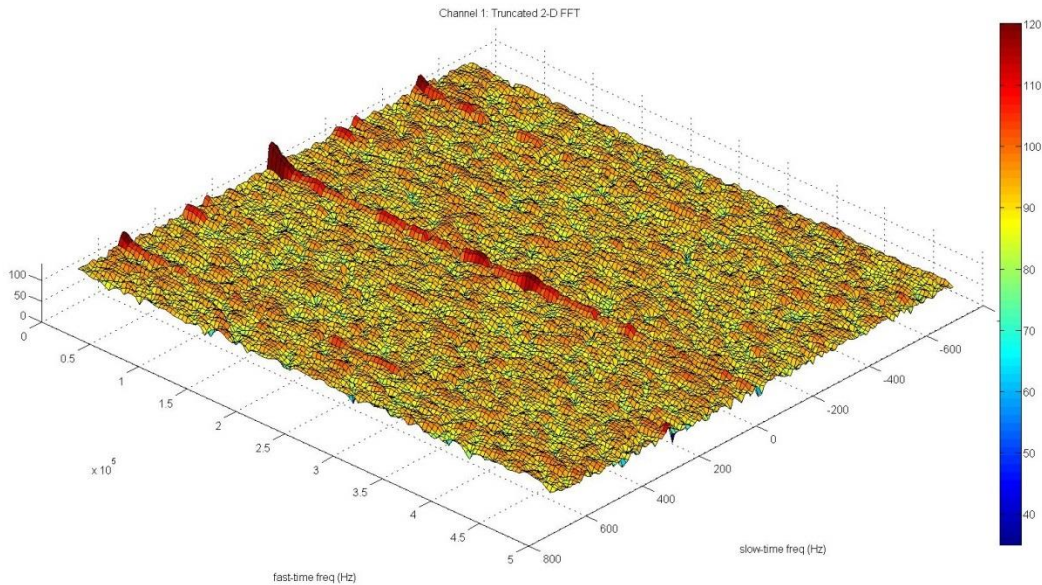


Figure 61: Rev1 miniature radar roof top testing against moving cars. Results show no detectable targets and significant noise floor compared to the brassboard flight test data.

4.2.2 Diagnostics procedure

The jump from the brassboard radar to the rev1 miniature radar system introduced more unknown variables than previously anticipated. The diagnostic tests described in this section were performed as a systematic way of dissecting the effects of the individual changes. After obtaining results shown in figures 60 and 61, it was assumed that the elevated noise floor was more than just the result of increased IF stage gain and that the cause of this effect was masking the target signals. It was hypothesized that the elevated noise floor could be caused by the switching power supply powering the RF components, the WFG creating a noisy chirp, or unknown coupling from the transmitter to the receiver.

The effects of the 5V switching power supply on the RF components were tested by using a linear benchtop power supply as a substitute. The potentially noisy chirp signal was tested by replacing it with a benchtop arbitrary waveform generator (AWFG). Lastly, the

potential for coupling was reduced/removed from the equation by physically separating the TX and RX chains using two different RF boards; one with only the TX chain active, the other with only the RX chains active. Utilizing the two separate RF boards, a series of loopback tests were performed across a combination of different power supplies and waveform generation methods. Figure 62 is a chart that lists the noise floor performance with each combination. Note that in addition to chirp waveforms, a single tone sinusoid at 2.365 GHz was also used as a TX signal since this tested whether or not the WFG noise came from chirping or is inherent to the device.

From the chart in figure 62, it can be seen that the difference in noise floor levels between the switching power supply vs the benchtop power supply did not affect the noise floor. However, changing the waveform generation method from the ADF4158 to the AWFG did reduce the noise floor by approximately 5-10 dB. The noise floor values is an average of a sub

	Dig PWR Supply	Bench PWR Supply
Dig WFG	Terminated TX chirp: 81.6 dB Loopback chirp: 87.8 dB Loopback Tone: 86.8 Note: 500 kHz noise	Terminated TX chirp: 78.7 dB Loopback chirp: 87.0 dB Loopback Tone: 82.5 Note: reduced 500 kHz noise
Bench WFG	<i>When quiet</i> Terminated TX chirp: 78.7 dB Loopback chirp: 78.9 dB Loopback Tone: 77.9 Note: tone loopback always quiet	<i>When quiet</i> Terminated TX chirp: 78.1 dB Loopback chirp: 78.8 dB Loopback Tone: 77.4 Note: tone loopback always quiet

Figure 62: Noise floor analysis using a combination of power supplies and waveform generators.
 1. Dig PWR Supply is a switching 5V power supply from the radar digital board. 2. Bench PWR supply is a linear 5V benchtop power supply. 3. Dig WFG is the ADF4158 FMCW WFG built into the radar digital board. 4. Bench WFG is a programed signal using a benchtop arbitrary waveform synthesizer.

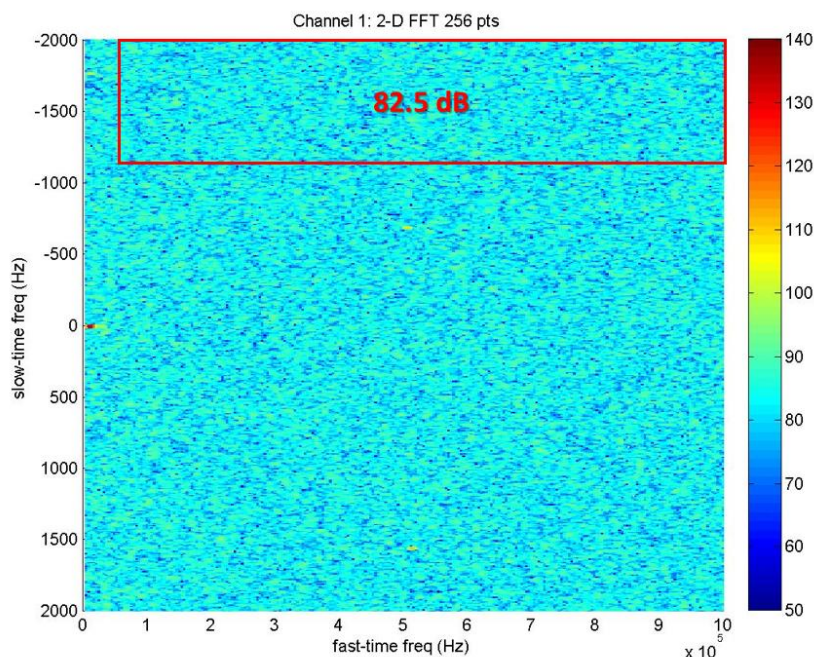


Figure 63: Subarea of 2-D FFT radar image used to calculate the average noise floor. The red box is a common quiet zone amongst all of the setups shown in figure 62.

region within the 2-D FFT processed image (figure 63) that had been shown to be void of artifacts from all combinations.

Since the AWFG resulted in lowered radar noise floor, an artificial loopback test using the AWFG was created. The test setup is shown in figure 64 where the AWFG was used to create two synchronous chirp signals of 15 MHz bandwidth with center frequencies offset by 300 kHz. These signals are mixed up to a center frequency of 2.365 GHz and BPF using the connectorized evaluation SAW filters to mimic the expected output of the FMCW radar system. The top right corner of figure 64 shows a MATLAB plot of the measured spectrum of the AWFG's chirp signal which has signal strength of -10 dBm. One of the chirps is sent to the TX chain on RF board 1 while the other chirp is amplified and sent to the RX chain on RF board 2 (into the IF down conversion mixer's LO port after some amplification). The output of the

transmit chain is heavily attenuated by -100 dB and fed into the receiver input. The result at the receiver is an input chirp that is offset from the mixer's LO chirp by 300 kHz which is the same scenario as delaying the transmit using the loopback delay line creates. Thus a 2-D FFT radar image can be created from the IF frequency produced using this imitated loopback test.

The expected output of the radar image is a single peak at 300 kHz in fast time and 0 Hz in Doppler; much like the carrier signal in figure 59 but with a lower noise floor. The results though, showed a variety of other anomalies in addition to the expected peak at 300 kHz as seen in figure 65.

The results of figure 65 pointed towards additional errors that existed in the digital system. Furthermore, these errors were hypothesized to be a part of the original target signal energy that is dispersed in range and Doppler due to improper pulse compressed. After a long series of testing it was discovered that the result seen in figure 65 is caused by a bit error in the fast-time Hanning-windowed ADC data produced by the FPGA.

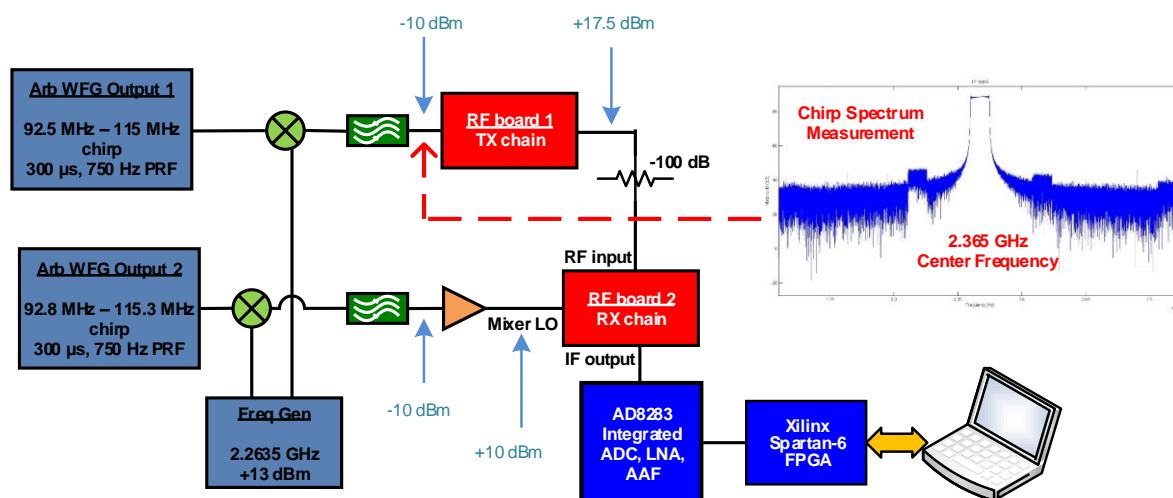


Figure 64: Block diagram of radar digital test using arbitrary waveform generator for chirp waveform creation. The two synchronized WFG outputs are offset by 300 kHz which simulates the delay of the loopback test setup.

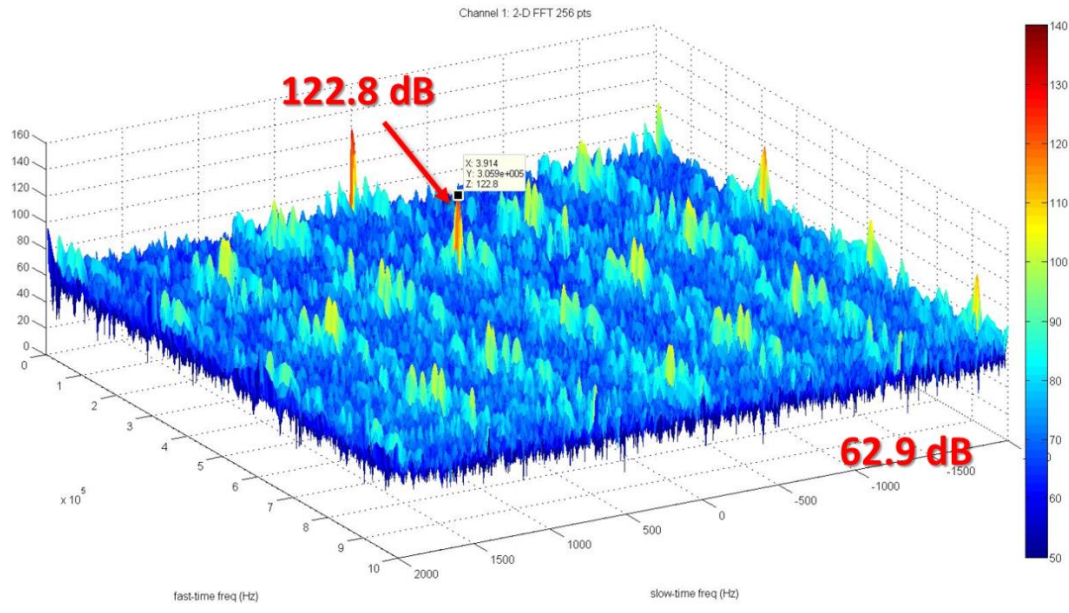


Figure 65: 2-D FFT radar image produced using the AWFG to imitate a loopback test. The test setup using the AWFG shown in figure 64. The marked peak is the expected target but the rest of the periodic anomalies are the result of additional errors in the miniature radar digital system.

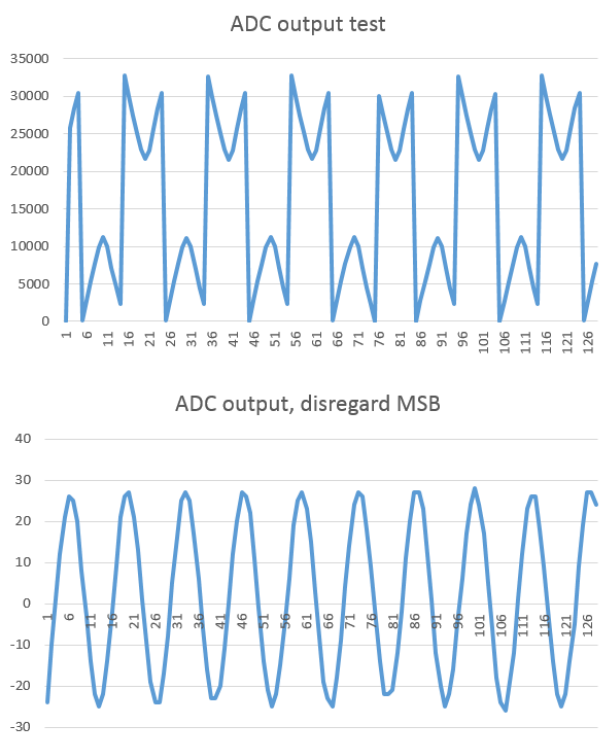


Figure 66: Plots of the ADC sampled data for a sinusoidal input in the miniature radar digital board. (top) ADC data with MBS low bit error. (bottom) ADC data after discarding the MSB bit showing ideal sinusoid.

Testing revealed that the expected MSB bit of the 16-bit windowed ADC value is constantly held low. The results of this effect is best seen in figure 66 (top) where the ADC digitizes an ideal sinusoid produced by a function generator and multiplies that with a rectangular window function. Since the MSB bit never toggles, all of the values are positive and wrapping in the data occurs. A quick fix to this error was performed by simply doing a bit shift to the left which changed the digitized results to that shown in figure 66 (bottom).

Applying this digital fix to the more complex version of the AWFG loopback imitation test resulted in the 2-D FFT processed radar image shown in figure 67. A few key factors to point out about figure 67.

1. A complex version of the AWFG loopback imitation setup was used where double sideband Doppler modulation is also applied to the imitated target signal.
2. Both the RX channels are shown in one image indicating that both channels are behaving properly. The channels are labeled in figure 67.
3. The transmit signal strength has been increased from +17.5 dBm to +25 dBm but the attenuation in the target signal path has also be increased by 10 dB offsetting this effect.
4. The color bar for figure 67 is changed to range from 0 dB to 100 dB to more clearly separate the targets from the noise. By comparison, figure 65 used a color bar that ranges from 50 dB to 140 dB.

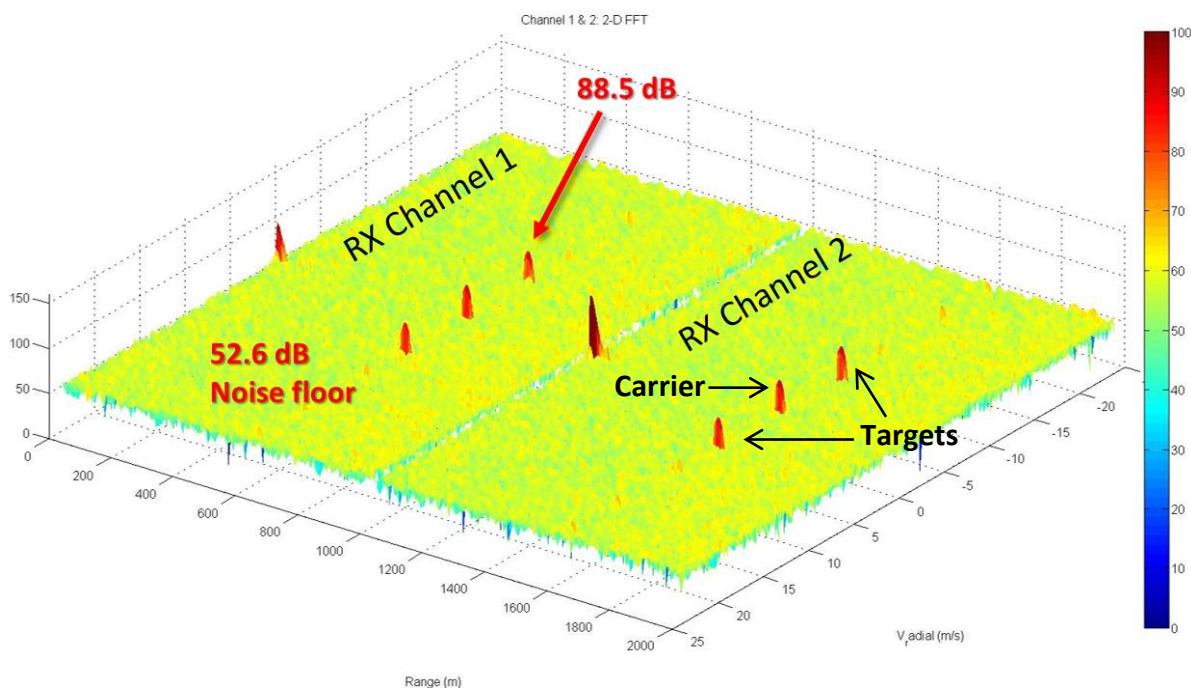


Figure 67: 2-D FFT radar image of both RX channels with ADC MSB error fixed. Generated using the same AWFG imitated loopback test setup shown in figure 64.

4.2.3 Rev2 miniature radar system

Target detection

The rev2 miniature radar system is a modification of the rev1 radar utilizing all of the lessons learned in the previous testing as well as a few additional components. The rev2 radar has the ADC MSB bug fixed but continues to use the non-ideal ADF4158 WFG on the radar digital board for simplicity and portability. It also uses a temporary external power amplifier to increase the transmit power to +25 dBm as well as two external LNAs on the RX chain to enhance the receiver noise figure. The loopback result of the rev2 miniature radar system is shown in figure 68 while table 10 lists the key parameters of the test.

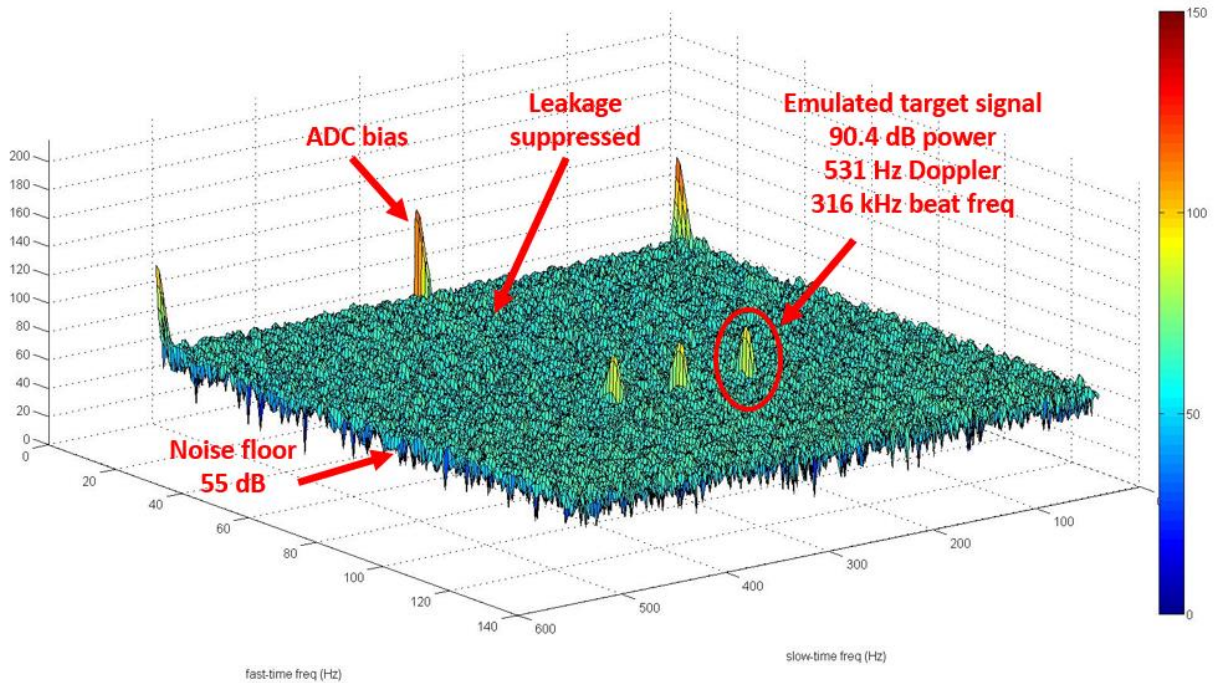


Figure 68: Rev2 miniature radar loopback result showing 35 dB SNR using the parameters listed in table 10.

Table 10: Rev2 miniature radar loopback parameters (figure 68)

Parameter	Value
Chirp bandwidth	15.7 MHz
Chirp duration	200 μ s
TX signal power	+25 dBm (w/ external TX amp)
RX signal power	-122 dBm*
Leakage signal power	-25 dBm
Doppler modulation	500 Hz (double sideband)
Delay line length	800 m
RX gain	83.5 dB (not including ADC PGA)
RX noise figure	5.82 dB

* Extra 10 dB target signal attenuation added to the loopback test setup compared to tables 6 and 9

The targets' beat frequency and Doppler is relative close to the expected values of 305.6 kHz and 500 Hz respectively and offsets in Doppler are attributed to timing biases between radar and function generator. Again the maximum detection range of a 1 m² RCS target can be calculated assuming a minimum 10-dB SNR detection requirement. Given the 35-dB SNR

shown in figure 68 which was obtained from an estimated RX power of -122 dBm, the minimum detectable signal strength is -147 dBm. Using equation [1] duplicated below and the associated assumptions, the maximum detection range of the rev2 miniature radar system is calculated to be 1063 m which is a significant improvement upon the brassboard radar (511 m) and the rev1 miniature radar system (533 m).

$$P_{RX} = \frac{P_{TX} G^2 \lambda^2 \sigma L}{(4\pi)^3 R^4} \quad [1]$$

Assumptions:

$$P_{RX} = -147 \text{ dBm}$$

$$P_{TX} = 25 \text{ dBm}$$

$$G = 0 \text{ dBi}$$

$$\lambda = 12.68 \text{ cm}$$

$$\sigma = 1 \text{ m}^2$$

$$L = 0 \text{ dB}$$

$$\mathbf{R_{max} = 1063 \text{ m}}$$

Angle of arrival (AoA)

Recall that one of the added capabilities of the miniature radar system is the RF switches in the RX chain which allows different antenna pairings to be cycled resulting in ability to gather radar data from all three necessary antenna pairs to produce unambiguous azimuth and elevation AoA estimation. Once the rev2 miniature radar system successfully demonstrated superior loopback test results, the AoA estimation capability was evaluated.

In the loopback test setup the same time delayed target signal is split four ways and sent to all four radar RX channels using matched length cables (see figure 33). It was expected that phase biases may exist between RX channels but the phase difference (i.e. delta phase, δ_{AB}) between these channels should remain consistent. Once the bias is calibrated out, the phase difference can be used to interpret the target AoA using equations [3] from section 2.3.

Table 11: Rev2 miniature radar phase differences from loopback test setup

FPGA RF switch control	RX channels	Mean phase difference (target 1)	Mean phase difference (target 2)	Standard deviation (target 1)	Standard deviation (target 2)
Antenna Select 0	RX1 and RX3	15.9°	15.7°	1.68°	1.74°
Antenna Select 1	RX2 and RX3	21.6°	21.4°	2.18°	1.17°
Antenna Select 2	RX2 and RX4	7.3°	7.3°	2.07°	1.92°

It was discovered however that the phase difference between loopback emulated targets had varying phase difference and significant biases which were attributed to phase drifts in the active components of the RX chains. This issue was eventually resolved with some additional development yielding the channel-to-channel phase difference characteristics outline in table 11.

Having obtained a phase difference standard deviations of less than 3° the rev2 miniature radar was moved to roof top calibration and testing against moving cars. It should be noted though that the phase difference is not the same as AoA which involves an inverse cosine term and is dependent on the ratio of antenna separation to wavelength (see equation [3]).

4.2.4 Comparison to simulation

In section 2.4 it was determined through simulation that the 2-D FFT provided 56 dB SNR improvement and that with this processing capability, a simulated input signal of -124 dBm with -110.5 dBm of thermal noise (assuming 3.5 dB noise figure for the brassboard radar) resulted in 40.2 dB SNR after the 2-D FFT. The resulting SNR of the rev2 miniature radar system shown in figure 68 and table 10 shows that for an input signal of -122 dBm with an calculated thermal noise of -108.2 (using a noise figure of 5.8 dB, see appendix A.1) the resulting 2-D FFT processed SNR is 35.4 dB which equals a 2-D FFT processing gain of 49.2 dB (SNR_{in} of -13.8 dB, SNR_{out} of 35.4 dB, therefore total SNR_{gain} 49.2 dB).

This 6.8 dB SNR discrepancy between the simulation and rev2 miniature radar performance (56 dB simulation vs 49.2 dB radar) can be attributed to two factors. First, the noise in the simulation was uncorrelated, generated using MATLAB's randn function. However, in the actual hardware, the 1-MHz bandwidth noise (due to the AAF) was sampled at 4 MSa/s. This is a 2x over sampling (since a 2-MHz Nyquist sampling rate is required) which means that the hardware thermal noise is not completely uncorrelated resulting in a 3 dB SNR degradation from coherent processing. Secondly, the signal in the hardware loopback test is double sideband modulated in Doppler which further reduces the peak power of each of the two targets by 3 dB. Therefore, the expected SNR processing gain of the rev2 miniature radar loopback test is only 50 dB which matches closely with the measured 49.2 dB.

4.3 Roof top testing

The rev2 miniature radar system was not flight tested since the certification on KU AE's Cessna 172 had expired in December 2014. Testing of the radar system in a real-world environment was performed on the roof of the KU Engineering building. The testing can be split into two separate categories, calibration and car measurements. Calibration was performed using a custom designed radar beacon that would emulate a target at range and Doppler so that the beacon signal can be separated from the stationary objects such as the buildings and ground. The car measurements were performed against moving traffic in front of the KU Engineering build on 15th Street in Lawrence, KS. The following sections will describe each of the test setups with sample results. The analysis of these results are discussed in Chapter 5: Performance analysis.

4.3.1 Calibration target

The calibration target was designed as a way to characterize the miniature radar's AoA estimation capability in a real-life environment. In the future, once the radar is mounted to an

aircraft, the beacon target can be used to align the radar's AoA estimation with the aircraft body coordinates which is critical in providing accurate and reliable target data. This step was not as critical for the elevation antennas used in the flight testing of the brassboard radar because that antenna array simply had to be relatively vertical in orientation to determine if targets were above or below the horizon. The rotational orientation of the azimuth array about the z-axis however, could produce significant biases and false interpretation of the radar data. Furthermore, it was discovered that targets aligned with the baseline between two azimuth antenna pairs could not be reliably detected meaning that with a two channel receiver such as the rev2 miniature radar, certain orientations are more preferable than others.

The calibration target itself is simply a beacon that radiates the radar's TX signal back towards the receiver after applying a Doppler modulation. Figure 69 shows a block diagram of the beacon calibration target. Note that between the RX and TX antennas, a total of 22 dB of gain is applied. The antenna to antenna coupling was measured to be less than -40 dB thus oscillation was not detected.

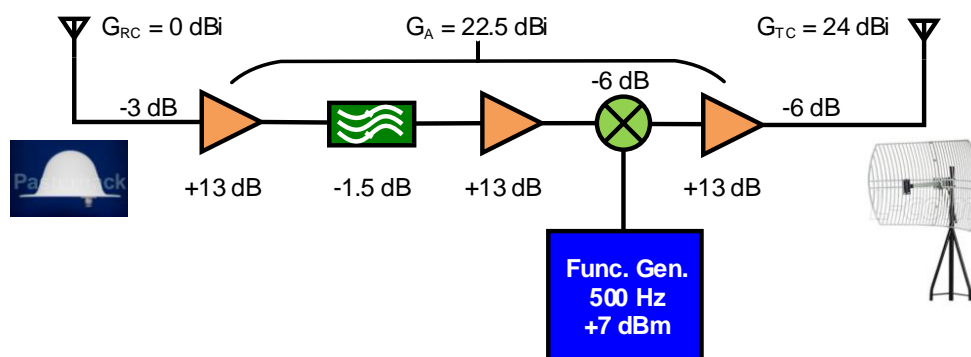


Figure 69: Calibration beacon target block diagram.

A function generator is used to produce a 500-Hz Doppler modulation. A directional antenna is used to provide more gain to the beacon setup creating a larger RCS and reduces the potential for multipath.

The RCS of the active beacon calibration target, σ_C , is given by equation [6] below where λ is 12.68 cm, G_{RC} is the gain of the receiving antenna, G_{TC} is the gain of the transmitting antenna, and G_A is the overall gain of the RF components between the two.

$$\sigma_C = \frac{\lambda^2}{4\pi} G_{RC} G_{TC} G_A \quad [6]$$

All of the gain values in equation [6] are given in figure 69 and results in a beacon calibration target with 17.57 dBsm target. The calibration target was setup on the roof of the engineering building approximately 20 meters apart from the radar TX and RX antennas. Figure 70 shows a photo of the setup of the calibration beacon setup on the roof and figure 71 is a high level block diagram of the setup.

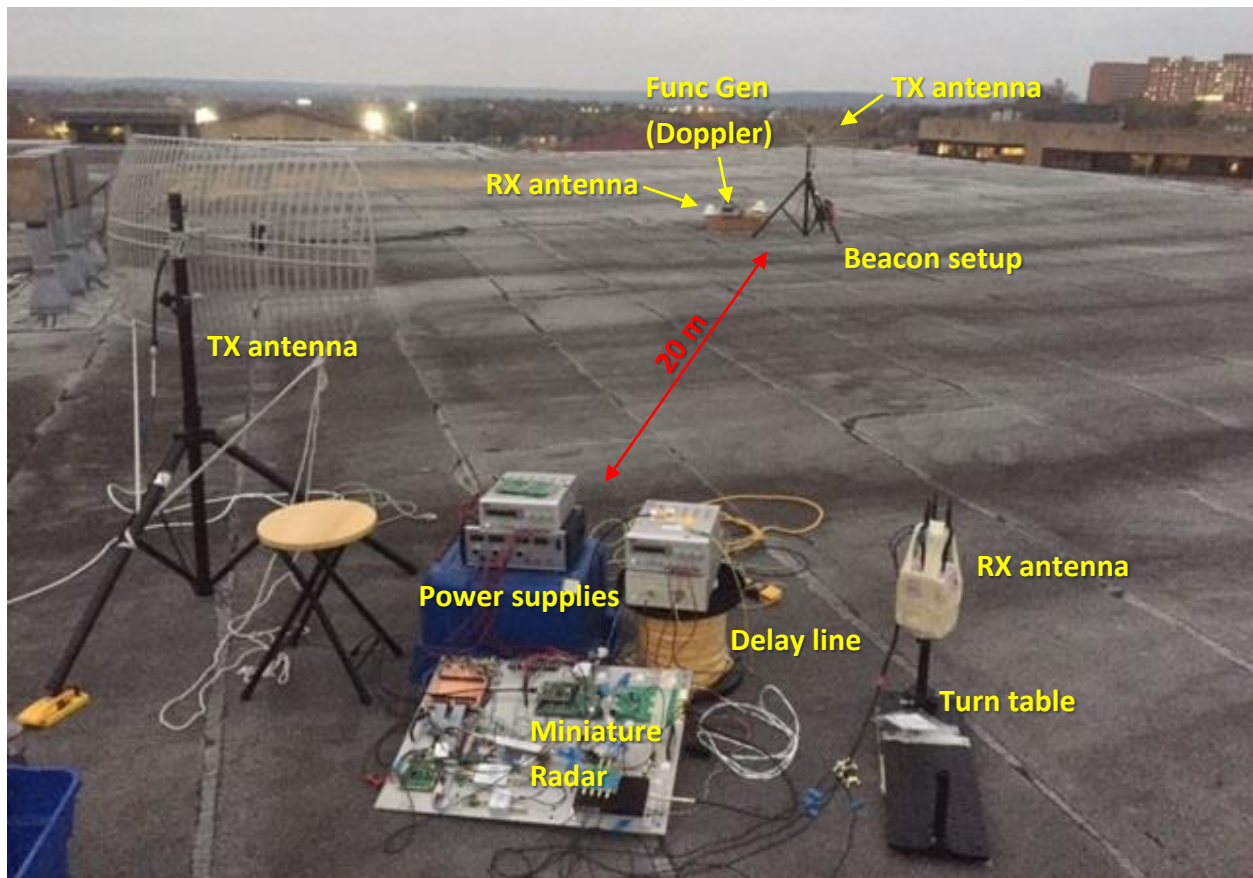


Figure 70: Calibration beacon target setup on the roof of KU's engineering build.

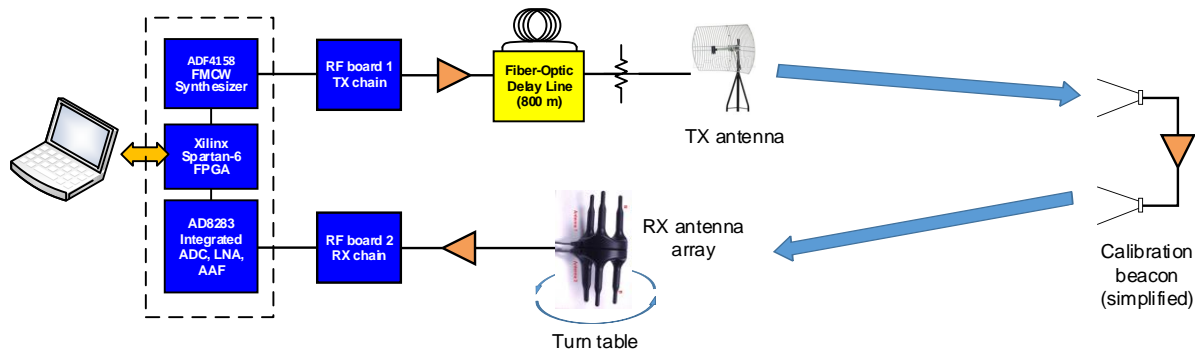


Figure 71: Calibration beacon target test setup block diagram.

Note that the calibration beacon is a simplified drawing, refer to figure 69 for the beacon block diagram.

There are several details to point out about the roof top calibration target testing. The following is a list of the critical details (reference figures 70 and 71).

1. The RX antenna array is mounted on a turntable so that incremental rotations can be accurately made during data gathering.
2. The TX antenna is modified to a dish antenna for more gain and directivity towards the beacon target.
3. The actual TX and RX signal levels are unknown, attenuators were experimentally added to the TX chain until an acceptable loopback test result was obtained (acceptable in the sense that it looked similar to the loopback test results).
4. While the beacon and the radar are physically separated by approximately 20 m, the 800-m fiber-optic delay line is inserted before the TX antenna causing the beacon target to look as if it was 600-m away (i.e. the beacon target will have a fast-time beat frequency of approximately 300 kHz, similar to the loopback test results).
5. A 500-Hz double sideband Doppler modulation was used on the beacon target setup. This coupled with the 800-m delay line means that the beacon target's signature should be identical to the loopback test setup.

6. The miniature radar system is mounted on the same aluminum plate as the former brassboard radar for portability and to use its battery as a power supply for eventual manned flight testing
7. The TX and RX chains of the radar system is still split by using two separate boards. It is believe however that this is no longer necessary.
8. Azimuth angular measurements were made in 10° angular cuts throughout a total 360° rotation.
9. Elevation angular measurements were made in 5° angular cuts from -20° to $+20^\circ$ and 10° angular cuts from $\pm 20^\circ$ to $\pm 60^\circ$.
10. For the elevation angular measurements, the antenna array was mounted sideways onto the turn table and the dish antennas on calibration beacon was changed to horizontal polarization. Note that the transmit dish antenna on the radar as well as the RX dome antenna on the beacon were left vertically polarized.
11. At each angular cut (azimuth and elevation) a total of at least 60 data samples were gathered. Note that the data samples were gathered from alternating antenna selections pairings such that 20 samples are from antenna select 0 pairing, 20 samples form antenna select 1 pairing, and 20 samples from antenna select 2 pairing (reference table 8).
12. Figure 72 illustrates the starting position of the RX antenna array relative to the calibration beacon target for both the azimuth and elevation angular cuts as well as the clockwise rotation for increasing angular measurements.

Figure 73 is a sample of the calibration beacon target's signature after 2-D FFT processing. The peaks of the two targets (caused by the beacon's double sideband Doppler modulation) as

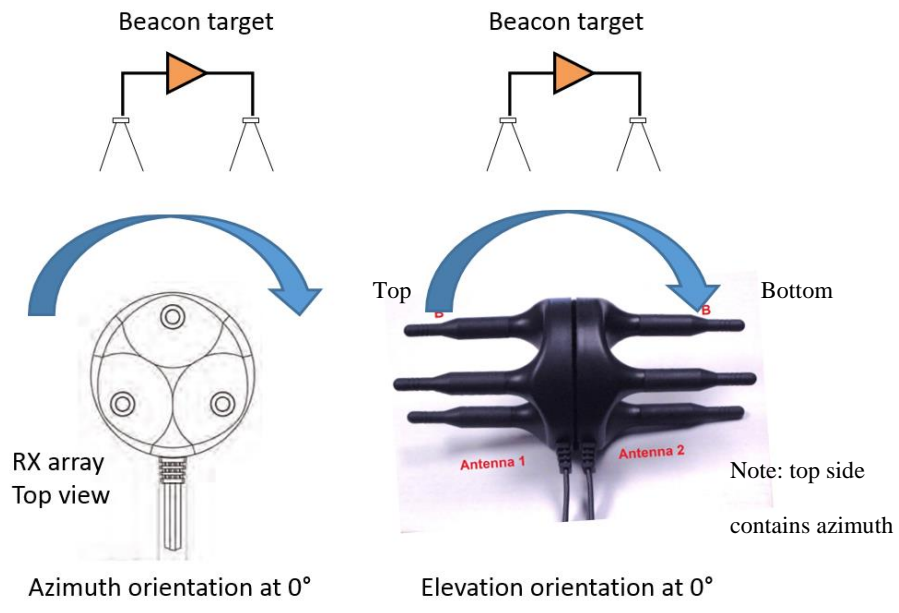


Figure 72: Starting orientation of the RX antenna array to the calibration beacon target for azimuth and elevation. From this initial position (considered to be 0°), the antenna arrays are rotated clockwise for increasing angular cuts. Note that this means the target position relative to the antenna, is rotation counter-clockwise.

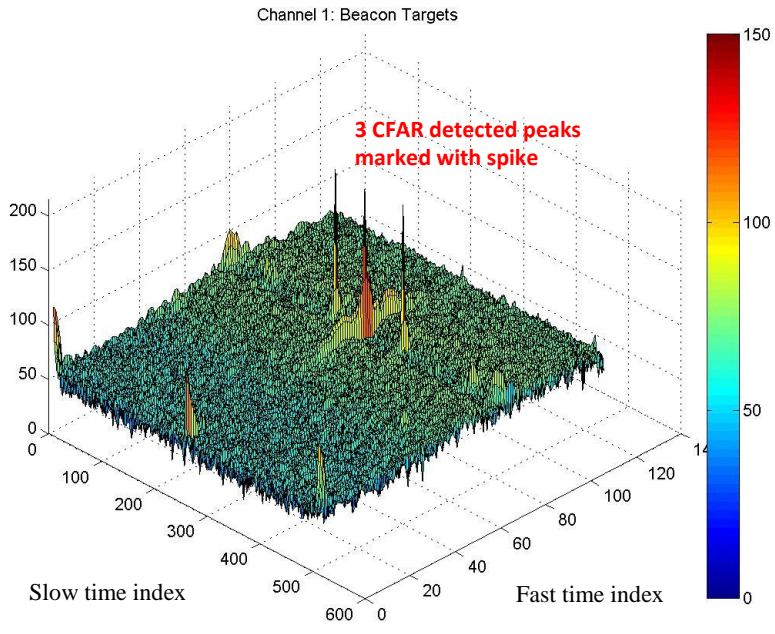


Figure 73: Sample 2-D FFT processed radar data from roof top calibration beacon testing. This sample is from an azimuth antenna at 0° angular cut. The peaks of the carrier and two targets are detected using CFAR and marked with a spike.

well as the carrier signal are detected using a constant false alarm rate (CFAR) algorithm further discussed in chapter 5. In figure 73, the detected peaks are marked with a spike for quick visual identification of the three expected pulse compressed targets.

An analysis of the calibration can be found in chapter 5 section 5.3. However, once the rev2 miniature radar was demonstrated to be working with the calibration target the system was then used to capture data on moving cars from on the engineering building roof top.

4.3.2 Moving car measurements

Measurements of moving cars is an ideal way to perform the initial rev2 miniature radar test in an outdoor environment. The potential effects of coupled aircraft noise is eliminated since the radar is on the ground. Since the radar is not moving, the echoes from stationary targets such as buildings and trees are mapped to the zero Doppler axis which is unused in target detection. Furthermore, given the 2-Hz update rate of the radar system, the slow moving cars with relatively little angular change in its geometry to the radar system is ideal for testing the AoA estimation capability of the radar.

The rev2 miniature radar system was setup on the southwest corner of the Engineering building's roof and cars driving west of the building were measured. Figure 74 shows an image of the scene as seen by the RX antenna array. The rev2 miniature radar used the same directional dish antenna for transmit that was used in the calibration beacon testing. This eliminated the potential for measuring vehicles behind the scene in figure 74 giving a-prior knowledge of the AoA of detected cars in the radar data.



Figure 74: Scene as seen by the RX antenna array.

The geometry of the scene was estimated using Google maps. Figure 75 shows that the estimated distance from the radar system to the top of the hill in the far edge of the scene is approximately 425 m. Furthermore, notice that in figure 74 the corner of the adjacent building blocks the TX and RX antennas' line-of-sight of the cars on the road. The distance of the cars on the road at this blocked at this point is estimated to be 250 m. This is a useful piece of information since it was observed that cars measured at this range are suddenly lost due to radar signals being blocked. The cars on this road typically drive at about 30 mph or 13.4 m/s. Figure 76 shows a sample of a 2-D FFT processed radar image of a single car moving towards the radar system along with the video of that car captured at the same time.

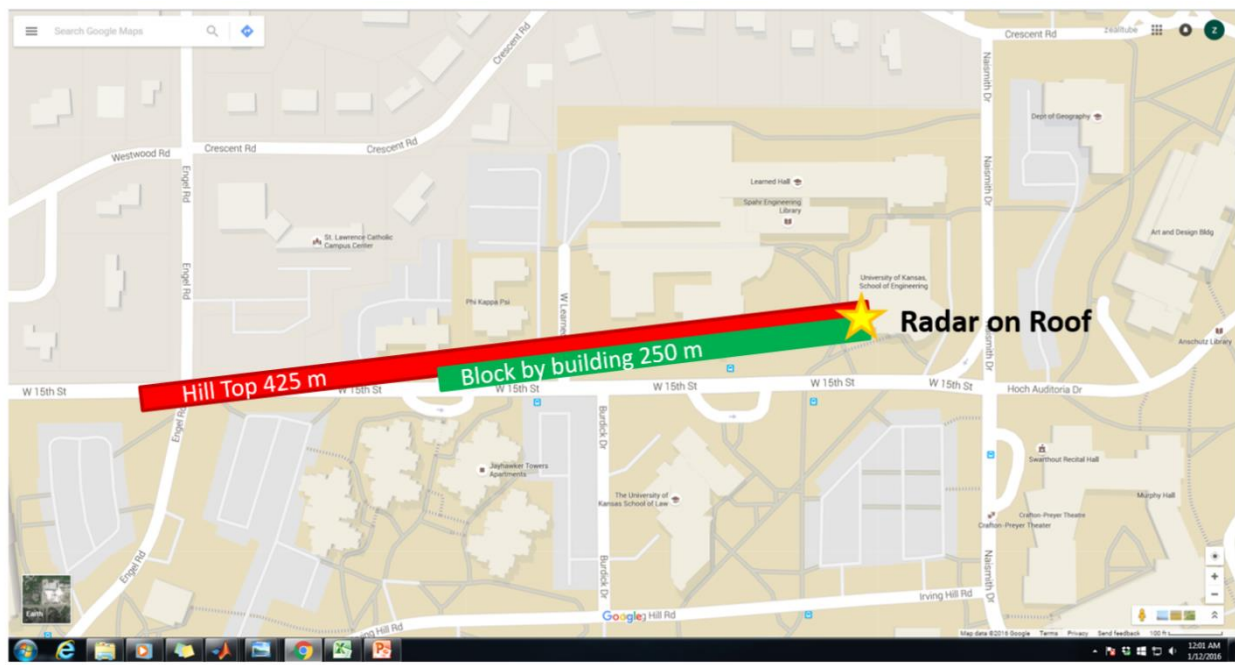


Figure 75: Estimation of range in the car measurement scene. (Red bar) Estimated distance to the top of the hill in the far edge of the scene in figure 74 using Google Maps. (Green bar) Estimated distance of cars that would be blocked by the protruding corner of the adjacent building.

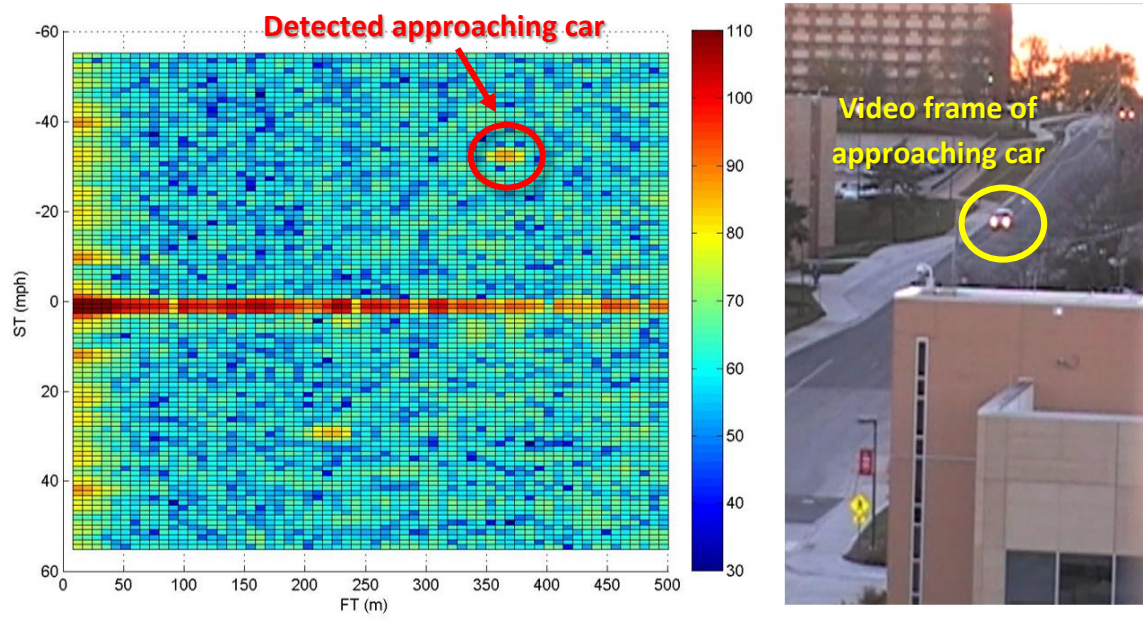


Figure 76: Sample of measured car data captured by the rev2 miniature radar system. (left) Sample 2-D FFT processed radar image showing a detected car approaching the radar system at roughly 35 mph located at a range of 375 m. (right) Image from video footage of the car in the detected radar image.

Chapter 5: Performance analysis

The performance analysis of the rev2 miniature radar system focuses on four key parameters. First is the radar's size weight and power (SWaP) which were designed to be flown onboard a sUAS. Second is the radar's ability to detect a target in range and Doppler. Third is the target angle of arrival (AoA) estimation using interferometry from the three RX antenna pairs. Lastly, the fourth capability is to perform target tracking and to determine the target's six degrees of freedom (6-DOF, i.e. XYZ location and XYZ velocities) relative to the RX antenna array.

5.1 Radar size, weight, and power

The SWaP of the rev2 miniature radar system was designed to fit onboard the 40% Yak-54 UAS which has a 10 lbs payload (shown in figure 6). The following is an analysis of each individual component (i.e. size, weight, and power) of the rev2 miniature radar system compared with the resources and limitations of the UAS.

Size

The rev2 miniature radar system's RF and digital boards (with the FPGA evaluation board) both fit within the aluminum chassis shown in figure 47 which was identified by the AE department as suitable for installation onboard the 40% Yak-54 UAS. However, the external amplifiers and other additional components appended to the radar system were not original anticipated and must be external to the chassis. The two primary external components are the TX power amplifier (Mini-Circuits' ZHL-42W+) and the RX LNAs (Mini-Circuits' ZX60-3011+). The TX power amplifiers measures approximately 17.8 cm x 8.3 cm x 7.0 cm (3 in x 3.25in x 2.75 in) while each of the two RX LNAs measure approximately 3.8 cm x 1.9 cm x 1.2

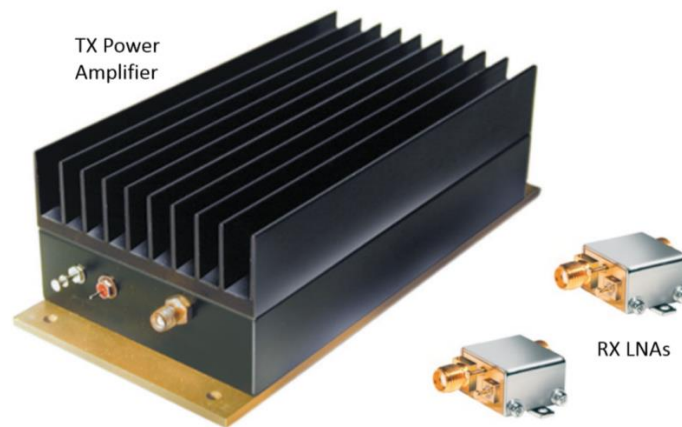


Figure 77: Rev2 miniature radar external amplifiers.
 (left) TX power amplifier, ZHL-42W+. (right) Two RX external LNAs, ZX60-3011+.
 These parts were not accounted for during the design of the miniature radar system.

cm (1.5 in x 0.75 in x 0.46 in). Figure 77 shows an image of these external components. The size and weight of the TX power amplifier makes it difficult, if not impossible, to fit onboard the 40% Yak-54 UAS. Continuing work on a rev3 miniature radar system will replace this power amplifier with one that is suitable for sUAS while the external RX LNAs will be built into the new rev3 RF boards.

Weight

The final weights of the rev2 miniature radar system is shown in table 12 below. The total weight of the system is 2.92 lbs (1.32 kg). This does not include the weight of the TX power amplifier shown in figure 77 since this component will be replaced in rev3. It also does not contain the weights of any batteries that might be necessary to power the radar system. Instead, the currently rev2 miniature radar system is designed to draw power from the 40% Yak-54 UAS which runs on a gasoline engine and is capable of carrying a small alternator. Table 12 does however, include the weights of the smaller RX LNAs from figure 77 even though these

Table 12: Rev2 miniature radar system weights

	Item	Weight (lbs)	Notes
1	RF board	0.23	Includes RX SMB cables, LO input SMA cable, fully populated TX chain
2	Digital board	0.34	Includes FPGA, ribbon cable, TX SMB cable
3	RX Antenna Array	0.79	2x Tripod antenna with associated cables
4	TX Antenna	0.04	miniature monopole
5	SMA cables	0.30	TX and RX cables, 5 cables total, approx. 5 ft/cable. (0.06 lbs per cable)
6	Aluminum chassis	0.80	Including both end covers
7	USB cable	0.08	USB cable for communication with Tegra K1
8	Flash Drive	0.02	Data storage, could swap to a mini-SDHC card where weight is negligible
9	External LNAs	0.24	Currently 4 external LNA used per RX channel.
10	Other hardware	0.08	Additional hardware not mentioned in this dissertation.
	TOTAL*	2.92	1.32 kg or 46.7 ounces

* Note: Does not include the weight of any additional logic devices (beyond the FPGA) that could be needed to replace the user laptop.

will be replaced in rev3. Lastly, table 12 does not include the weight of a logic device that would replace the user computer, however, recent developments in this area (beyond the scope of this dissertation) would indicate that this logic device would weigh no more than 1 lbs.

Power

Including the external power amplifier and LNAs, the total rev2 miniature radar draws 22.5 W (12.5 V, 1.8 A). According to the datasheets, the external TX power amplifier draws approximately 9.8 W while the external RX LNAs drawn 2.9 W total. This leaves 9.8 W between the radar digital and RF systems. It is unknown how much power the total rev3 miniature radar system will draw at this point but it is expected to be less than the current 22.5 W.

5.2 Target detection in range and Doppler

During the majority of the brassboard and miniature radar systems testing, target detection was made by visual inspection after post processing. However, the radar onboard the sUAS must make automatic target detection in real-time and ideally relay only target information such as range and Doppler to the aircraft flight director or autopilot. Thus, a method for target detection was investigated and will be discussed in this section.

Target detection in range and Doppler was performed on the 2-D FFT processed radar image using a Constant False Alarm Rate (CFAR) detection algorithm implemented in MATLAB. Figure 78 illustrates this process for a single pixel in the range-Doppler radar image that will be referred to as the cell under test (CUT). The CFAR algorithm is ran on every possible cell within a 2-D FFT radar image except for the four rows or columns near the edges of the image (edge cases). The analysis of each CUT is performed using the following processing:

1. Determine if the current CUT is a local maxima.
2. If it is then compare its value to the value of the average surrounding noise floor minus the 8 guard cells that immediately surround the CUT (see figure 78).
3. If the CUT is at least some threshold value (typically 10 dB) higher than the average surrounding noise floor then flag it as a detected target.
4. If the CUT does not meet the threshold or is not a local maxima then move on to the next cell in the image.

The CFAR process described was performed on the rev2 miniature radar loopback test data as well as the calibration beacon test data. As seen in figure 73 (from the calibration beacon test), the CUTs that met the CFAR criterial were flagged by the algorithm and marked with a large spike for quick visual identification. The following images in figure 79 shows four

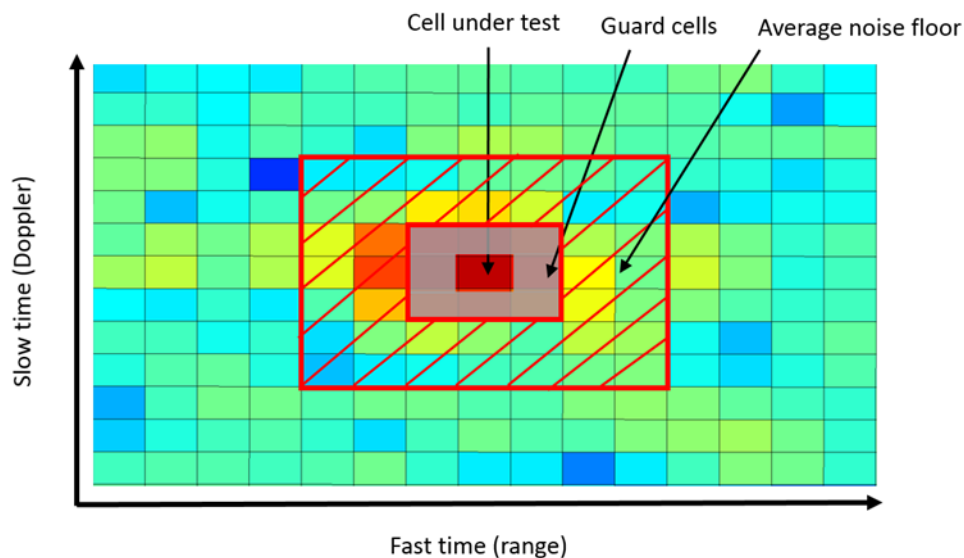


Figure 78: CFAR detection example for the radar's range-Doppler image. The cell under test is compared against the average noise floor to see if it meets a detection threshold to be flagged as a target.

samples of CFAR detection results from the rev2 miniature radar cars measurement testing described in section 4.3.2. Note that the SNR threshold of detection was set to 15 dB for this dataset. Circled in the four radar image samples shown in figure 79 is a detected car that is approaching the radar system; this is the same car that is seen in figure 76.

A total of approximately 12 sec of radar data was gathered with the car present in the radar field of view (recall that the radar used a directional TX antenna for this set of measurements). The CFAR algorithm was applied to all 22 radar updates and successfully detected the car over this duration. Figure 80 is a scatter plot of all of these detected instances as the car approached the radar system showing a clear range-Doppler trail being drawn out over time (figure 80, circled in red). Note that the noise at zero Doppler and near zero range (40 m) are ignored.

Car Testing – AntSel0, channel 1

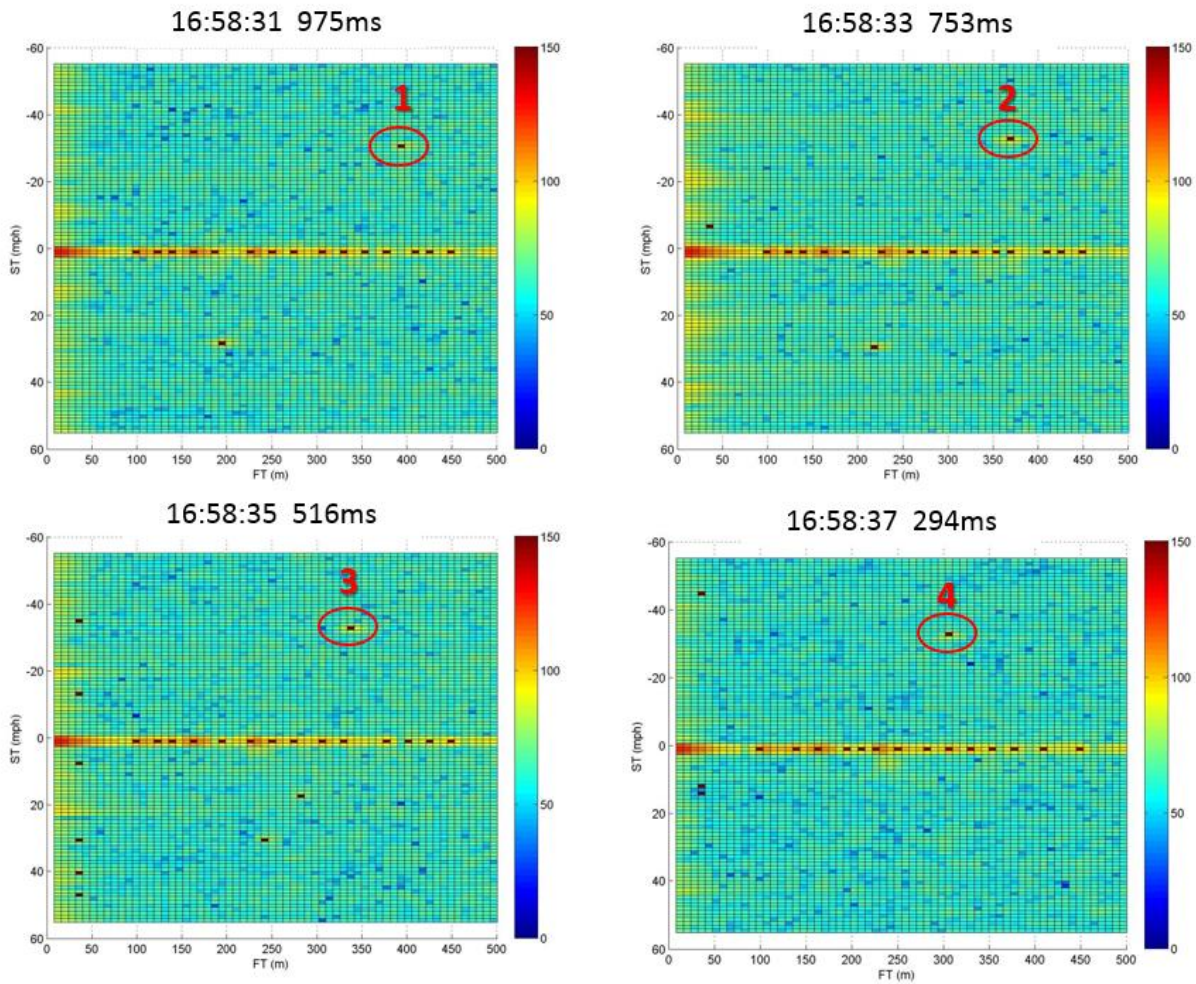


Figure 79: Sample CFAR processed car measurement images captured by the rev2 miniature radar . The four samples are chosen at 2 second intervals. Circled in red is an approaching car detected by the radar. This is the same car shown in figure 76.

In MATLAB, the CFAR process described was fairly efficient and, by observation, could easily be run in real-time with the current radar's 2-Hz update rate. Recent developments, beyond the scope of this dissertation, have shown that the NVIDIA Tegra K1 multicore processor is capable of performing CFAR radar processing at the intended 10-Hz radar update rate using its graphical processing unit (GPU) capabilities.

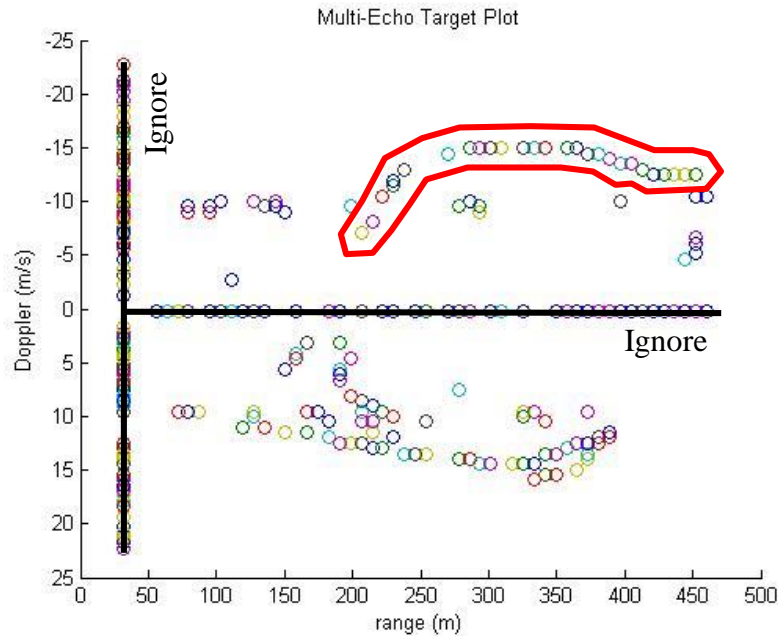


Figure 80: Scatter plot CFAR detected cars over a 12-sec interval. Circled in red is a approaching car from the top of the scene (figure 74) moving at 15 m/s (33 mph).

5.3 Angle of arrival estimation

The target angle of arrival estimation (AoA) is performed by the radar system to determine the angular location of the detected targets relative to the RX antenna array. Since the radar system is intended to use isotropic antennas for both transmit and receive (therefore, avoiding the need for scanning), targets detected in range and Doppler could be located anywhere around the radar. Interferometry using the radar receive antennas in pairs was performed to estimate the AoA of the target echo detected in the range-Doppler map.

This AoA estimation process was further broken into four steps. The first step was to process and obtain the phase difference data from the calibration beacon measurements across all of the angular cuts (azimuth and elevation). The second step was to create a simulation of the expected phase difference to AoA estimation performance based on the physical antenna array dimensions obtained through data sheets. The third step was to fit the simulation to the

measured data by removing biases and adjusting the measured/assumed antenna to antenna spacing in the RX array to obtain a mapping of calculated AoA to measured RX antenna rotation. The fourth step is to apply this mapping to the measured car data shown in figure 80. These steps were all performed with the anticipation of calculating the target's 6 degrees of freedom (6-DOF, i.e. XYZ location and XYZ velocities) relative to the radar system in section 5.4.

5.3.1 Calibration beacon measurements

As mentioned before the first step in the AoA estimation process was to gather data at various known angular cuts in both azimuth and elevation from a known target. This was performed using the calibration beacon test setup described in section 4.3.1. This test was split into two parts, azimuth angular cuts and elevation angular cuts. The following summarizes the data gathered from each.

Azimuth

The calibration beacon azimuth angular cuts contain data measured from 0° to 360° in 10° increments. At each angular cut, the radar recorded at least 20 updates per antenna select pairing. CFAR was then performed on all of the radar updates (two radar images per update) to detect the two targets and the carrier signals produced by the calibration beacon in each radar image. The phase differences of the same detected targets across both radar images were recorded as well as the SNR. Once these phase differences had been gathered for each target across all 20 radar updates, the average SNR, average phase difference, and phase difference standard deviation were calculated from the data set.

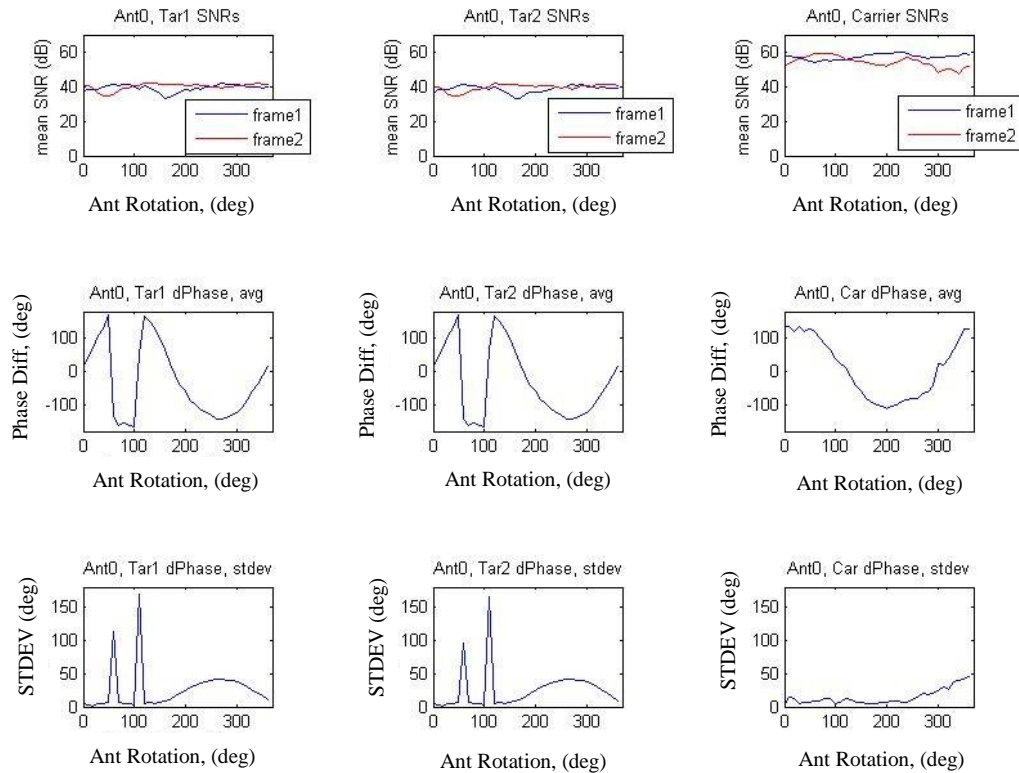


Figure 81: Azimuth calibration target phase difference measurement from antenna pairing 1 (Ant Sel 0). (Top row) Average SNR of targets 1, 2 and carrier vs RX antenna rotation. (Mid row) Average phase difference of the same target captured by the azimuth antenna pair. (Bot row) Standard deviation of the phase differences.

Once again the above process was performed at each angular cut from 0° to 360° and figures 81 and 82 shows these results over the entire azimuth cut for each of the two azimuth antenna pairings (antenna select 0 and antenna select 1, ref figure 48 and table 8).

Visual observation of the phase difference plots for target 1 and target 2 in figures 81 and 82 (i.e. middle left and center plots in each figure) show that there is a distinct sinusoidal shaped relationship between the phase difference and RX antenna rotation (i.e. AoA). This is expected since there is a \cos^{-1} relationship between the phase difference, δ_{AB} , and the AoA, θ_{AB} , as seen in equation 3. It can also be seen that there are certain rotation angular cuts where phase wrapping occurs in the data. Rather than trying to fit the phase difference to an ideal sinusoid that is

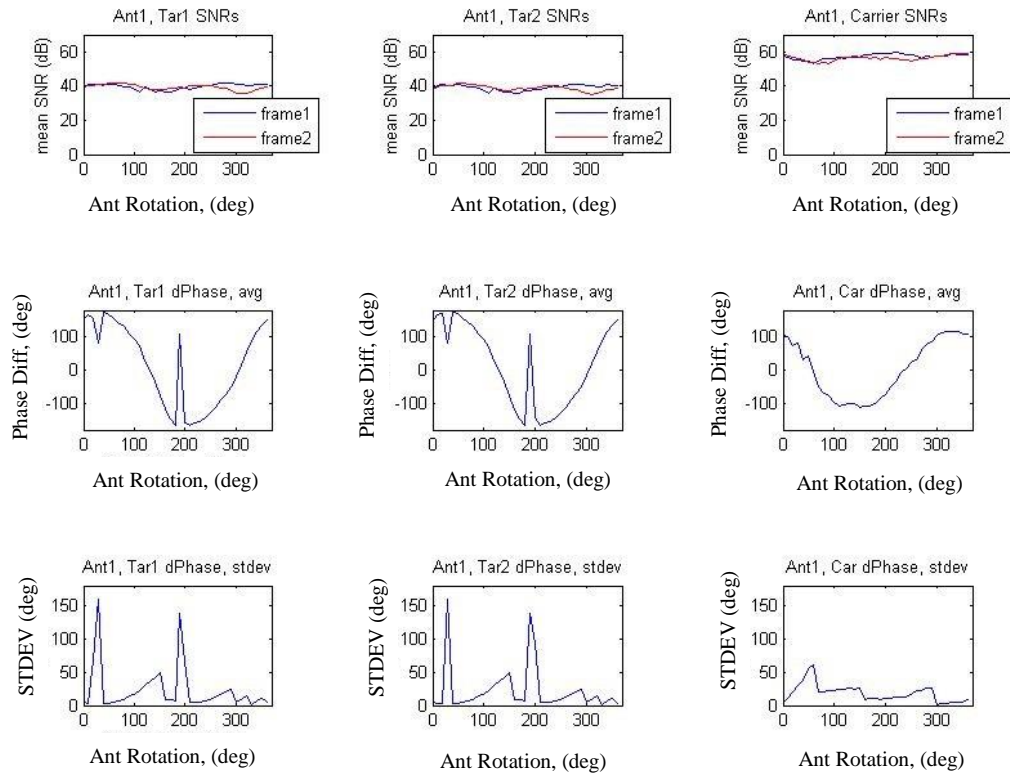


Figure 82: Azimuth calibration target phase difference measurement from antenna pairing 2 (Ant Sel 1). (Top row) Average SNR of targets 1, 2 and carrier vs RX antenna rotation. (Mid row) Average phase difference of the same target captured by the azimuth antenna pair. (Bot row) Standard deviation of the phase differences.

related to the AoA, it was decided that the proper method is to convert the measured phase difference to a measured AoA. This measured AoA was then fine-tuned by removing biases and adjusting the antenna-to-antenna spacing to fit the ideal AoA characteristic. The ideal AoA characteristics, was obtained from simulations which are discussed in section 5.3.2.

Elevation

The same procedure as the azimuth processing was performed for the elevation antenna pair. The elevation angular cuts were measured in 5° increments for up to $\pm 20^\circ$ antenna rotations and 10° increments out to $\pm 60^\circ$ antenna rotations. Once again, for each angular cut, at least 20

elevation radar updates (two radar images per update) were gathered and processed. The phases of identical targets in both radar images were subtracted to obtain phase difference. At each elevation angular cut, the SNR, and phase difference averages were calculated as well as the standard deviation of the phase difference. Figure 83 shows plots of the average SNR, average phase difference, and standard deviation as a function of the elevation antenna array rotation relative to the calibration beacon.

From figure 83 it can be seen that two instances of phase wrapping occurs within the $\pm 60^\circ$ rotation of the elevation antenna relative to the calibration beacon. This is caused by the

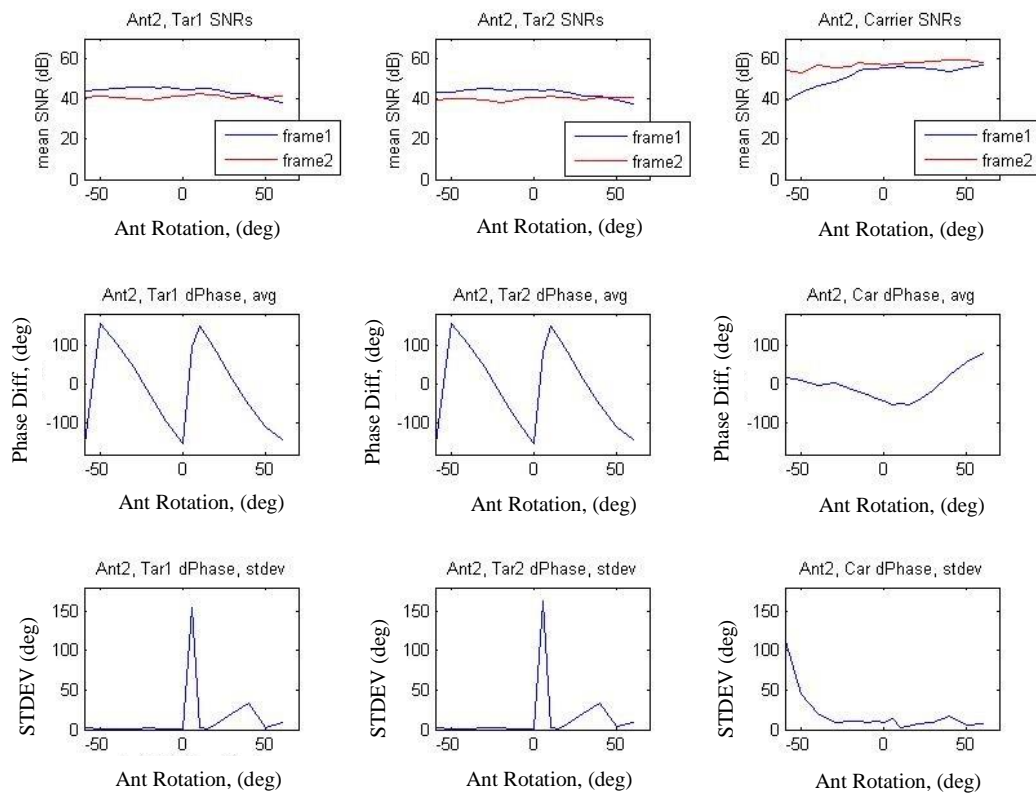


Figure 83: Elevation calibration target phase difference measurement from antenna pairing 3 (Ant Sel 2). (Top row) Average SNR of targets 1, 2 and carrier vs RX antenna rotation. (Mid row) Average phase difference of the same target captured by the elevation antenna pair. (Bot row) Standard deviation of the phase differences. Note that the angular rotation of the elevation antenna array only ranges from -60° to $+60^\circ$.

large spacing between the two elevation antenna elements which is estimated to be 13.5 cm while it should ideally be 6.34 cm (half-wavelength). However, since the radar specifications only called for target measurements within $\pm 15^\circ$ elevation field of view from the horizon, this can still be performed unambiguously using only RX antenna rotation data from $\pm 15^\circ$.

5.3.2 AoA simulations for miniature radar system

An AoA simulation was created specifically for the rev2 miniature radar system using parameters that were either physically measured or obtained from the datasheet. These simulated results are then compared against the measured AoA characteristics from the calibration beacon testing (section 5.3.3). The AoA simulation assumes that the azimuth RX antenna array is a perfect equilateral triangle with antenna-to-antenna baseline spacing of 53 mm. It was estimated that the elevation RX antenna array is separated by 130 mm using the COTS antennas datasheet, shown in figure 84.

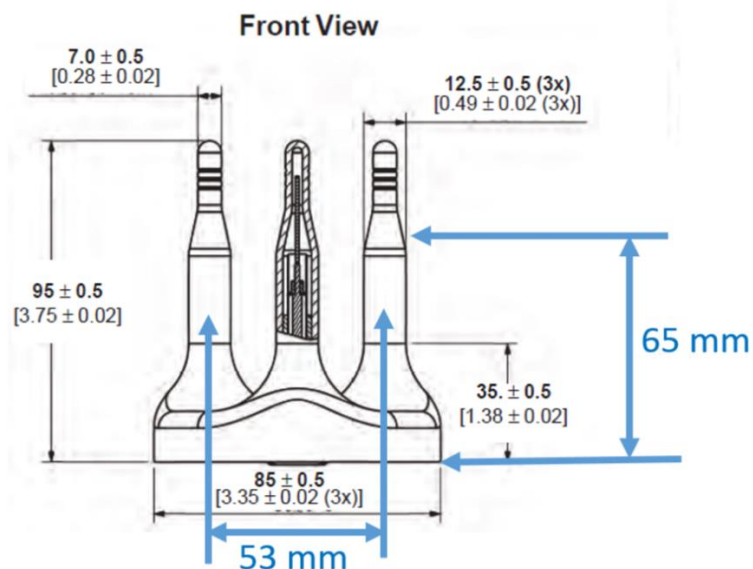


Figure 84: Estimated antenna spacing of the RX antenna array. The three azimuth antennas are assumed to be a perfect equilateral triangle. The elevation antenna spacing is assumed to be 130mm (2x 65 mm) since two antennas are attached end to end.

Figure 85 shows the azimuth AoA simulations performed in MATLAB. This simulation assumes that the radar system's azimuth antenna array is located in the center of a circle of targets with a 500 m radius (figure 85, top left). Given this geometry, the phase of each target detected by each of the antennas is limited between $+32^\circ$ and -152° . The phase difference amongst all three antennas are shown in figure 85 (bottom left) and spans $\pm 160^\circ$. Once these phase differences were applied to equation [3] (duplicated below) with the associated assumptions and converted into AoA, the AoA showed a perfect degree-to-degree mapping to the simulated circle of targets (figure 85, bottom right).

$$\theta_{AB} = \cos^{-1} \left(\frac{\lambda \delta_{AB}}{2\pi d} \right) \text{ [rad]} \quad [3]$$

Assumptions: δ_{AB} obtained from figure 85, bottom left, $d = 5.3$ cm, and $\lambda = 6.34$ cm

Recall that the simulation of figure 85 assumed the azimuth antenna array is perfectly centered amongst the circle of targets. The simulation was extended to account for the case where the RX array is offset from (0,0). This offset is highly plausible since it could not be guaranteed that during the calibration target measurements, the RX antenna was mounted over the exact center of the turn table. While simulations of the offset showed an impact on the magnitude of the phase measured by each antenna element, the phase difference and the resulting AoA was unaffected (see figure 86).

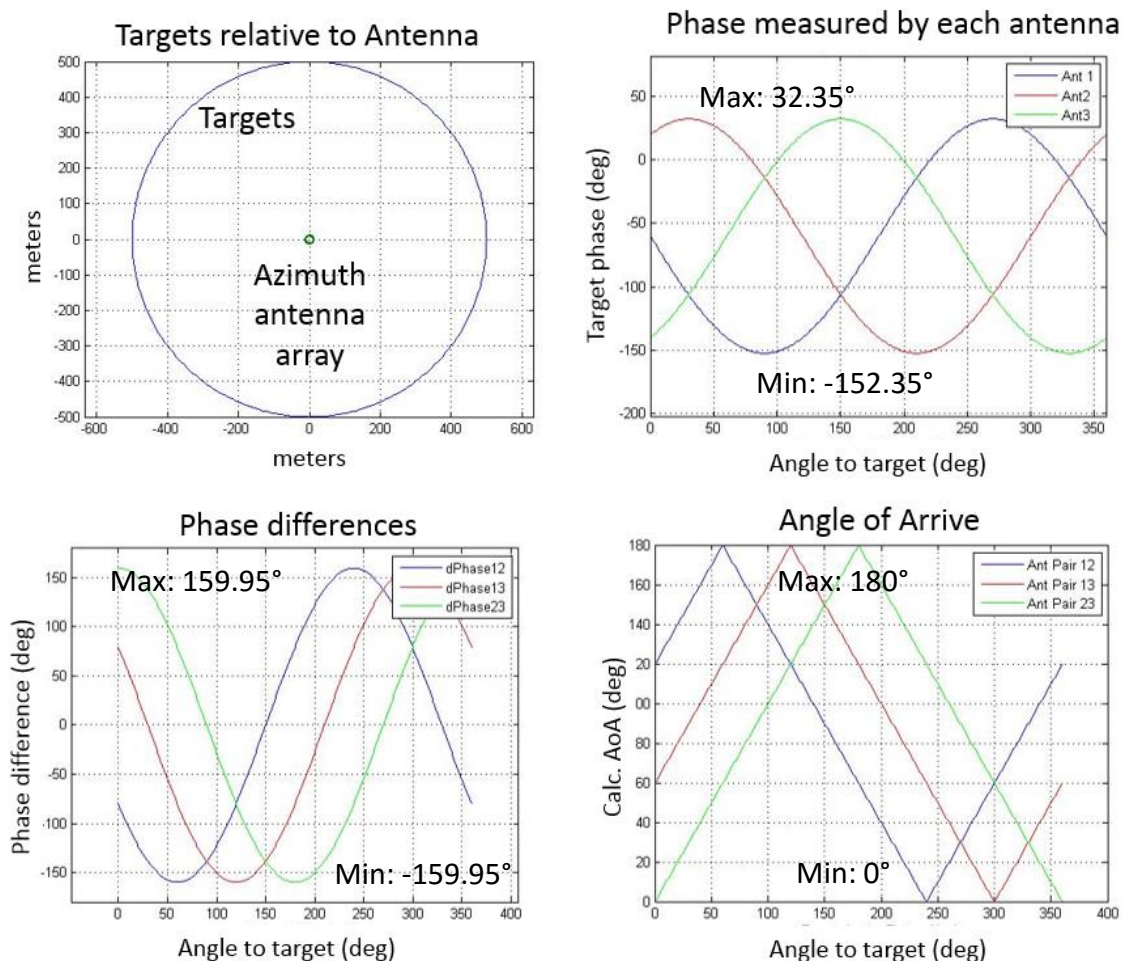


Figure 85: Phase, phase difference, and angle of arrival simulations. (top left) Simulation setup showing the targets located at a distance of 500 m away for the 3-element azimuth antenna centered at (0,0). (top right) The target phase measured by each antenna in the azimuth array. (bottom left) The phase difference between antenna elements. (bottom right) Phase differences converted to AoA using equation [3].

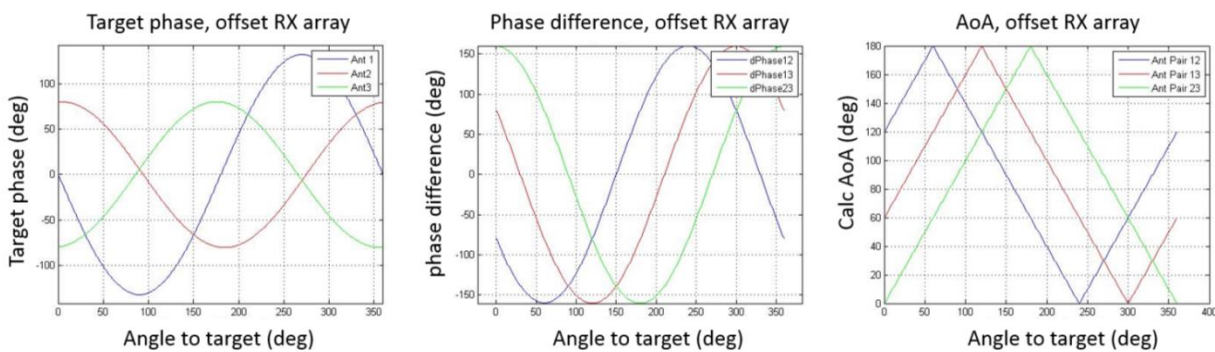


Figure 86: AoA simulation for scewed RX array. (left) Phase of targets measured by azimuth array. (middle) Phase differences of these targets. (right) Calculated AoA from phase differences.

Elevation

Elevation AoA simulations were not performed since this was not needed due to the already linear relationship between the measured phase difference and the antenna rotation in elevation. This is further discussed in section 5.3.3.

5.3.3 Phase difference to AoA conversion and fitting

The third process is to convert the measured phase differences shown in section 5.3.1 into AoA for the azimuth and elevation. This conversion process involves the physical parameters of the RX antenna array, primarily the antenna-to-antenna separation and biases in the radar system. The process described in this section used these degrees of freedom to not only convert the phase differences to an estimated AoA but also fitted the estimated AoA to the ideal AoA developed in the simulations in section 5.3.2.

Azimuth

To fit the measured azimuth AoA to the ideal AoA simulation, the phase difference data, shown in figures 81 and 82, must first be unwrapped. A custom unwrapping code was written which uses multiple previous values to determine if the current phase needed to be adjusted. Figure 87 shows two examples of the unwrapped phase differences, one from each antenna select pairing. A best fit sinusoid is also shown in each image from an early attempt at directly mapping phase difference to AoA. This earlier direct attempt however, failed to achieve a proper one to one mapping with low errors for the azimuth case.

Notice that there are several outliers around the peaks and troughs of the unwrapped phase difference data shown in figure 87. The phase difference is at a maximum or minimum when the calibration beacon is aligned with the baseline of the antenna pair; an end-fire situation.

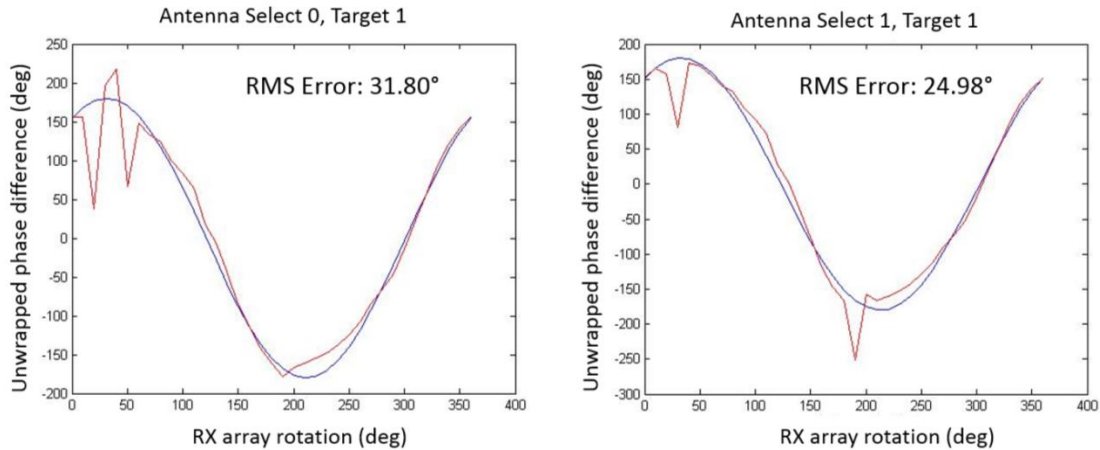


Figure 87: Two samples of unwrapped, calibration beacon, phase difference data over the entire 360° azimuth angular cuts. The RMS error shown is the error with respect to the best fit sinusoid, also shown in blue. This was a failed effort at interpreting AoA using only phase difference.

At these end-fire cases, the phase difference is located at the boundary of $\pm 180^\circ$ and noise in the data could cause the phase difference to toggle back and forth between positive and negative values creating a large standard deviation (over 100°) as seen in figures 81 and 82, bottom row. For the best AoA fit to the simulations, the phase difference values with greater than 100° standard deviation were ignored which removed the outlier data near the end-fire situations.

This can be done without introducing ambiguity to the azimuth AoA as long as there are no overlapping angles where data from both pairs are thrown away. Figure 88 shows the final matched calibration beacon AoA data to the AoA ideal simulations and table 13 lists the biases and the antenna baseline spacing (experimentally determined) that were applied to the calibration beacon data to obtain this best fit.

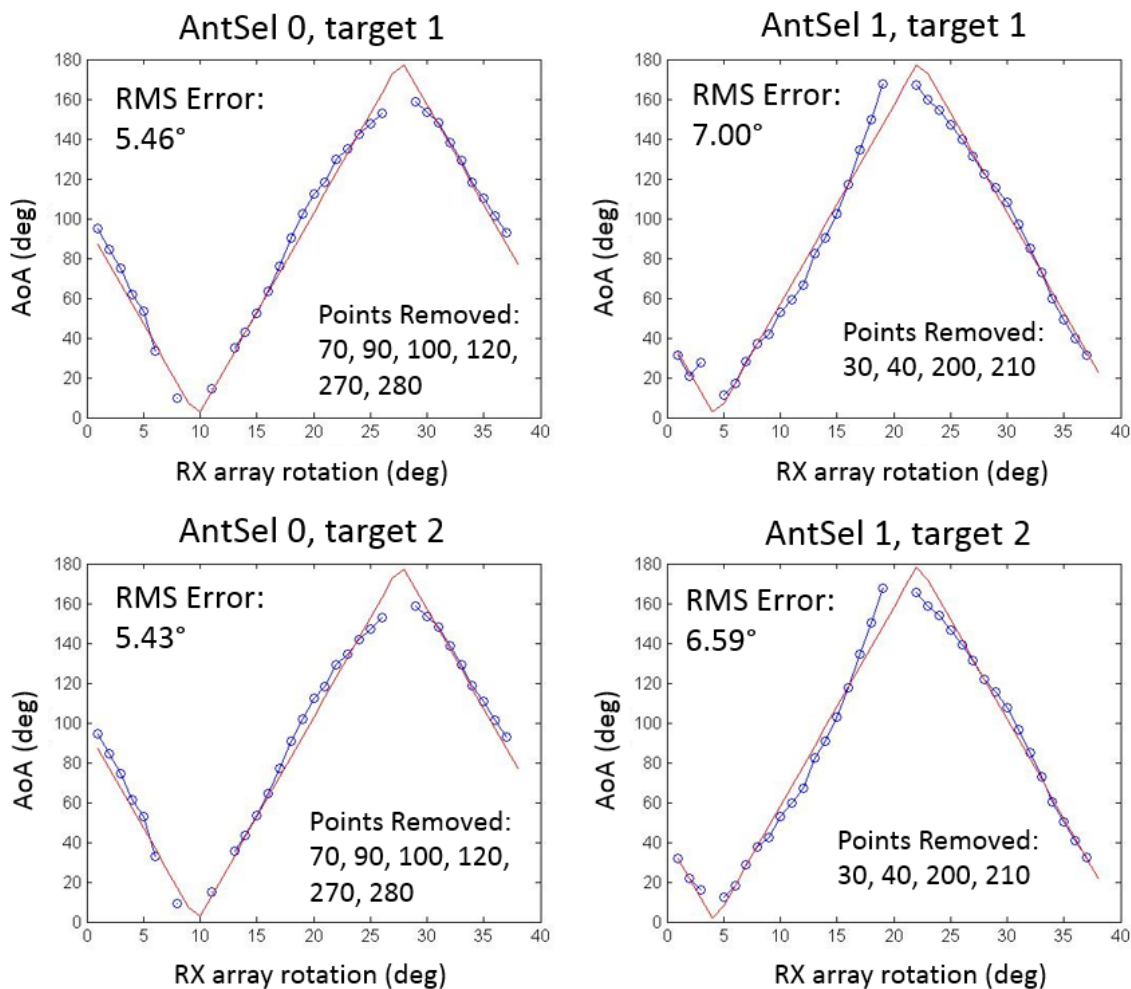


Figure 88: Calibration beacon AoA (blue) fitted to ideal AoA simulation (red). Phase biases and antenna-to-antenna baseline spacing were experimentally varied to obtain the optimal fit shown. End-fire situations resulting in significant phase difference standard deviations were removed.

Table 13: Calibration beacon data biases and adjustments for optimized AoA fitting

	AntSel 0, target 1	AntSel 0, target 2	AntSel 1, target 1	AntSel 1, target 2
RMS error of fit	5.46°	5.43°	7.00°	6.59°
RX rotation points removed (>100° std dev)	70°, 90°, 100°, 120°, 270°, 280°	70°, 90°, 100°, 120°, 270°, 280°	30°, 40°, 200°, 210°	30°, 40°, 200°, 210°
Phase difference bias	-24.3°	-24.3°	-13.15°	-13.15°
Ant-to-ant baseline	6.17 cm	6.17 cm	6.10 cm	6.13 cm
Average baseline*	6.17 cm		6.115 cm	

* Average baseline is used in car measurement data in section 5.34

** The chirp wavelength, λ , is assumed to be 6.34 cm

As mentioned earlier, the outlier data located at the end-fire situations can be removed without adding ambiguity so long as the gaps in coverage do not overlap between the two azimuth antenna pairings. Figure 89 is a graph of the coverage area provided by the two antenna pairings showing that the coverage gaps do not overlap and that meaningful data can be gathered by at least one antenna pairing for all 360° around the azimuth array. Also note that while the uncertainty in the phase difference is high at the end-fire situations, their sign (positive or negative) is still fairly consistent (see figure 87). This is enough data to resolve the ambiguity of which gap the target data falls in while using the other antenna pairing to obtain the precise phase difference and thus AoA information. Using this logic all target locations in 360° azimuth can be accounted for with just two pairs of azimuth antenna elements.

It is important to note that during the calibration beacon test, the RX antenna array was rotated clockwise. This is effectively the same as rotating the calibration beacon counter-clockwise around the radar system. This relationship needs to be accounted for when locating moving target relative to the radar's frame of reference.

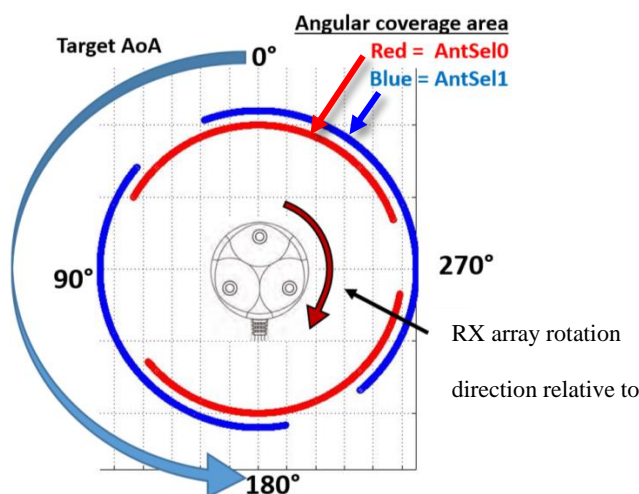


Figure 89: Angular coverage area of each azimuth antenna pair. Since the gaps in the coverage area do not overlap, the target AoA can be located unambiguously.

Using the values presented in table 13, the conversion of target phase data (captured by the radar) to azimuth AoA is performed by implementing the following steps.

1. Subtract the phase of a target in channel 2 from the same target in channel 1 (reference figure 48 and 51 for channel to RX antenna element mapping).
2. Depending on which azimuth antenna pairing the data was captured from (i.e. Antenna Select 0 or 1) add the associated bias listed in table 13 to the phase difference.
3. Convert the phase difference to AoA using equation [3] where λ is 6.34 cm and the antenna-to-antenna baseline spacing, d , is given by table 13.
4. Find this calculated AoA on the simulation values using interpolation and find the corresponding RX array rotations that creates this calculated AoA (there should be two possibilities).
5. Perform steps 1 – 4 for both azimuth antenna pairs (i.e. Antenna Select 0 and 1). There should only be one resulting RX array rotation that matches the data from both array pairings. Trace the RX array rotation value counter-clockwise to yield the azimuth AoA of the target.

Elevation

To convert the measured elevation differences to an elevation AoA, the data shown in figure 83 (middle row) was first be unwrapped. Figure 90 shows that the unwrapped elevation phase differences spanned over 600° for an RX antenna array rotation of only $\pm 60^\circ$ relative to the calibration beacon. This is again, the result of the elevation antenna-to-antenna baseline being greater than a half-wavelength. However, since the radar system specifications in table 1 calls for $\pm 15^\circ$ elevation coverage, only the phase difference from this view angle (i.e. RX

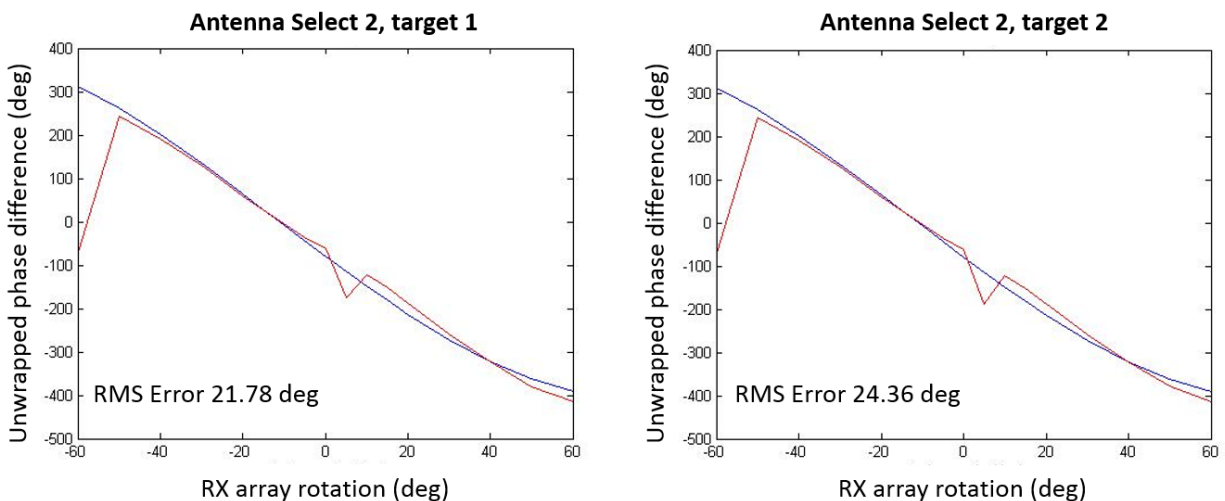


Figure 90: Unwrapped phase difference data for the entire $\pm 60^\circ$ elevation angular cut data using the calibration beacon setup. (red) The measured unwrapped target phase difference which spans over 600° . (blue) Best fit scaled sinusoid to the unwrapped phase difference and RMS error of the fit excluding the initial condition at -60° RX array rotation.

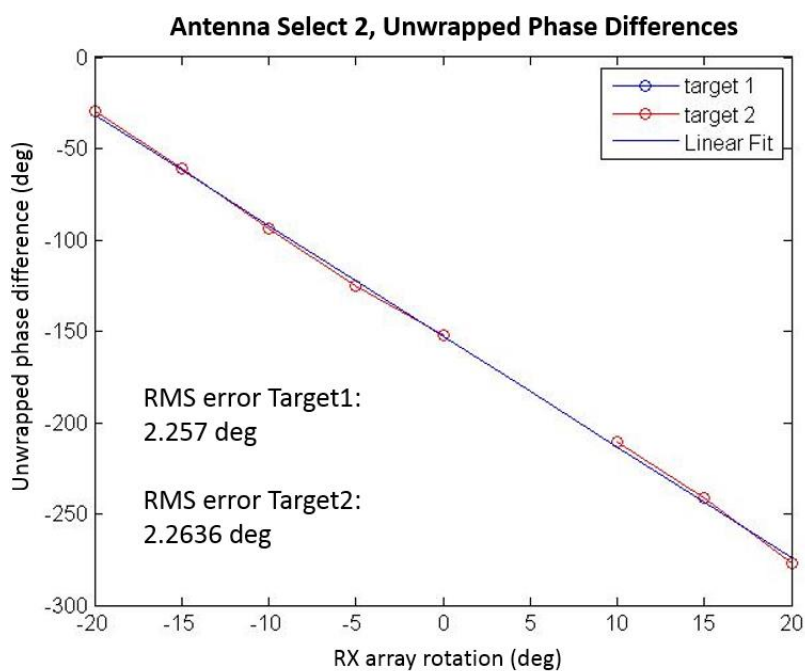


Figure 91: Unwrapped phase differences for only $\pm 20^\circ$ elevation angular cuts. (red) The unwrapped target phase differences spanning 242° . (blue) Linear line of best fit to the unwrapped phase difference. The RMS errors shows a close match after discarding the measurement at 5° RX array rotation which had a standard deviation greater than 100° .

antenna rotation of $\pm 15^\circ$) is necessary. For an added margin, the phase differences from $\pm 20^\circ$ RX array rotation was considered in this analysis. Figure 91 shows the unwrapped elevation phase information for this narrowed elevation field of view and the best linear fit to both targets.

It can be seen in figure 91, that a simple line of best fit is able to produce a RMS error of less than 2.3° for a direct phase difference to RX array rotation mapping. Furthermore, there are no ambiguities within this mapping. Therefore, rather than trying to remove biases and performing AoA conversions, it was decided that this linear relationship expressed in equation [7] was sufficient for target elevation AoA estimation. Note that the elevation antenna array's orientation relative to the calibration beacon and direction of positive rotation is shown in figure 72. Similar to the azimuth antenna array, the target AoA is in the opposite direction of the RX array rotation.

$$RX \text{ array rotation} = -0.165(\text{Phase difference}) - 25.2 \quad [7]$$

5.3.4 Car measurement AoA

The described range-Doppler and AoA analysis was performed for the series of car measurement data shown in figure 80, specifically for the approaching car whose CFAR detected peaks are circled in red. The phase information from three consecutive radar updates (i.e. Antenna Select 0, 1, and 2) were combined to form an azimuth and elevation estimation of the car's location. It was assumed that the AoA of the car would not change significantly between updates given the geometry of the setup (approaching car near boresight), the speed of the car, and the stationary radar system. Table 14 summarizes the first 18 radar updates combined into 6 total AoA updates. Figure 92 is a graphical summary of the car data set showing range, Doppler, and AoA. Note that the RMS error in the azimuth AoA estimations causes target location to

Table 14: Measured car range, Doppler, and AoA

Radar Update Index	Range per update (m)	Average Doppler (m/s)	Azimuth AoA Ant Sel 0 (deg)	Azimuth AoA Ant Sel 1 (deg)	Average Azimuth AoA (deg)	Elevation AoA (deg)
1,2,3	452, 444, 437	-12.47	N/A	3.47	3.47	-1.86
4,5,6	429, 421, 413	-12.63	-2.23	4.80	1.29	-2.46
7,8,9	405, 397, 389	-13.61	-5.98	2.53	-1.725	-3.12
10,11,12	381, 373, 365	-14.59	-5.82	12.70	3.44	-2.49
13,14,15	357, 341, 333	-14.92	4.48	14.01	9.25	-2.62
16,17,18	325, 310, 294	-14.92	-0.94	-9.94	-5.44	-3.25

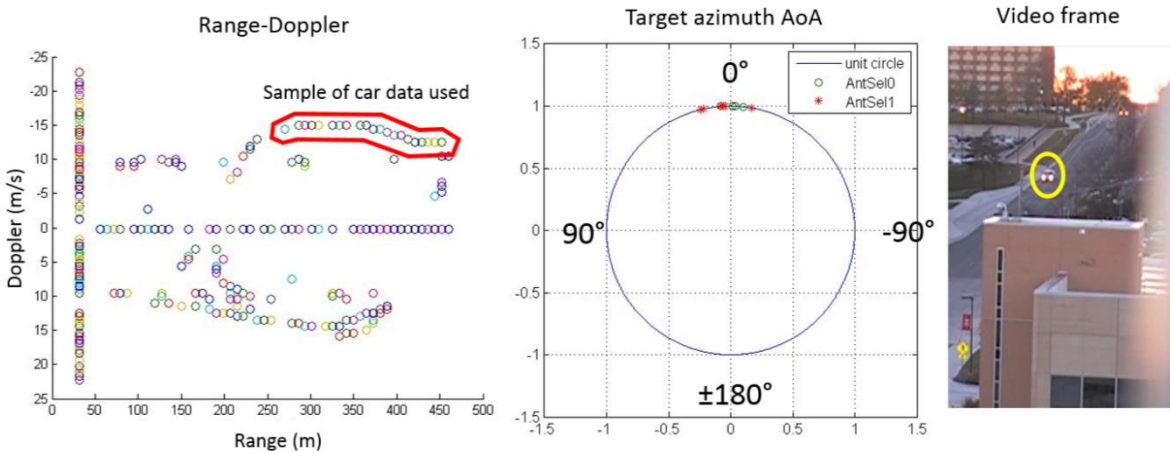


Figure 92: (left) Range-Doppler plot of the car target from table 14. (middle) Azimuth AoA plot of the car target on a unit circle showing the measured angles from both azimuth antenna pairs. (right) Sample image of the approaching car from video captured simultaneously with the radar data.

fluctuate beyond the original $\pm 3^\circ$ specification but the elevation AoA performs significantly better.

5.4 Target tracking and 6-DOF estimation

The last piece of radar performance analysis focuses on the ability to perform target tracking as well as estimation of the target's 6 degrees of freedom (6-DOF); XYZ position and XYZ velocity relative to the radar. The target tracking capability is to provide the flight director

with a sense of where the target will appear on the next radar update, a confidence level in the target, and filtering of anomalous echoes. The target 6-DOF is to provide a real sense of the target location in 3-D space as well as its true heading in addition to just the radial velocity (i.e. Doppler).

5.4.1 Target tracking

Target tracking was performed using the range-Doppler relationship of detected targets in a 2-D FFT radar image. Assuming the Doppler of a target changes slowly compared to the radar update rate, it is possible to estimate the new location of the target in range-Doppler given the time between updates and the radial velocity. The new location was estimated as a 3 x 5 (range x Doppler) block in the radar image centered on the predicted target location. If a target was detected in this block, the confidence in the target is incremented by 1 and so is the confidence of future prediction zone of the target. If the target fails to appear in the next prediction zone, its confidence level drops. Using this method of tracking targets in range and Doppler, the targets that meet a certain confidence level threshold can be reported to a flight director or autopilot. Note however that this means a target must be consecutively detected and accurately predicted to eventually meet this threshold. Furthermore, this process filters out anomalies and/or is able to assign them less confidence since these anomalies do not follow the range-Doppler relationship.

Figure 93 shows samples of this tracking method from the car measurement dataset taken at intervals of five radar updates. The first column of figure 93 shows an angled view of the detected targets in range and Doppler for updates 1, 5, 10, and 15. The height of the target indicates the confidence level in the tracked target based on the number of times the target has appeared in the predicted range-Doppler block. The second column of figure 93 is a top down view of the same target to more easily observe the target migration through range and Doppler.

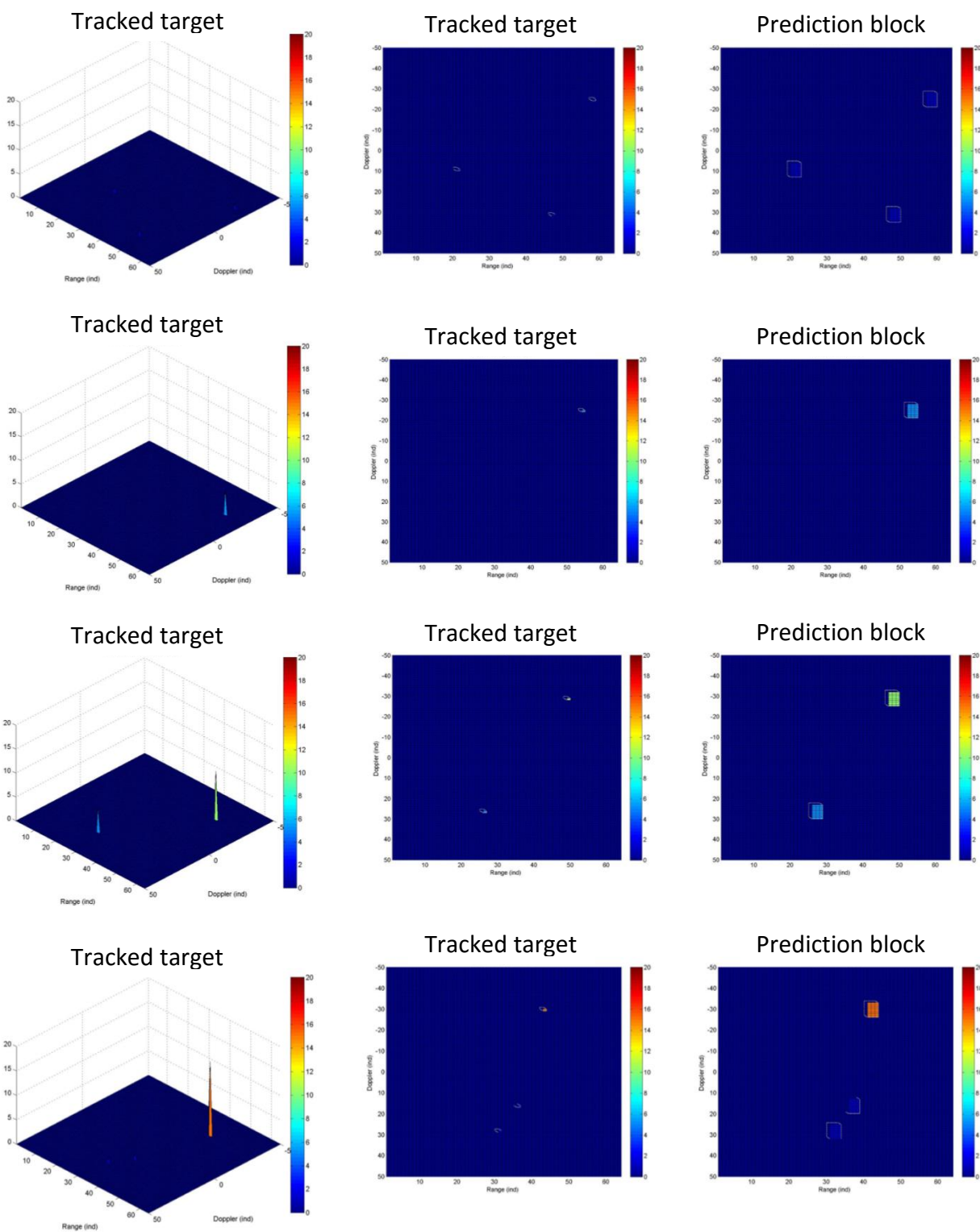


Figure 93: (left column) Detected target in range-Doppler where the height of the target corresponds to the confidence level. (middle column) Top-down view of detected target in range and Doppler. (right column) Predictions in range and Doppler of where each target should appear in the next radar update. As detected target locations match the predictions, the confidence level (height) of the target grows.

The third column shows the predicted range-Doppler blocks based on the current target location and confidence level. It can be seen that as the target is successfully detected in consecutive updates, both the target (figure 93, column 1&2) and the prediction blocks (figure 93, column 3) grows in confidence. The threshold for a successfully detected and tracked target to be reported to the flight director may be set to any value and could be a variable depending on the environment and/or additional supporting sensors.

5.4.2 Six degrees of freedom (6-DOF) estimation

The target six degrees of freedom (6-DOF) information is the true target location in X, Y, and Z as well as its velocity in X, Y and Z relative to the radar system. This information can be obtained using target range and AoA information. However, it was discovered that the root mean square error (RMSE) of the target AoA significantly affected the ability to reliably extrapolate this information. The following is a description of the target 6-DOF analysis.

Azimuth

The azimuth location and velocities analysis began with an estimation of the target's true location relative to the radar RX antenna array. Using the image of the scene it was estimated that the approaching car that was successfully detected and tracked in figure 93 began with an azimuth AoA of -3° and over the course of 18 radar updates ended at 0° (shown in figure 94). Comparatively, the "Average Azimuth AoA" of the detected car shown in table 14, is generally in the correct direction but fluctuates between positive and negative which is attributed to the AoA RMSE. Note that the data in table 14 was gathered at the rev2 miniature radar's 2-Hz update rate. It was proposed that the instability of the measured data can be reduced if additional radar updates could have been gathered at the ideal 10-Hz radar update rate and averaged. This was tested using interpolation on the measured data set.

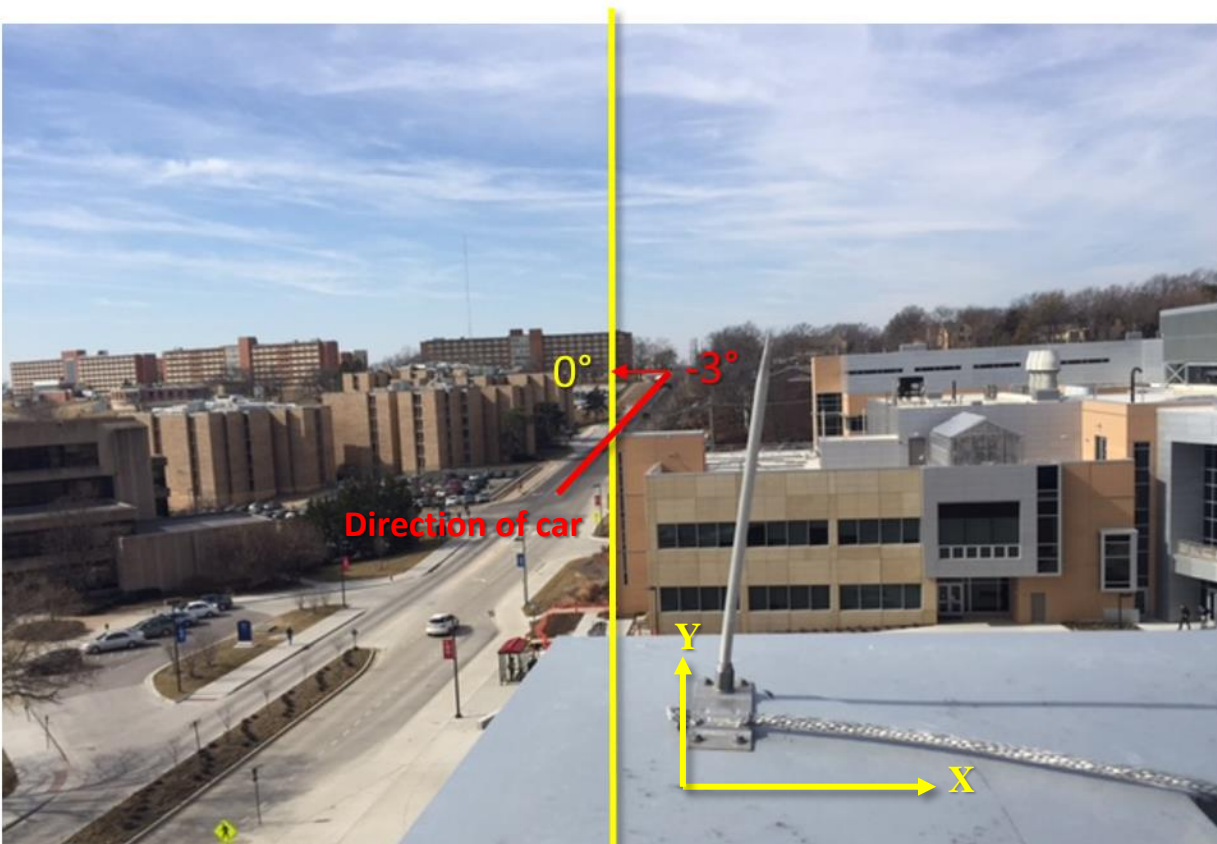


Figure 94: Estimation of the azimuth AoA of the approaching car in the data shown in table 14. The car should begin at approximately -3° and move towards 0° azimuth AoA over the course of 18 radar updates.

The 18 measurement samples shown in table 14 were interpolated to 126 samples which represents a 10-Hz radar update rate. This interpolation was also performed for the estimated ideal AoA data which was then paired with the range data to yield the expected XY location as a function of time shown in figure 95 (left). Note that the car is estimated to travel in the negative X-axis direction and negative Y- axis direction in both figure 95 (left) and the scene in figure 94.

The interpolation of the azimuth AoA measured data had a 6° RMSE built into the interpolated values since this was the best fit of the calibration beacon measurements to the expected AoA (figure 88). From here the measured AoA was paired with the same measured range data as the ideal setup and converted to XY locations relative to the radar system. A 25

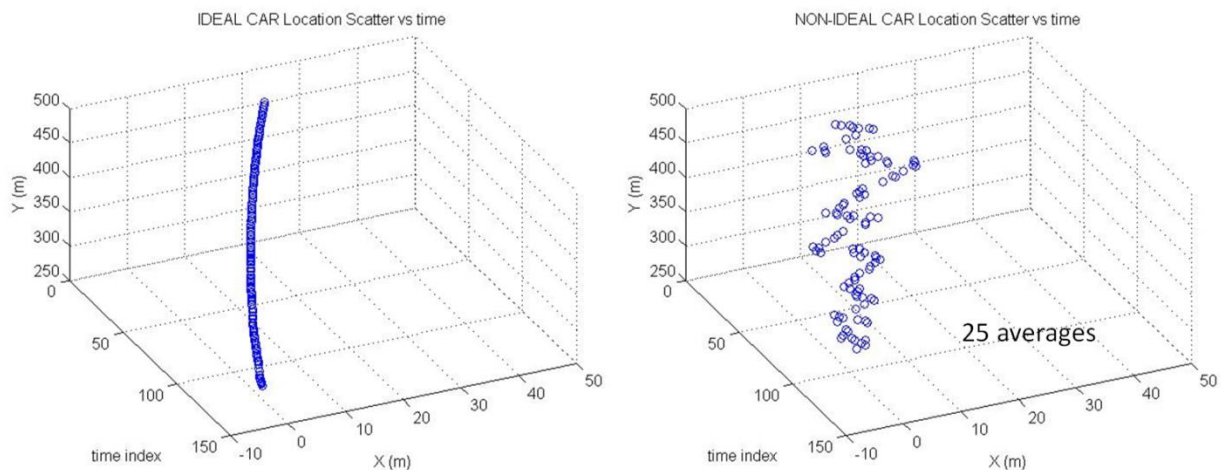


Figure 95: (left) Ideal car location in XY azimuth plane per time index. XY location is calculated from the estimated car movement in figure 94. (right) Interpolated azimuth car data from the measured locations using 25 averages per sample.

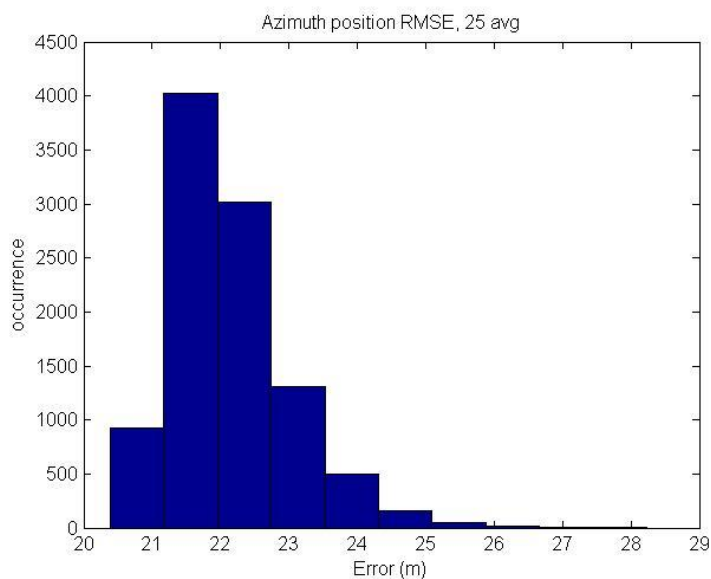


Figure 96: Interpolated data histogram of the measured XY location error (expressed as RMS range) from the estimated ideal XY location of the car.

sample moving window averaging function was applied to the XY locations to try and reduce the error of the measured XY location from the ideal XY location. Figure 95 (right) shows one sample of the interpolated measured XY locations vs time. A histogram of 10,000 measured

azimuth AoA interpolations was created showing that the resulting XY location data error as a RMSE distance away from the estimated ideal case (figure 96).

The azimuth X and Y velocities also contain a significant amount of error since these values are extrapolated from the difference in XY locations between consecutive updates. Figures 97 and 98 shows the X and Y velocities respectively for a single interpolation sample. The instantaneous velocity between consecutive radar updates are plotted as a stem plot. The average velocity across the entire data set however, is shown as a red bar. It can be seen that while the instantaneous velocities fluctuates for both X and Y, the average X direction velocity is -1.5 m/s and the average Y direction velocity is -15.1 m/s meaning on average, the car target in the scene (figure 94) is moving slightly left, and down the hill towards the radar.

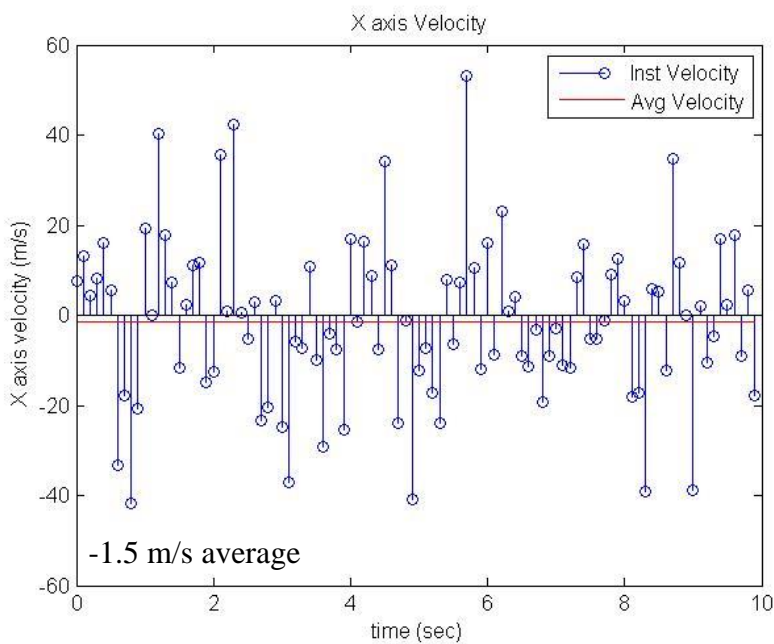


Figure 97: X-axis velocity from interpolated measured car data.

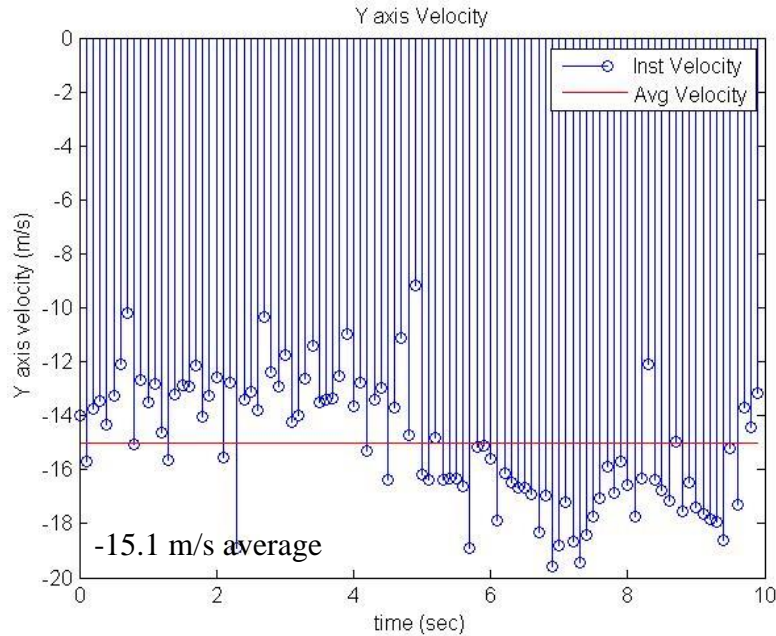


Figure 98: Y-axis velocity from interpolated measured car data.

Elevation

The elevation 6-DOF analysis also began with an estimation of the setup and ideal behavior of the approaching car from Table 14. Figure 99 shows the estimated setup where the top of the hill, in the far edge of the scene in figure 94, is assumed to be the same height as the radar system on the roof of the building. Inspections of the purely measured elevation AoA data shown in table 14 indicates that while some fluctuations may occur, in general, the measured car is moving in the negative Z axis direction (i.e. down hill).

Similar to the azimuth AoA analysis, the elevation AoA from the estimation of the scene (ideal) and measured data were interpolated to represent the radar sampling at a 10-Hz update rate. The estimated ideal elevation AoA was paired with the measured ranges to the car to create the ideal Z-axis location relative to the radar system shown in figure 100 (left). The interpolations of the measured elevation AoA data had a 2.26° RMSE built into the interpolated

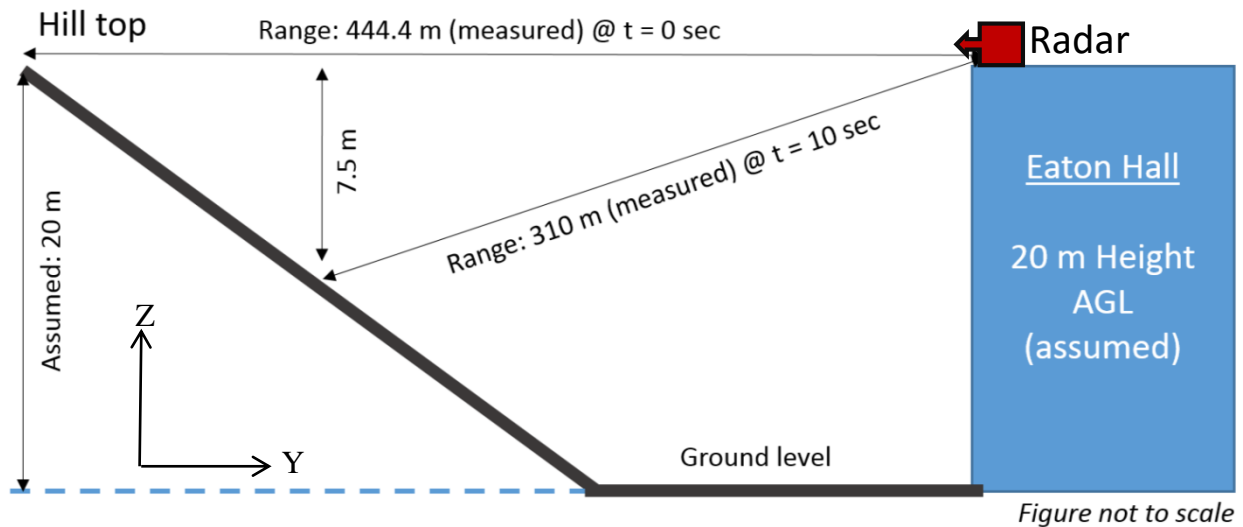


Figure 99: Estimation of the elevation parameters of the car measurement scene.

values since this was the best elevation AoA fit that could be achieved during calibration (figure 91). A 25 sample moving window averaging function was applied to the Z-axis locations to try and reduce the fluctuation errors. Figure 100 (right) shows a sample of one of the interpolated measured Z-axis locations vs time plots. A histogram of 10,000 measured elevation AoA interpolations was created showing that the resulting Z location data error as a RMSE distance away from the estimated ideal case.

The elevation velocity also contained errors since the values were extrapolated from the difference in Z-axis locations between consecutive updates. Figure 102 shows the Z-axis velocity for a single interpolation sample. The instantaneous velocity between consecutive radar updates are plotted as a stem plot. The average velocity across the entire data set however, is shown as a red bar with a value of -0.96 m/s. Therefore, while the instantaneous elevation velocity does fluctuate, on the average, the target car in the scene is decreasing in altitude at a rate of 1m/s.

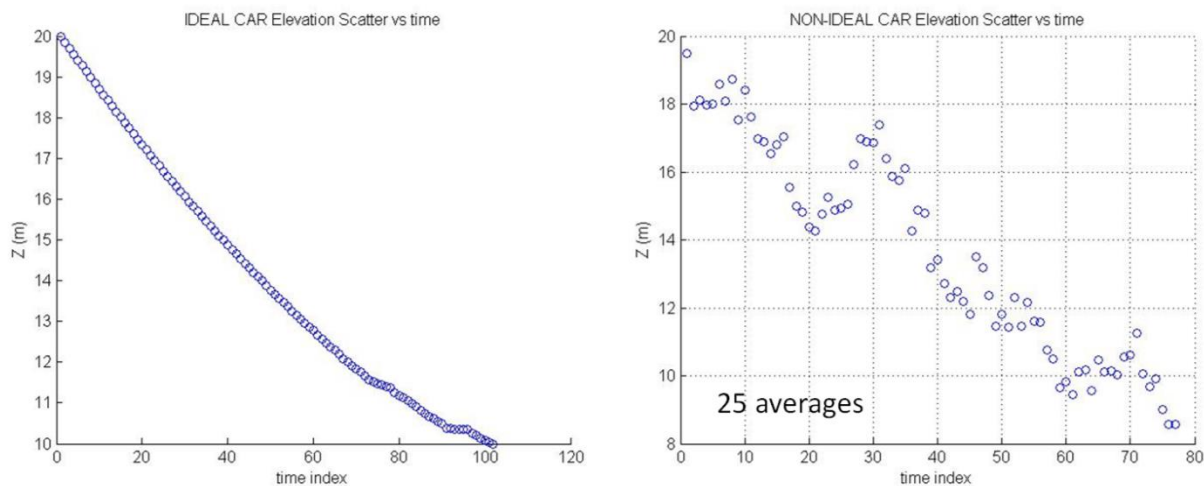


Figure 100: (left) Ideal car location in Z elevation plane per time index. Z location was calculated from the assumed setup in figure 99. (right) Interpolated elevation car data from the measured locations using 25 averages per sample.

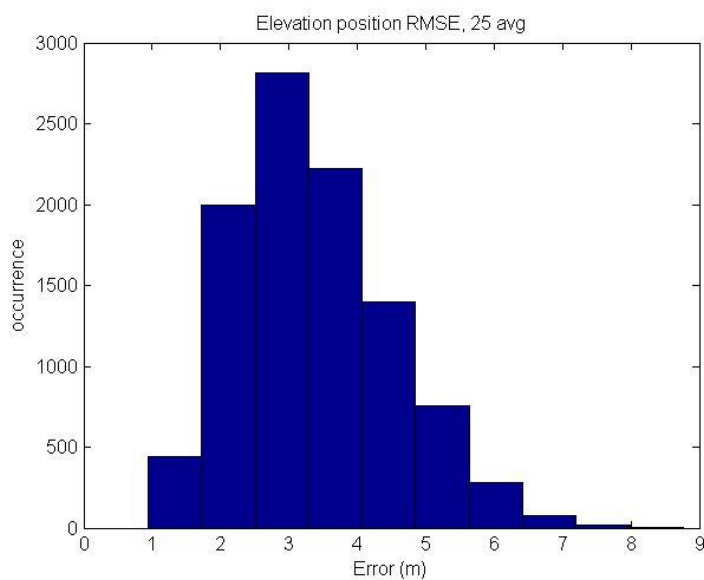


Figure 101: Interpolated data histogram of the measured Z location error (expressed as RMS range) from the estimated ideal location of the car.

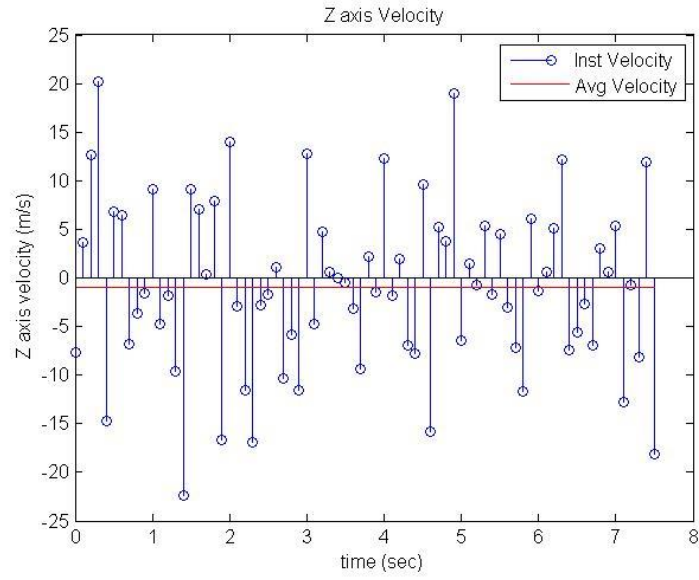


Figure 102: Z-axis velocity from interpolated measured car data.

Chapter 6: Conclusion and continuing work

6.1 Conclusion

The design of a multichannel, collision avoidance, FMCW radar that is capable of detecting targets in range and Doppler using a 2-D FFT processing method has been validated in laboratory and environmental testing. Hardware limitations primarily in the form data memory and transfer rates have limited the radar system to only two active receive channels per update at a 1.7-Hz update rate when ideally the radar should possess at least four active receive channels at a 10-Hz update rate. The miniaturization of the brassboard radar system into a size, weight, and power form factor that is capable of being installed on a 40% Yak-54 UAS was successfully completed with the exception of the unforeseen external transmit power amplifier. This amplifier as well as the memory and data rate issues will be addressed in continuing work.

Algorithms for target detection using CFAR were successfully demonstrated on both laboratory testing as well as environmental testing against moving cars. Using the rev2 miniature radar system which has the ability to toggle between receiving antenna pairs, the angle of arrival of the cars were obtained after calibration. Though the AoA point in the correct direction, the RMSE in the AoA estimations (obtained through calibration) of the instantaneous calculation of the target's 6-degree of freedom less accurate than desired. Interpolations using the measured data showed that averaging the target AoA data does help reduce the 6-DOF error and could be performed once the radar is properly functioning at maximum speed. The following section will address continuing work on improving the radar system capabilities.

6.2 Continuing work

Continuing work on the radar system is being performed through NASA LEARN II as well as by UAVradars LLC, a KU technology spinout company founded on this radar technology. The scope of the immediate continuing work for enhancing the radar system to meet the ideal performance requirements in table 1 are:

1. The FPGA memory needs to be increased such that the 2-D FFT and ping pong architecture can be performed within the available memory so as not to lose radar data during data transfer. This can be performed by obtaining a larger FPGA, though the more practical method is to switch FPGA evaluation boards to one with easily accessible off chip RAM.
2. The data transfer rates needs to be enhanced to meet the 10-Hz update rate requirement. The use of Ethernet instead of USB is being explored for this purpose though NASA LEARN II.
3. To fully meet the 10-Hz update rate requirement, the waveform generator needs to be adjusted or replaced with an alternative, such as a direct digital synthesizer (DDS), to remove the 50- μ s delay between consecutive transmits to wait for transients to settle.
4. The external TX power amplifier needs to be replaced with a smaller SWaP component. Currently the power amplifier investigated by Michael Blecha is intended to be the replacement but requires integrated testing with the radar system. [ref 13]
5. With the upgraded data capture capability, the interpolated AoA analysis described in section 5.4.2 can and should be experimentally validated.

Continuing research is currently being performed in NASA LEARN II on using a Tegra K1 as a system of systems integration (figure 103). The Tegra K1 is proposed to perform the radar

processing (i.e. finishing the 2-D FFT, CFAR, target tracking, and AoA analysis) using its GPU capability and also contain the AE department's custom flight director/autopilot as well as sensor integration with a camera onboard the same sUAS. This research is heading towards the autonomous collision avoidance sUAS that is capable of utilizing the collision avoidance radar data as well as allowing the radar data to enhance other sensors that could ultimately make up the collision avoidance sensor suite.

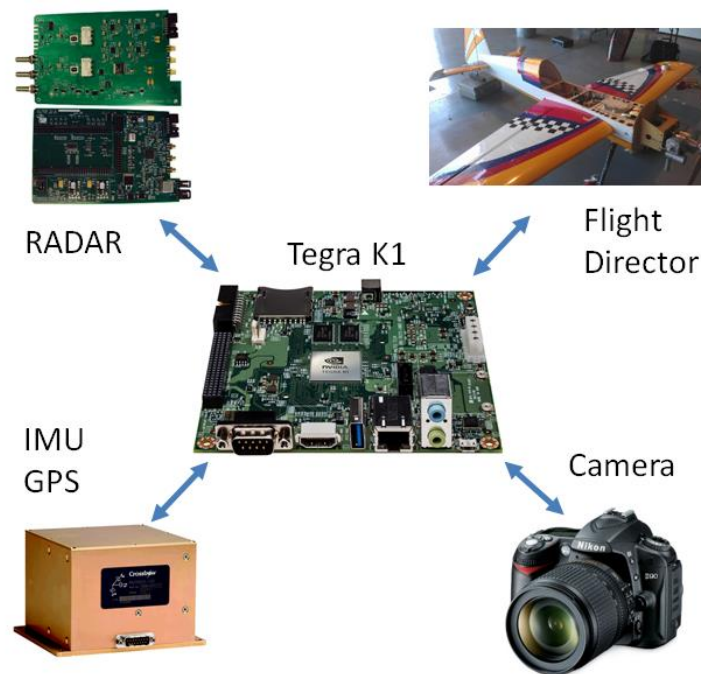


Figure 103: Tegra K1 serving as a system of systems integration hub for the collision avoidance radar along with the flight director, autopilot, and camera detection sensor onboard the 40% Yak-54 UAS.

Since the rev3 miniature radar operating frequency is migrating into the 2.4-2.5 GHz ISM band, the interference with WiFi, cellphones, and even the sUAS remote control needed to be investigated. It has been proposed that the radar system needs to have cognitive capabilities and monitor its surroundings for interference. Note that this also includes interference for a second

collision avoidance radar system for the case where two sUAS each carrying a radar system are flying near each other. Lastly, the NASA LEARN II effort will investigate range dependent update rate and target sensitivity where closer targets are reported more often since they require less coherent processing due to lower signal propagation loss.

References

- [1] Pope, Stephen. "FAA Investigating Reported UAV Collision with Piper Twin." *Flying*. 1 September 2015. Web. Accessed: 19, April, 2016.
<http://www.flyingmag.com/technique/accidents/faa-investigating-reported-uav-collision-piper-twin>
- [2] "UAV Transponders & Tracker Kits." *Unmanned Systems Technology*. Echoblu Ltd. Web. Accessed: 19, April, 2016.
<http://www.unmannedsystemstechnology.com/company/sagetech-corporation/>
- [3] Crowe, Steve. "Watch: MIT Drone Autonomously Avoids Obstacles at 30 MPH." *Robotic Trends*. 6 November 2015. Web. Accessed: 19 April 2016.
http://www.robotictrends.com/article/watch_mit_drone_autonomously_avoids_obstacles_at_30_mph
- [4] Contarino, Mark and Scire Consultants, LLC. "Report. Task 3.1 – Review and Analysis of Available System Technology Options and Justification for System Selection." All Weather Sense and Avoid System for UASs. 5 December 2009.
- [5] Marshal, Patrick. "Miniature radar may put UAVs in the air". *GCN*. 24 June 2014. Web. Accessed: 15 December 2015. <https://gcn.com/blogs/emerging-tech/2014/06/uav-radar-sense-and-avoid.aspx>

- [6] “World’s Lightest UAV LiDAR Utilises Ellipse-E Miniature INS.” *Unmanned Systems Technology*. Echoblue Ltd. Web. Accessed: 10 December 2015.
http://www.unmannedsystemstechnology.com/2015/09/worlds-lightest-uav-lidar-utilises-ellipse-e-miniature-ins/?utm_source=Unmanned+Systems+Technology+Newsletter&utm_campaign=be870baf1d-Unmanned_Systems_Technology_eBrief&utm_medium=email&utm_term=0_6fc3c01e8d-be870baf1d-106366497
- [7] Zakharov, Mikhail. “Designing a Multichannel Sense-and-Avoid Radar for Small UASs,” Information & Telecommunication Technology Center, KU, Lawrence, KS, 2014.
[Document](#).
- [8] J. F. Florencio Neto. “Receiver Antenna Array for Multichannel Sense-and-Avoid Radar for Small UAVs,” ITTC Technical Report 70093-01, Information & Telecommunication Technology Center, KU, Lawrence, KS, 2013. [Document](#).
- [9] Niakan, Nahal. Personal interview. 27 February 2013.
- [10] “Integration of Civil Unmanned Aircraft Systems (UAS) in the National Airspace System (NAS) Roadmap,” U.S. Department of Transportation Federal Aviation Administration. First Edition-2013. [Document](#).

- [11] “Integration of Unmanned Aircraft into the National Airspace System,” Carnegie Mellon University, May 1, 2007.
- [12] Stastny TJ; Garcia G; Keshmiri S; “Collision and Obstacle Avoidance in Unmanned Aerial Systems Using Morphing Potential Field Navigation and Nonlinear Model Predictive Control,” *ASME Journal of Dynamic Systems, Measurement and Control*, Under Review, July 2013.
- [13] Blecha, Michael . “Implementation of a 2.45 GHz Power Amplifier for use in Collision Avoidance Radar,” Information & Telecommunication Technology Center, KU, Lawrence, KS, 2016.
- [14] Al-Jazzar, Saleh O, et all. “Low Complexity and High Accuracy Angle of Arrival Estimation using Eigenvalue Decomposition with Extension to 2D AOA and Power Estimation,” *EURASIP Journal on Wireless Communications and Networking*. 2011.
- [15] “Agilent Fundamentals of RF and Microwave Noise Figure Measurements,” Agilent Technologies. Application Note 57-1. August 5, 2010.
- [16] Accardo, Domenico, et all. “Flight Test of Radar-Based Tracking System for UAS Sense and Avoid,” *IEEE Transactions on Aerospace and Electronic Systems*. Vol. 49. No. 2 April 2013.

Appendix

A.1 Rev2 Miniature Radar RF Chain

Table 15: Rev2 miniature radar noise figure calculation chart

	1	2	3	4	5	6	7	8	9
	Ext. Board	LNA	RF switch	SAW filter	Amp	Mixer	LPF	IF amp1	IF amp2
Gain (dB)	-3	11.5	-1.5	-1	13.3	-5.6	-0.2	35	35
Gain (linear)	0.50	14.13	0.71	0.79	21.38	0.28	0.95	3162	3162
F (dB)	3	1.7	1.5	1	1	5.6	0.2	12	12
F (linear)	2.00	1.48	1.41	1.26	1.26	3.63	1.05	15.85	15.85

$$\text{Noise Figure} = F_1 + \frac{F_2-1}{G_1} + \frac{F_3-1}{G_1 G_2} + \frac{F_4-1}{G_1 G_2 G_3} + \dots + \frac{F_9-1}{G_1 G_2 G_3 G_4 G_5 G_6 G_7 G_8} \quad [8]$$

The noise figure of the rev2 miniature radar was calculated from table 15 and equation 8 where $F_{\#}$ and $G_{\#}$ is the F (linear) and Gain (linear) in corresponding column number. The calculated noise figure is 3.82 (linear) or 5.82 dB.

A.2 Detailed 2-D FFT simulation

```

% Loopback Simulation
% Jan-2014
% Simulate the UAV radar loopback results

clear all;
close all;
clc;

% SEEDING randn
s = RandStream('mrg32k3a');
RandStream.setDefaultStream(s);
savedState = s.State;

```

```

%CONSTANTS
c = 3e8;           % free-space light speed (m/s)
K = 1.38e-23;     % Boltzmann's constant (J/K)

% SYSTEM-LEVEL PARAMETERS
To = 290;         % system temperature (K)
F = 3.5;          % Rx noise figure (dB)

fc = 1445e6;      % radar center frequency (Hz)
B = 15.7e6;       % signal bandwidth (Hz)
f1 = fc - B/2;    % radar start frequency (Hz)
lambda = c/fc;    % wavelength (m)

subT = 0.2e-3;    % waveform duration (s)
k = B/subT;       % Tx signal chirp rate (Hz/s)
T_pause = 54e-6;  % pause duration between chirps (s)

% RF NOISE AND LEAKAGE POWER & FREQUENCY LEVELS
% Tx signal power (dBm)
Tx_power = 27;
% Tx-to-Rx antenna coupling (dB)
Tx_Rx_coupling = -39;
% Tx-to-Rx leakage power (dBm)
leakage_power = Tx_power + Tx_Rx_coupling;
% leakage path length (m)
leakage_path_length = 5;
% leakage path delay (s)
leakage_path_delay = leakage_path_length/c;
% leakage beat freq (Hz)
leakage_freq = k*leakage_path_delay;
% Rx noise power (dBm)
noise_power = 10*log10(K*To*B)+30;

% SIGNAL PROCESSING INFO
f_s = 4e6;        % sample freq (Hz)
Bvideo = 1e6;     % anti-aliasing filter BW (Hz)
dt = 1/f_s;       % sample period (s)
M = 512;          % number of slow time sampled waveforms
Tt = M*(subT+T_pause);

t = 0:dt:subT;    % waveform time index (s)
t_ext = -200*dt:dt:subT; % waveform time index (s)
n = length(t);    % time vector length (samples)

% TARGET SIGNAL FREQUENCIES
v_max = 2*36;     % max UAV to UAV radial velocity (m/s)
v = 50;           % Radial velocity (m/s)

```

```

R = 584; % Range (m) - same as loopback setup
Rx_signal_power = -124.5;
Rx_signal_freq = 2*R/c*k; % signal beat freq (Hz)

% DIGITAL QUANTIZATION PARAMETERS
% note: given -17 dBm input saturates the 12 bit ADC
% Vp is max peak sinusoid voltage input into ADC
Vp = 10^((-17-10)/20);
Vpp = 2*Vp; % Vpp max sinusoid input into ADC
Quant_steps = 2^12; % number of quantization steps
% amount of voltage change required for an
% quantization increment
V_per_Q = Vpp/Quant_steps;
DC_bias = Vp;

% RF VOLTAGE LEVELS
A_s = sqrt(2*50*10^(0.1*(Rx_signal_power-30)));
% peak signal voltage (V)
A_l = sqrt(2*50*10^(0.1*(leakage_power-30)));
% peak leakage voltage (V)
A_n = sqrt(50*10^(0.1*(noise_power-30)));
% RMS noise voltage (V)

% SIMULATE DECHIRP, HANNING WINDOW, AND FAST-TIME FFT
Hd = IF_HPF_Butterworth_3;
Hd2 = IF_LPF_AAF;

% Maximum value in 1-D FFT matrix, found by running this code
% assumes signal power of -124 dBm
MAX_FFT_VAL = 13106184;

ADC_clip_low = zeros(1,M);
ADC_clip_high = zeros(1,M);

for ind = 1:M % for each of the M total fast-time samples
    % 1. Simulate the fast-time Round Trip time vector (s)
    T = 2*R/c + 2*v*((subT+T_pause)*(ind-1)+t_ext)/c;
    % 2*R/c is the base time offset
    % each update of index, target is closer to target by
    % 2*v/c for
    % duration based on index which is (ind-1)*(subT+T_pause)
    % use "t" to convert this T value into a vector of sampled
    % times.

    % 2. Create Hanning window of proper length

    %HANNING QUANT-----

```

```

H = hann(length(t));
h1 = round(H.*4096);      % Quantize ON
%h1 = H*4096;           % Quantize OFF
%-----
% 3. Calculate the amplitudes of leakage, signal, and noise @
% input t0 RX chain
sig_RX = A_s.*sind(360*(f1.*T+k.*t_ext.*T-k/2.*T.^2));
leak_RX = A_l.*sind(360*(f1.*leakage_path_delay + ...
    k.*t_ext.*leakage_path_delay - ...
    k/2.*leakage_path_delay.^2));
noise_RX = A_n.*randn(size(sig_RX));

% 4. Create ideal signal and leakage matrices for analysis
% later
signal(ind,:) = sig_RX;    % IF freq signal
leakage(ind,:) = leak_RX; % IF leakage signal

% 4.1 RF chain amplification (including the IF portion)
% Amplify the noise by Gain (dB), amplify the signal and
% leakage by Gain
% minus NF (dB)
IF_gain = 25.11;
% dB (no ADC) - Theoretically should be 28.11
% assuming gain is 3 dB short due to connector lose
IF_NF = 3.656;           % dB (no ADC)

sig = sig_RX*10^(IF_gain/20); % (V) amplitude
leak = leak_RX*10^(IF_gain/20); % (V) amplitude
noise = noise_RX*10^((IF_gain+IF_NF)/20); % (V) amplitude

% 5. LPF and HPF signal, leakage, noise
%-----
%sln_sum = sig+noise;
sln_sum = sig+leak+noise;
%-----
% IF HPF (two HPF stages combined into 1)
sln_filt1 = filter(Hd, sln_sum);
% IF LPF (LPF after mixer and AAF combined into 1)
sln_filt2 = filter(Hd2, sln_filt1);
% Remove added signal portion which waits for filter ringing
% to stop

% DC BIAS-----
%sln_filt = sln_filt2([201:1001]) % Bias OFF
%sln_filt = sln_filt2([201:1001])-10*V_per_Q; % Bias ON
sln_filt = sln_filt2([201:1001])-...

```

```

(10*V_per_Q + (2*V_per_Q).* ...
randn(size(sln_filt2([201:1001]))));           % Bias ON

%-----
% 6. ADC Quantize to 12 bits and zero pad
zero_pad = zeros(1,(1024-length(h1)));

% ADC QUANT-----
ADC_quant = round((sln_filt)./V_per_Q);       % Quantize ON
% ADC_quant = ((sln_filt)./V_per_Q);         % Quantize OFF
%-----
% Simulate Clipping of ADC if it occurs
% find values of ADC_quant < -2048, set to min value -2048
clipping_low = ADC_quant >= -0.5*(2^12);
min_values = not(clipping_low).*(-0.5)*(2^12);
ADC_quant = ADC_quant.*clipping_low + min_values;
ADC_clip_low(ind) = sum(not(clipping_low));
% find values of ADC_quant > 2048, set to max value 2048
clipping_high = ADC_quant <= 0.5*(2^12);     % 1 for not
% clipped value, 0 for clipped
max_values = not(clipping_high).*0.5*(2^12); % 1 for
% clipped 0 else, multiply 1 by 2^12
ADC_quant = ADC_quant.*clipping_high + max_values;
ADC_clip_high(ind) = sum(not(clipping_high));

% 7. Perform FFT on quantized data and quantized windowing
% function Multiply ADC values with windowing function and
% truncate to 16 bits

% MULTIPLY QUANT-----
slnw = round(((2^16)*(h1'.* ADC_quant))./(2^24));
% Quantize ON
%slnw = (((2^16)*(h1'.* ADC_quant))./(2^24));
% Quantize OFF
%-----
slnfft = fft([slnw, zero_pad]);                % zero pad and FFT

% simulate FFT LSB 16 bits as max 1-D FFT output
slnr = real(slnfft);
slni = imag(slnfft);
scaler = 1.0;
slnr = round((slnr*(2^16))./(scaler*MAX_FFT_VAL));
slni = round((slni*(2^16))./(scaler*MAX_FFT_VAL));
sln(ind,:) = slnr + i*slni;
%sln(ind,:) = slnfft;

```

end

```

% DEBUGGING -----
%max(noise)
%max(noise)/V_per_Q
ADC_clip_chech_high = sum(ADC_clip_high)
ADC_clip_chech_low = sum(ADC_clip_low)
% -----

ft_trunc = 128;
sig_leak_noise= sln(:,1:ft_trunc);

figure;
surf(abs(sig_leak_noise));
title('1-D FFT magnitude');
ylabel('fast time freq (Hz)');
xlabel('slow time index');

% SLOW TIME SIGNAL PROCESSING SECTION
freq_slow = 2*v_max/lambda;
fs_slow = 1/(subT+T_pause);
fs_sample = ceil(freq_slow*(M/2)/(fs_slow/2));

h2 = hann(M);

for ind = 1:ft_trunc
    st_fft = fft(h2.*sig_leak_noise(:,ind));
    st_fft = fftshift(st_fft);
    sln2(:,ind) = st_fft([M/2-fs_sample: M/2+fs_sample]);
end

sln2_dB = 20*log10(abs(sln2+1e-9));

% FREQ AXIS
[l1,l2] = size(sln2);
f_fast = (f_s/2)*l2/512*linspace(0,1,l2);
f_slow = (fs_slow/2)*fs_sample/(M/2)*linspace(-1,1,2*fs_sample+1);

% PLOTS
figure;
surf(f_fast, f_slow, sln2_dB)
xlabel('Fast time freq (Hz)');
ylabel('Slow time freq (Hz)');
zlabel('Relative Power (dB)');
title('Signal Leakage and Noise 2-D FFT');

```

```

caxis([35,120]);
%view(180,0);
view(150,35)
colorbar;
boldify;

% Calculate an SNR

% through Matlab tinkering, found that signal max point is at
% (156, 80)
% i.e. sln2_dB(156,80) is max target echo
% estimate noise floor around (156,80)

% Create a 2D x 2D sample area around signal with the middle
% 2d x 2d area hallowed out (contains signal impulse)
d = 4;
D = 10;
lowD_row = mean(mean(sln2_dB([156-D:156-d], [80-D:80+D])));
highD_row = mean(mean(sln2_dB([156+d: 156+D], [80-D:80+D])));
lowR_col = mean(mean(sln2_dB([156-D+1: 156+D-1], [80-D:80-d])));
farR_col = mean(mean(sln2_dB([156-D+1: 156+D-1], [80+d:80+D])));

% find max signal value
subArea = sln2_dB([156-D:156+D], [80-D:80+D]);
Target_impulse = max(max(subArea))

% calculate total average noise and SNR
avg_NoiseFloor = mean([lowD_row, highD_row, lowR_col, farR_col])
SNR = Target_impulse - avg_NoiseFloor

% Find MAX noise value in 2D x 2D box around target signal
max_lowD_row = max(max(sln2_dB([156-D:156-d], [80-D:80+D])));
max_highD_row = max(max(sln2_dB([156+d: 156+D], [80-D:80+D])));
max_lowR_col = max(max(sln2_dB([156-D+1: 156+D-1], [80-D:80-
d])));
max_farR_col = max(max(sln2_dB([156-D+1: 156+D-1],
[80+d:80+D])));

max_Noise = max([max_lowD_row, max_highD_row, max_lowR_col,
max_farR_col])
SNmaxR = Target_impulse - max_Noise

```

A.3 Ideal AoA simulation with skewed RX array

```

% Simulate usage of subset of AoA dPhase from 3 antenna pairs
% Lei Shi
% 1/19/16

% Theory:
% 1. Each antenna pair provides good AoA estimation except for
end fire
% 2. Remove end fire values for each antenna pairing

% Hypothesis:
% 3. Use 2 antenna pairing in Azimuth to provide full 360
coverage

clear all;
close all;
clc;

%--Constants -----
c = 3e8; % m/s, speed of light
f_center = 2.36e9+7.5E6; % Hz, center freq
lambda = c/f_center; % m, wavelength
d = 56.3e-3; % m, antenna to antenna spacing
%-----

% Simulate Targets in circle on XY plane
Range = 500; % (m) targets located at
Theta = 0:1:360; % (deg) angular resolution of simulation

X = cosd(Theta).* Range; % (m) location on X axis
Y = sind(Theta).* Range; % (m) location on Y axis

% Location of Antennas (Triangle center at (0,0))
%
%      O
%     / | \ d/2
%    /  r  \
%   d   |   d
%  /   (0,0)  \ d/2
% /-----\
% O-----d-----O
%
r = (d/2)/cosd(30);

Ant1 = [0,r]; % ((X,Y) location of Antenna 1

```

```

dx = sind(30)*d;
dy = cosd(30)*d;

Ant2 = Ant1 - [dx,dy];
Ant3 = Ant1 - [-dx,dy];

% Scew of Antenna Location OFF OF Origin
% scewX = 0; %d/12;
% scewY = 0; %d/8;
% Ant1 = Ant1 + [scewX, scewY];
% Ant2 = Ant2 + [scewX, scewY];
% Ant3 = Ant3 + [scewX, scewY];

% Tripod and RX SMA cable imperfections causing non-equalateral
% triangle
%Ant1(2) = Ant1(2)-d/12;
%Ant2(2) = Ant1(2)+d/12;

% Debug: plot Antenna locations
figure;
scatter([Ant1(1),Ant2(1),Ant3(1), 0], [Ant1(2),Ant2(2),Ant3(2),
0]);
grid on;
axis equal;

% Debug: plot circle
figure;
plot(X,Y);
grid on;
axis equal;
hold on;
scatter([Ant1(1),Ant2(1),Ant3(1), 0], [Ant1(2),Ant2(2),Ant3(2),
0]);
hold off;

% Simulate delta phases captured by each antenna pairing

Phase1 = zeros(size(Theta));
Phase2 = zeros(size(Theta));
Phase3 = zeros(size(Theta));

for indT = 1:length(Theta)
    % Range of target at current Theta to each antenna
    R1 = sqrt((X(indT)-Ant1(1))^2 + (Y(indT)-Ant1(2))^2); % m,
range to antennal
    R2 = sqrt((X(indT)-Ant2(1))^2 + (Y(indT)-Ant2(2))^2);

```

```

    % m, range to antenna2
R3 = sqrt((X(indT)-Ant3(1))^2 + (Y(indT)-Ant3(2))^2);
    % m, range to antenna3

%*****
% NOTE
% IF CABLE LENGTHS ARE DIFFERENT, RESULT IN A BIAS IN PHASE
  FOR 1
% ANTENNA. SIMULATE THAT BIAS HERE.
%*****
Phase1(indT) = (R1/lambda-floor(R1/lambda))*360+30;
Phase2(indT) = (R2/lambda-floor(R2/lambda))*360-60;
Phase3(indT) = (R3/lambda-floor(R3/lambda))*360;

dPhase12(indT) = Phase1(indT)-Phase2(indT);
dPhase13(indT) = Phase1(indT)-Phase3(indT);
dPhase23(indT) = Phase2(indT)-Phase3(indT);

end

% Perform Phase Unwrapping -180 to +180
% Method 1: Matlab
    Phase1uw = unwrap(Phase1./360*2*pi);
    Phase2uw = unwrap(Phase2./360*2*pi);
    Phase3uw = unwrap(Phase3./360*2*pi);

    Phase1uw = Phase1uw*360/(2*pi);
    Phase2uw = Phase2uw*360/(2*pi);
    Phase3uw = Phase3uw*360/(2*pi);

    Phase1uw = Phase1uw - mean(Phase1uw);
    Phase2uw = Phase2uw - mean(Phase2uw);
    Phase3uw = Phase3uw - mean(Phase3uw);
% Method 2: Manual
% for ind = 1:length(Theta)
%     if Phase1(ind) > 180
%         Phase1uw(ind) = Phase1(ind)-360;
%     elseif Phase1(ind) < -180
%         Phase1uw(ind) = Phase1(ind) + 360;
%     else
%         Phase1uw(ind) = Phase1(ind);
%     end
%
%     if Phase2(ind) > 180
%         Phase2uw(ind) = Phase2(ind)-360;

```

```

% elseif Phase2(ind) < -180
%     Phase2uw(ind) = Phase2(ind) + 360;
% else
%     Phase2uw(ind) = Phase2(ind);
% end
%
% if Phase3(ind) > 180
%     Phase3uw(ind) = Phase3(ind)-360;
% elseif Phase3(ind) < -180
%     Phase3uw(ind) = Phase3(ind) + 360;
% else
%     Phase3uw(ind) = Phase3(ind);
% end
%
% end

figure;
plot(Theta, Phase1uw, 'b', Theta, Phase2uw, 'r', Theta,
Phase3uw, 'g')
xlabel('Target Spacial Angle (deg)')
ylabel('Electric Phase at Antenna (deg)')
title ('Target Angle to RX Phase')
legend('Ant 1', 'Ant2', 'Ant3')
grid on;
axis equal;

% Perform delta Phase Unwrapping -180 to +180
% Method 1: manual
% for ind = 1:length(Theta)
%     if dPhase12(ind) > 180
%         dPhase12uw(ind) = dPhase12(ind)-360;
%     elseif dPhase12(ind) < -180
%         dPhase12uw(ind) = dPhase12(ind) + 360;
%     else
%         dPhase12uw(ind) = dPhase12(ind);
%     end
%
%     if dPhase13(ind) > 180
%         dPhase13uw(ind) = dPhase13(ind)-360;
%     elseif dPhase13(ind) < -180
%         dPhase13uw(ind) = dPhase13(ind) + 360;
%     else
%         dPhase13uw(ind) = dPhase13(ind);
%     end
%
%     if dPhase23(ind) > 180
%         dPhase23uw(ind) = dPhase23(ind)-360;

```

```

% elseif dPhase23(ind) < -180
%     dPhase23uw(ind) = dPhase23(ind) + 360;
% else
%     dPhase23uw(ind) = dPhase23(ind);
% end
%
% end

% Method 2: MATLAB unwrap
dPhase12 = Phase1uw - Phase2uw;
dPhase13 = Phase1uw - Phase3uw;
dPhase23 = Phase2uw - Phase3uw;

dPhase12uw = unwrap(dPhase12/360*2*pi);
dPhase13uw = unwrap(dPhase13/360*2*pi);
dPhase23uw = unwrap(dPhase23/360*2*pi);

dPhase12uw = dPhase12uw*360/(2*pi);
dPhase13uw = dPhase13uw*360/(2*pi);
dPhase23uw = dPhase23uw*360/(2*pi);

% dPhase12uw = dPhase12uw - mean(dPhase12uw);
% dPhase13uw = dPhase13uw - mean(dPhase13uw);
% dPhase23uw = dPhase23uw - mean(dPhase23uw);

figure;
plot(Theta, dPhase12uw, 'b', Theta, dPhase13uw, 'r', Theta,
dPhase23uw, 'g')
xlabel('Target Spacial Angle (deg)')
ylabel('Electric Phase Difference (deg)')
title('Target Angle to Delta Phases')
legend('dPhase12', 'dPhase13', 'dPhase23')
grid on;
axis equal;
%ylim([-180,180]);

% convert dPhase to AoA
del_length12 = dPhase12uw./360*lambda;
del_length13 = dPhase13uw./360*lambda;
del_length23 = dPhase23uw./360*lambda;

AoA12 = acosd(del_length12./d);
AoA13 = acosd(del_length13./d);
AoA23 = acosd(del_length23./d);

% Debugging: AoA plots

```

```

figure;
plot(Theta, AoA12, 'b', Theta, AoA13, 'r', Theta, AoA23, 'g');
xlabel('Target Angle, Theta, (deg)');
ylabel('Calculated AoA (deg)');
title('Target Spacial Angle vs Calculated AoA');
legend('Ant Pair 12','Ant Pair 13','Ant Pair 23');
grid on;
ylim([-20,200]);

%% SHAVE OFF dPhase ENDFIRE MEASUREMENTS

dPhase_buffer = 25;          % deg, +/- to be removed from endfire
limit

min12 = min(dPhase12uw);
min13 = min(dPhase13uw);
min23 = min(dPhase23uw);
max12 = max(dPhase12uw);
max13 = max(dPhase13uw);
max23 = max(dPhase23uw);

for ind = 1:length(dPhase12)
    if dPhase12uw(ind) < min12 + dPhase_buffer
        dPhase12_buff(ind) = NaN;
    elseif dPhase12uw(ind) > max12 - dPhase_buffer
        dPhase12_buff(ind) = NaN;
    else
        dPhase12_buff(ind) = dPhase12uw(ind);
    end

    if dPhase13uw(ind) < min13 + dPhase_buffer
        dPhase13_buff(ind) = NaN;
    elseif dPhase13uw(ind) > max13 - dPhase_buffer
        dPhase13_buff(ind) = NaN;
    else
        dPhase13_buff(ind) = dPhase13uw(ind);
    end

    if dPhase23uw(ind) < min23 + dPhase_buffer
        dPhase23_buff(ind) = NaN;
    elseif dPhase23uw(ind) > max23 - dPhase_buffer
        dPhase23_buff(ind) = NaN;
    else
        dPhase23_buff(ind) = dPhase23uw(ind);
    end
end
end

```

```

% Debugging: Plot new buffered dPhase after taking off endfire
measurements
figure;
plot(Theta, dPhase12_buff, 'b', Theta, dPhase13_buff, 'r',
Theta, dPhase23_buff, 'g')
xlabel('Target Spacial Angle (deg)')
ylabel('Electric Phase Difference (deg)')
title ('Target Angle to Delta Phases, Excluding Endfire')
legend('dPhase12', 'dPhase13', 'dPhase23')
grid on;
axis equal;
%ylim([-180,180]);

% convert dPhase_buff to AoA
del_length12 = dPhase12_buff./360*lambda;
del_length13 = dPhase13_buff./360*lambda;
del_length23 = dPhase23_buff./360*lambda;

AoA12_buff = acosd(del_length12./d);
AoA13_buff = acosd(del_length13./d);
AoA23_buff = acosd(del_length23./d);

% Debugging: AoA's that can still be calculated
figure;
plot(Theta, AoA12_buff, 'b', Theta, AoA13_buff, 'r', Theta,
AoA23_buff, 'g');
xlabel('Target Angle, Theta, (deg)');
ylabel('Buffered AoA (deg)');
title('Target Spacial Angle vs Buffered AoA');
legend('Ant Pair 12','Ant Pair 13','Ant Pair 23');
grid on;
%ylim([0,180]);

%% COVERAGE ANALYSIS

% As long as 2 dPhase exist at a given Theta, the Azimuth AoA
% can be calculated thus covered.  If only 1 or no dPhase exist,
% this angle is ambiguous.

NaN12 = isnan(AoA12_buff);
% if Not a Number (NaN) then return 1, else 0
NaN13 = isnan(AoA13_buff); % NaN = 1
NaN23 = isnan(AoA23_buff); % Measurement = 0

figure;

```

```

plot(Theta, NaN12, Theta, NaN13, Theta, NaN23)
xlabel('Target Angle, Theta, (deg)');
ylabel('AoA Exist, 1 = No, 0 = Yes');
title('AoA Estimation Exist (Yes/No)');
legend('AoA12', 'AoA13', 'AoA23');
grid on;
ylim([-1,2]);

Overlap_12_13 = NaN12.*NaN13;
    % If both AoA12_buff and AoA13_buff is NaN
    % then this Theta cannot be measured
    % This will return a 1 when both NaN's
    % overlap.
    % If = 1, then this Theta Does Not Exist
    % If = 0, then this Theta Exists
Overlap_12_23 = NaN12.*NaN23;
Overlap_13_23 = NaN13.*NaN23;

% 3 ANTENNA ARRAY
% Create New Circle of X and Y values from only those where AoA
at that
% Theta Exists
for ind = 1:length(Theta)
    if Overlap_12_13(ind) == 1 || Overlap_12_23(ind) == 1 ||
Overlap_13_23(ind) == 1
        X_buff(ind) = NaN;
        Y_buff(ind) = NaN;
        Theta_buff(ind) = NaN;
    else
        X_buff(ind) = X(ind);
        Y_buff(ind) = Y(ind);
        Theta_buff(ind) = Theta(ind);
    end
end

% Debug: plot circle
figure;
plot(X_buff,Y_buff);
xlabel('X axis (m)');
ylabel('Y axis (m)');
title('AoA Coverage Not Using Endfire Measurements, 3
Antennas');
grid on;
axis equal;
Xlim([-600,600]);
ylim([-600,600]);

```

```

% 2 ANTENNA ARRAY
% Create New Circle of X and Y values from only those where AoA
% at that Theta Exists
% Note: Since this only uses 2 Antenna Pairs. If either pair
% reports a NaN then the AoA cannot be uniquely determined
% Thus, this is a summation of both NaNs.

Summation_12_13 = NaN12 + NaN13;
% all values that cannot be used are >= 1
% All values of zero, have good
% measurements from both antenna
% pairings
for ind = 1:length(Theta)
    if Summation_12_13(ind) >= 1
        X2_buff(ind) = NaN;
        Y2_buff(ind) = NaN;
        Theta2_buff(ind) = NaN;
    else
        X2_buff(ind) = X(ind);
        Y2_buff(ind) = Y(ind);
        Theta2_buff(ind) = Theta(ind);
    end
end

% Debug: plot circle
figure;
plot(X2_buff,Y2_buff);
xlabel('X axis (m)');
ylabel('Y axis (m)');
title('AoA Coverage Not Using Endfire Measurements, 2
Antennas');
grid on;
axis equal;
Xlim([-600,600]);
ylim([-600,600]);

```